The Astrophysical Journal, 995:43 (30pp), 2025 December 10 https://doi.org/10.3847/1538-4357/ae07db

EPOCHS. III. Unbiased UV Continuum Slopes at $6.5 < z < 13$ from Combined PEARLS GTO and Public JWST/NIRCam Imaging

Duncan Austin[1], Christopher J. Conselice[1], Nathan J. Adams[1], Thomas Harvey[1], Qiao Duan[1], James Trussler[1], Qiong Li[1], Ignas Juodžbalis[1,2], Katherine Ormerod[1,3], Leonardo Ferreira[4], Lewi Westcott[1], Honor Harris[1], Stephen M. Wilkins[5], Rachana Bhatawdekar[6], Joseph Caruana[7,8], Dan Coe[9,10,11], Seth H. Cohen[12], Simon P. Driver[13], Jordan C. J. D'Silva[13,14], Brenda Frye[15,16], Lukas J. Furtak[17], Norman A. Grogin[9], Nimish P. Hathi[9], Benne W. Holwerda[18], Rolf A. Jansen[12], Anton M. Koekemoer[9], Madeline A. Marshall[14,19], Mario Nonino[20], Rafael Ortiz, III[12], Nor Pirzkal[9], Aaron Robotham[13], Russell E. Ryan, Jr.[9], Jake Summers[12], Christopher N. A. Willmer[16], Rogier A. Windhorst[12], Haojing Yan[21], and Erik Zackrisson[22,23]

[1] Jodrell Bank Centre for Astrophysics, Alan Turing Building, University of Manchester, Oxford Road, Manchester, M13 9PL, UK
[2] Kavli Institute for Cosmology, University of Cambridge, Madingley Road, Cambridge, CB3 0HA, UK
[3] Astrophysics Research Institute, Liverpool John Moores University, 146 Brownlow Hill, Liverpool, L3 5RF, UK
[4] Department of Physics & Astronomy, University of Victoria, Finnerty Road, Victoria, BC V8P 1A1, Canada
[5] Astronomy Centre, Department of Physics and Astronomy, University of Sussex, Brighton, BN1 9QH, UK
[6] European Space Agency (ESA), European Space Astronomy Centre (ESAC), Camino Bajo del Castillo s/n, 28692 Villanueva de la Cañada, Madrid, Spain
[7] Department of Physics, University of Malta, Msida MSD 2080, Malta
[8] Institute of Space Sciences & Astronomy, University of Malta, Msida MSD 2080, Malta
[9] Space Telescope Science Institute, 3700 San Martin Drive, Baltimore, MD 21218, USA
[10] Association of Universities for Research in Astronomy (AURA) for the European Space Agency (ESA), STScI, Baltimore, MD 21218, USA
[11] Center for Astrophysical Sciences, Department of Physics and Astronomy, The Johns Hopkins University, 3400 N Charles Street, Baltimore, MD 21218, USA
[12] School of Earth and Space Exploration, Arizona State University, Tempe, AZ 85287-1404, USA
[13] International Centre for Radio Astronomy Research (ICRAR) and the International Space Centre (ISC), The University of Western Australia, M468, 35 Stirling Highway, Crawley, WA 6009, Australia
[14] ARC Centre of Excellence for All Sky Astrophysics in 3 Dimensions (ASTRO 3D), Australia
[15] Department of Astronomy, University of Arizona, 933 N Cherry Avenue, Tucson, AZ, 85721-0009, USA
[16] Steward Observatory, University of Arizona, 933 N Cherry Avenue, Tucson, AZ 85721-0009, USA
[17] Physics Department, Ben-Gurion University of the Negev, P.O. Box 653, Be'er-Sheva 84105, Israel
[18] Department of Physics and Astronomy, University of Louisville, Natural Science Building 102, Louisville, KY 40292, USA
[19] National Research Council of Canada, Herzberg Astronomy & Astrophysics Research Centre, 5071 West Saanich Road, Victoria, BC V9E 2E7, Canada
[20] INAF—Osservatorio Astronomicodi di Trieste, Via Bazzoni 2, 34124 Trieste, Italy
[21] Department of Physics and Astronomy, University of Missouri, Columbia, MO 65211, USA
[22] Observational Astrophysics, Department of Physics and Astronomy, Uppsala University, Box 516, SE-751 20 Uppsala, Sweden
[23] Swedish Collegium for Advanced Study, Linneanum, Thunbergsvägen 2, SE-752 38 Uppsala, Sweden
Received 2024 April 16; revised 2025 September 12; accepted 2025 September 15; published 2025 December 3

Abstract

We present an analysis of rest-frame UV continuum slopes, β, using a sample of 1011 galaxies at $6.5 < z < 13$ from the EPOCHS photometric sample collated from the GTO PEARLS and public ERS/GTO/GO (JADES, CEERS, NGDEEP, GLASS) JWST/NIRCam imaging across 178.9 arcmin^2 of unmasked blank sky. We correct our UV slopes for the photometric error coupling bias using 200,000 power-law spectral energy distributions for each $\beta = \{-1, -1.5, -2, -2.5, -3\}$ in each field, finding biases as large as $\Delta\beta \simeq -0.55$ for the lowest signal-to-noise ratio galaxies in our sample. Additionally, we simulate the impact of rest-UV line emission (including Lyα) and damped Lyα systems on our measured β, finding biases as large as 0.5–0.6 for the most extreme systems. We find a decreasing trend with redshift of $\beta = -1.51 \pm 0.08 - (0.097 \pm 0.010) \times z$, with potential evidence for Population III stars or top-heavy initial mass functions in a subsample of 68 $\beta + \sigma_\beta < -2.8$ galaxies. At $z \simeq 11.5$, we measure an extremely blue $\beta(M_{\rm UV} = -19) = -2.73 \pm 0.06$, deviating from simulations, indicative of low-metallicity galaxies with nonzero Lyman continuum escape fractions $f_{\rm esc,LyC} \gtrsim 0$ and minimal dust content. The observed steepening of $d\beta/d\log_{10}(M_\star/M_\odot)$ from 0.22 ± 0.02 at $z \simeq 7$ to 0.81 ± 0.13 at $z \simeq 11.5$ implies that dust produced in core-collapse supernovae at early times may be ejected via outflows from low-mass galaxies. We also observe a flatter $d\beta/dM_{\rm UV} = 0.03 \pm 0.02$ at $z \simeq 7$ and a shallower $d\beta/d\log_{10}(M_\star/M_\odot)$ at $z < 11$ than seen by the Hubble Space Telescope, unveiling a new population of low-mass, faint galaxies reddened by dust produced in the stellar winds of asymptotic giant branch stars or carbon-rich Wolf–Rayet binaries.

Unified Astronomy Thesaurus concepts: High-redshift galaxies (734); Dust formation (2269); Ultraviolet astronomy (1736); Infrared telescopes (794)

1. Introduction

The first year of study with the James Webb Space Telescope (JWST; J. P. Gardner et al. 2023) has led to the discovery of a multitude of high-redshift galaxy candidates in the first billion years of cosmic evolution (M. Castellano et al. 2022;

S. L. Finkelstein et al. 2022; Y. Harikane et al. 2023; R. P. Naidu et al. 2022; H. Yan et al. 2023; N. J. Adams et al. 2023; H. Atek et al. 2023; D. Austin et al. 2023; R. Bouwens et al. 2023; C. T. Donnan et al. 2023; G. C. K. Leung et al. 2023) discovered in deep near-IR (NIR) imaging using the Near-InfraRed Camera (NIRCam; M. J. Rieke et al. 2005, 2023) instrument. In addition, several studies, including M. Tang et al. (2023), S. Fujimoto et al. (2023), K. Nakajima et al. (2023), and A. J. Bunker et al. (2024), have spectroscopically confirmed galaxies using JWST's Near InfraRed Spectrograph (NIRSpec) Micro Shutter Assembly (P. Ferruit et al. 2022; P. Jakobsen et al. 2022; T. D. Rawle et al. 2022; T. Böker et al. 2023), with the most distant sources found at $z \sim 12$–13 (e.g., E. Curtis-Lake et al. 2023; B. Wang et al. 2023; M. Castellano et al. 2024; J. A. Zavala et al. 2025).

In these early JWST data, measurements of the UV luminosity function (UVLF) have revealed an overabundance of intrinsically UV-bright sources at $z > 10$ (N. J. Adams et al. 2024; C. T. Donnan et al. 2023; S. L. Finkelstein et al. 2023; R. Bouwens et al. 2023; P. G. Pérez-González et al. 2023; M. Castellano et al. 2023; D. J. McLeod et al. 2023; G. C. K. Leung et al. 2023; S. L. Finkelstein et al. 2024; C. T. Donnan et al. 2024), which may be explained by either the mapping of UV luminosity to host halo mass (e.g., C. A. Mason et al. 2023), an increased star formation efficiency (e.g., K. Inayoshi et al. 2022; J. Mirocha & S. R. Furlanetto 2023), or minimal dust obscuration at high redshift (A. Ferrara et al. 2023; F. Ziparo et al. 2023). Further investigation into the rest-frame UV properties of these galaxies is therefore of the utmost importance to help distinguish between these plausible scenarios.

The rest-frame UV continuum slope, β, is commonly calculated via the power law $f_\lambda \propto \lambda^\beta$ (D. Calzetti et al. 1994, hereafter C94), and is a key diagnostic for understanding the properties of the stellar continuum, providing a tracer of massive O/B-type main-sequence stars and their surrounding H II nebular regions. It is primarily dependent on the galactic dust content, meaning the UV dust attenuation ($A_{\rm UV}$) can be estimated from β via the empirical G. R. Meurer et al. (1999) relation, $A_{\rm UV} = 4.43 + 1.99\beta$. The 100 Myr star formation rates (SFRs) of star-forming galaxies (SFGs) can therefore be estimated from dust-corrected intrinsic UV magnitudes, $M_{\rm UV}$, under an assumed luminosity to SFR conversion ($\kappa_{\rm UV}$; see P. Madau & M. Dickinson 2014). Additionally, β has a more minor dependence on stellar ages and metallicities (see, e.g., R. J. Bouwens et al. 2012; S. Tacchella et al. 2022), especially in bursty star formation history (SFH) models, evidence for which has been observed in a spectroscopically confirmed $z = 7.3$ galaxy by T. J. Looser et al. (2024).

Since β is closely related to the dust content in galaxies, we can use it to study the global build up of galactic dust. It is expected that the dominant dust production mechanism at early times is nucleation in the ejecta of core-collapse supernovae (or CCSNe; e.g., P. Todini & A. Ferrara 2001; S. Bianchi et al. 2009; S. Marassi et al. 2019), although dust destruction processes such as sputtering, sublimation, and grain–grain collisions in the resulting reverse shock are not well constrained even in the local Universe (e.g., M. Bocchio et al. 2016; E. R. Micelotta et al. 2018; F. Kirchschlager et al. 2019, 2024). As well as core-collapse supernovae, dust production also occurs in the stellar winds of 0.8–8 $M_\odot$ asymptotic giant branch (AGB) stars (e.g., S. Zhukovska et al. 2008; H. P. Gail et al. 2009; S. Höfner & H. Olofsson 2018), 12–30 $M_\odot$ red super giant (RSG) stars (E. M. Levesque et al. 2006), and $\gtrsim 30\,M_\odot$ Wolf–Rayet (WR) stars that are carbon-rich (WC stars) with an OB companion (e.g., R. M. Lau et al. 2020, 2022), although the accompanying SN is expected to very quickly destroy dust produced in both RSGs and WCs. Dust reprocessing is also expected in the interstellar medium (ISM) via astration and depletion (e.g., B. T. Draine & E. E. Salpeter 1979; B. T. Draine 2009, 2011), although these processes are not yet fully understood (see R. Schneider & R. Maiolino 2024 for a thorough review). The dust chemistry and grain size distribution impact the extinction curve shape (S. Salim & D. Narayanan 2020), which is often assumed to follow the D. Calzetti et al. (2000), LMC (K. D. Gordon et al. 2003), or SMC (Y. C. Pei 1992) laws. Recent results regarding the relation between IR excess (IRX $= \log_{10}(L_{\rm IR}/L_{\rm UV})$) and β (the IRX–β relation) from Atacama Large Millimeter/submillimeter Array (ALMA) Reionization Era Bright Emission Line Survey (REBELS; R. J. Bouwens et al. 2022) data have, however, demonstrated the suitability of a "Calzetti-like" attenuation curve at $z \simeq 7$ (R. A. A. Bowler et al. 2024).

Prior to the advent of JWST, much effort had been made to measure β in large, unbiased photometric galaxy samples at $z \sim 4$–10 collated from deep imaging by Hubble Space Telescope's (HST) Advanced Camera for Surveys (ACS), Near Infrared Camera and Multi-Object Spectrometer (NICMOS; e.g., N. P. Hathi et al. 2008), and Wide Field Camera 3 (WFC3) IR instruments. The most notable work at $z = 7$–10 has been conducted with WFC3-IR, where β is measured either directly from F105W (Y-band), F125W (J-band), F140W (JH-band) and F160W (H-band) colors (R. J. Bouwens et al. 2009, 2010; S. L. Finkelstein et al. 2010; R. J. McLure et al. 2011; J. S. Dunlop et al. 2012, 2013; R. J. Bouwens et al. 2014; S. M. Wilkins et al. 2016; R. Bhatawdekar & C. J. Conselice 2021), or from the best-fitting spectral energy distribution (SED) template (e.g., S. L. Finkelstein et al. 2012) in the 10 C94 filters designed to omit UV absorption/emission features present in galaxy spectra. These studies find relatively red $\beta \sim -1.9$ at $z \simeq 4$ (e.g., N. P. Hathi et al. 2013) and moderately blue $\beta \sim -2.2/-2.4$ at $z \simeq 7$ in galaxies with $M_{\rm UV} \simeq -19$, symbolic of low-metallicity, relatively dust-free systems, corroborating predictions from simulations (S. M. Wilkins et al. 2012, 2013; V. Gonzalez-Perez et al. 2013).

More recently, the redder JWST/NIRCam filters have given access to the rest-frame UV at $z \gtrsim 10$, allowing for both the first β measurements at these redshifts and improved β measurements from vastly deeper rest-frame near-UV/optical coverage for galaxies at $z \gtrsim 5$. Photometric β measurements have been made in abundance with JWST (M. W. Topping et al. 2022; F. Cullen et al. 2023; A. M. Morales et al. 2024; T. Nanayakkara et al. 2023), with M. W. Topping et al. (2024a) and F. Cullen et al. (2024) observing, on average, extremely blue UV slopes at $z \gtrsim 10$, implying little to no dust presence at these epochs. In addition, JWST studies have found tentative evidence for $\beta < -3$ in individual galaxies at $z \gtrsim 10$ (e.g., H. Atek et al. 2023; D. Austin et al. 2023; F. Cullen et al. 2023; L. J. Furtak et al. 2023), although these may be a result of either photometric scatter or the known β bias from the increased selectability of faint blue galaxies compared to their redder counterparts (see, e.g., A. B. Rogers et al. 2013). These ultra-blue sources may, however, provide evidence for exotic Population III (Pop III) stellar populations

(E. Zackrisson et al. 2011) and/or top-heavy/bottom-light IMFs (e.g., E. Rasmussen Cueto et al. 2023; C. L. Steinhardt et al. 2023). As well as this, these blue galaxies require high Lyman continuum (LyC) escape fractions, $f_{\rm esc,LyC}$, needed to adequately reduce the reddening of the continuum by free–free, free–bound, and two-photon nebular emission (D. Schaerer 2002, 2003; A. Raiter et al. 2010; N. Byler et al. 2017; M. W. Topping et al. 2022). These $f_{\rm esc,LyC}$ are unfortunately impossible to measure directly due to the opacity of the intergalactic medium (IGM) in the Epoch of Reionization (EoR). Several indirect tracers have been suggested, including blue UV β slopes (E. Zackrisson et al. 2013; J. Chisholm et al. 2022), low [O III]+Hβ equivalent widths (EWs; M. W. Topping et al. 2022; R. Endsley et al. 2023), small sizes (S. Mascia et al. 2023), strong Mg II-$\lambda\lambda$2796, 2803 (henceforth Mg II; J. Chisholm et al. 2020; H. Katz et al. 2022), etc., although it is likely that a combination of these is required to accurately measure $f_{\rm esc,LyC}$ (e.g., N. Choustikov et al. 2024). This is necessary to estimate the relative importance of low-mass galaxies, which are expected to contribute a significant fraction of the total ionizing photon budget of galaxies needed to reionize the neutral IGM by $z \simeq 6$ (see, e.g., R. J. Bouwens et al. 2015a; Planck Collaboration et al. 2016, 2020).

In this work, we use the EPOCHS v1 sample photometric galaxy sample, presented in EPOCHS-I (C. J. Conselice et al. 2025), comprising deep public and PEARLS GTO (PIs: R. Windhorst & H. Hammel, PIDs: 1176 and 2738; R. A. Windhorst et al. 2023) JWST/NIRCam imaging. This paper is structured as follows. We outline our data sources and cataloging procedure in Section 2, before calculating UV properties in Section 3. UV slope scaling relations are presented in Section 4, with a discussion of β biases given in Appendix A. We discuss the dust implications and possibility of exotic Pop III and top-heavy IMF scenarios in Section 5, before concluding in Section 6.

ΛCDM cosmological parameters of $\Omega_m = 0.3$, $\Omega_\Lambda = 0.7$, $H_0 = 70\,{\rm km\,s^{-1}\,Mpc^{-1}}$, and AB magnitudes (J. B. Oke 1974; J. B. Oke & J. E. Gunn 1983) are assumed throughout this analysis.

2. Data and Cataloging

2.1. PEARLS Imaging

In this work, we utilize blank-field JWST/NIRCam photometric imaging from the Prime Extragalactic Areas for Reionization Science (PEARLS; PIs: R. Windhorst & H. Hammel, PIDs: 1176 and 2738; R. A. Windhorst et al. 2023) GTO survey. This includes three NIRCam parallel fields surrounding the Hubble Frontier Field (HFF; J. M. Lotz et al. 2017) MACS J0416.1-2403 (hereafter MACS-0416) lensing cluster at $z = 0.396$ and the El Gordo ($z = 0.87$; F. Menanteau et al. 2012) cluster parallel. In addition, we also include data from the four spokes of the North Ecliptic Pole Time Domain Field (NEP-TDF; R. A. Jansen & R. A. Windhorst 2018). As part of the PEARLS survey design, these fields contain imaging in four short wavelength (SW; F090W, F115W, F150W, and F200W) and four long-wavelength (LW; F277W, F356W, F410M, and F444W) NIRCam filters. In addition, we also include bluer F606W imaging from the HST/ACS Wide Field Channel (WFC) in the NEP-TDF from the GO-15278 (PI: R. Jansen) and GO-16252/16793 (PIs: R. Jansen & N. Grogin; see R. O'Brien et al. 2024) HST programs. At the time of writing, the first two NEP-TDF spokes, the first epoch of MACS-0416, and the El Gordo cluster are publicly available from the Minkulski Archive for Space Telescopes (MAST).[24]

2.2. Public ERS and GO Imaging

As part of the EPOCHS sample, we include public ERS and GO imaging from the Grism Lens-Amplified Survey from Space (GLASS; PI: T. Treu, PID: 1324; T. Treu et al. 2022), Data Release 1 of deep JWST Advanced Deep Extragalactic Survey imaging in GOODS-South (JADES-Deep-GS; PI: D. Eisenstein, PID: 1180; D. J. Eisenstein et al. 2023; M. J. Rieke et al. 2023), Cosmic Evolution Early Release Science (CEERS; PI: S. Finkelstein, PID: 1345; M. B. Bagley et al. 2023) and Next Generation Deep Extragalactic Exploratory Public (NGDEEP; PIs: S. Finkelstein, C. Papovich & N. Pirzkal, PID: 2079; M. B. Bagley et al. 2024) surveys. Photometric NIRCam imaging is available in F115W, F150W, F200W, F277W, F356W, and F444W for every survey. Where available, we include the F090W (GLASS and JADES) wideband filter and the F410M (CEERS and JADES) and F335M (JADES) medium-band NIRCam filters.

In addition, we also include bluer data from HST ACS/WFC for CEERS and NGDEEP to somewhat compensate for the lack of blue F090W NIRCam photometry. We use ACS/WFC data in the F606W and F814W filters from the Cosmic Assembly Near-IR Deep Extragalactic Legacy Survey (CANDELS; PIs: S. Faber & H. Ferguson, N. A. Grogin et al. 2011; A. M. Koekemoer et al. 2011; S. Faber 2011) covering the Extended Groth Strip (E. J. Groth et al. 1994) for CEERS, and deep F435W, F606W, and F814W ACS/WFC data from v2.5 of the Hubble Legacy Fields (K. E. Whitaker et al. 2019) covering the HUDF-Par2 for NGDEEP.

2.3. NIRCam Data Reduction Pipeline

Our data reduction pipeline is similar to that of L. Ferreira et al. (2022), N. J. Adams et al. (2023), and D. Austin et al. (2023), and is identical to that used in the rest of the EPOCHS series. A detailed account of this pipeline is presented in N. J. Adams et al. (2024, hereafter EPOCHS-II), which is summarized below.

We use version 1.8.2 of the official JWST data reduction pipeline (H. Bushouse et al. 2022)[25] and Calibration Reference Data System (CRDS) v1084, which includes improved in-flight LW flat-fielding that dramatically deepens these images compared to CRDS v0995. Between stages 1 and 2, we subtract templates of "wisps" in F150W and F200W (SW artifacts produced by reflection off the top secondary mirror support strut, which are most prominent in the B4 detector) using the official STScI templates.[26] We do not remove "claws" (artifacts from nearby bright foreground stars within the susceptibility region) in the NIRCam imaging, but instead mask these post reduction. After stage 2, we apply Chris Willott's $1/f$ noise correction.[27] Before stage 3, we perform background subtraction on individual cal.fits frames, which

[24] An overview of PEARLS data and papers, as well as access to both independently reduced NIRCam imaging and cluster lens models, are available at https://sites.google.com/view/jwstpearls.
[25] https://github.com/spacetelescope/jwst
[26] https://stsci.app.box.com/s/1bymvf1lkrqbdn9rnkluzqk30e8o2bne
[27] See https://github.com/chriswillott/jwst

Table 1
5σ Depths (In 0.″32-diameter Apertures) and Areas of the Blank-field Surveys Used in the EPOCHS-III Sample

Survey	HST ACS/WFC		JWST NIRCam									Area/ arcmin^2	N_{gals}
	F606W	F814W	F090W	F115W	F150W	F200W	F277W	F335M	F356W	F410M	F444W		
NEP-TDF	28.74	⋯	28.50	28.50	28.50	28.65	29.15	⋯	29.30	28.55	28.95	57.32	297
MACS-0416	⋯	⋯	28.67	28.62	28.49	28.64	29.16	⋯	29.33	28.74	29.07	12.30	23
El Gordo	⋯	⋯	28.23	28.25	28.18	28.43	28.96	⋯	29.02	28.45	28.83	3.90	9
CEERS P1-8,10	28.60	28.30	⋯	28.70	28.60	28.89	29.20	⋯	29.30	28.50	28.85	60.31	308
CEERS P9	28.31	28.32	⋯	29.02	28.55	28.78	29.20	⋯	29.22	28.50	29.12	6.08	33
NGDEEP	29.20/30.30	28.80/30.95	⋯	29.78	29.52	29.48	30.28	⋯	30.22	⋯	30.22	6.29	41
JADES-Deep-GS	29.07	⋯	29.58	29.78	29.68	29.72	30.21	29.58	30.17	29.64	29.99	22.98	277
GLASS	⋯	⋯	29.14	29.11	28.86	29.03	29.55	⋯	29.61	⋯	29.84	9.76	23

Note. These differ from those presented in EPOCHS-I as we limit our redshift range to $z < 13$ and also do not use the GTO PEARLS CLIO and ERS SMACS-0723 parallel fields in this analysis. This sample also differs slightly to EPOCHS-II/EPOCHS-IV due to our exclusion of galaxies at $6.5 < z < 7.5$ in El Gordo, MACS-0416, and GLASS due to the large β biases associated with this redshift range. We note that NGDEEP is split into three regions: one has deep HST ACS/WFC coverage (4.03 arcmin^2) and another has shallower ACS/WFC coverage (1.28 arcmin^2), leaving 0.98 arcmin^2 with JWST/NIRCam data alone. These HST areas and depths for NGDEEP are collated from the work of D. Austin et al. (2023).

consists of an initial flat background subtraction followed by a further 2D background subtraction using `photutils` (L. Bradley et al. 2022). This skips the sky-subtraction step in stage 3 and allows for quicker background subtraction assessment and fine-tuning. Post stage 3, we use the `tweakreg` part of the DrizzlePac[28] python package to first align the F444W image onto the Gaia Data Release 3 (DR3; Gaia Collaboration et al. 2018)-derived World Coordinate System (WCS) before matching all remaining filters to this WCS. We finally pixel match to the F444W image with the use of `astropy reproject` (S. L. Hoffmann et al. 2021)[29] to make drizzled images with a pixel scale of 0.″03 per pixel.

2.4. Catalog Creation and Photo-z's

To detect sources in each field, we perform forced photometry in apertures detected in the inverse-variance weighted stacked F277W, F356W, and F444W reduced images using `SExtractor` (E. Bertin & S. Arnouts 1996) with the setup given in EPOCHS-II to produce an initial photometric catalog. Fluxes and magnitudes in both Kron ("FLUX_AUTO" and "MAG_AUTO"; R. G. Kron 1980) and 0.″32-diameter circular ("FLUX_APER" and "MAG_APER") apertures as well as an estimate of the half-light radius ("FLUX_RADIUS"), among other quantities, are produced in this initial `SExtractor` catalog. In this work, we predominantly use the aperture fluxes, which are corrected for the missing flux that is spread beyond the aperture by the point-spread function (PSF) using the simulated `WebbPSF` (M. D. Perrin et al. 2012; M. D. Perrin et al. 2014) PSFs. These PSFs imply that our 0.″32 apertures contain approximately 70%–80% of the total point-source flux. The Kron fluxes are used only to determine correction factors for the stellar mass derived from SED fitting for extended sources only.

For the Hubble images with differing dimensions to our reduced JWST imaging, we use the `photutils` (L. Bradley et al. 2022) python module to perform forced photometry in the same 0.″32-diameter circular apertures from the F277W, F356W, and F444W JWST/NIRCam stack. We also confirm that the fluxes we obtain are consistent with those measured using `sep` (`SExtractor` for python; K. Barbary 2016). We aperture correct our Hubble ACS/WFC photometry using the PSF models given in R. C. Bohlin (2016).

To calculate image depths in each band, we randomly place 0.″32-diameter apertures in empty regions defined by both the `SExtractor` segmentation map and our band-dependent image masks. These image masks are manually created to mask out stellar diffraction spikes, a 50–100 pixel border near the shallower image edges, as well as any remaining image artifacts, such as stray "snowballs," "wisps," or "claws." Each aperture used in these depth calculations is forced not to overlap with any other aperture and to be at least 1″ away from any source. The flux measurements of the nearest 200 apertures to each detected source are used to estimate a "local depth," and hence provide a photometric error defined as the normalized median absolute deviation (NMAD) of the measured fluxes. We choose to adopt this flux error as opposed to the underestimated `SExtractor` output as this more appropriately deals with the correlated noise in the photometric images. To account for potential JWST/NIRCam zero-point (ZP) uncertainties, we also impose a 10% minimum flux error in each band. Table 1 shows the average 5σ depths obtained in each NIRCam band for the JWST surveys used in this work. These are calculated as the NMAD of all apertures in empty image regions as opposed to the average local depth to avoid aperture double-counting.

We next calculate photometric redshifts (photo-z's) for our EPOCHS sample using the `EAZY-py` (G. B. Brammer et al. 2008) SED-fitting code using the standard "tweak_fsps" templates produced using the Flexible Stellar Population Synthesis (FSPS) package (C. Conroy & J. E. Gunn 2010) combined with sets 1 and 4 from the bluer R. L. Larson et al. (2023) template set (referred to henceforth as "fsps_larson") with stronger emission-line treatment. The three pure stellar templates from R. L. Larson et al. (2023; set 1) use v2.2.1 of the Binary Populations and Spectral Synthesis (BPASS; J. J. Eldridge et al. 2017; E. R. Stanway & J. J. Eldridge 2018; C. M. Byrne et al. 2022) stellar population synthesis (SPS) model for ages $\{10^6, 10^{6.5}, 10^7\}$ Gyr at a fixed metallicity $Z_\star = 0.05\,Z_\odot$ while adopting a standard G. Chabrier (2003) IMF. In addition, template set 4 includes nebular continuum and line emission calculated from `CLOUDY` v17

[28] https://github.com/spacetelescope/drizzlepac
[29] https://reproject.readthedocs.io/en/stable/

(G. J. Ferland et al. 2017) with Lyα removed, ionization parameter $\log U = -2$, $Z_{\rm gas} = Z_\star$, LyC escape fraction $f_{\rm esc,LyC} = 0$, $n_{\rm H} = 300\,{\rm cm}^{-2}$ gas cloud hydrogen density, and spherical geometry. We run the EAZY-py photo-z fitting twice with redshift both free ($0 < z < 25$) as well as a "low-redshift" run, where the redshift is limited to be $z < 6$, in order to determine the χ^2 of the best-fitting low-z solution. This is required for our selection criteria outlined in Section 2.5 and has been performed for high-z galaxy identification in the past (e.g., K. Hainline et al. 2023).

2.5. High-z Sample Selection

One potential source of contamination in our EPOCHS sample, other than low-z galaxy interlopers, comes from Milky Way Y- and T-type brown dwarfs. To account for these, we fit Sonora Bobcat brown dwarf templates (M. Marley et al. 2021) to our candidate galaxies via least-squares regression and find the best-fitting solution. In addition, we note that our sample may well contain "little red dots" (LRDs), as found by, e.g., J. Matthee et al. (2024) and V. Kokorev et al. (2024), which are hypothesized to be active galactic nuclei (AGN; see I. Labbe et al. 2025). The impact of contamination by these LRDs on the results of this work is presented in Appendix B, and an analysis of the impact on the global stellar mass function (GSMF) is given in EPOCHS-IV (T. Harvey et al. 2025).

To select a robust sample of high-redshift galaxies from our photometric catalogs, we use similar selection criteria as used in EPOCHS-I/II/IV, outlined below:

1. There must be at least one photometric band entirely bluewards of the Lyα break at $\lambda_{\rm rest} = 1216$ Å. The limits used here are defined by the upper and lower 50% transmission limits of the filters taken from the Spanish Virtual Observatory (SVO; C. Rodrigo & E. Solano 2020) filter profile service. This constrains us to $z \gtrsim 6.5$ when using JWST/NIRCam data alone.
2. Any bands entirely bluewards of the Lyα break must be nondetected at the 3σ confidence level, with bands straddling the break having no signal-to-noise ratio (SNR) requirements.
3. The two bands directly redwards of (but not straddling) the Lyα break must be detected at $>5\sigma$, and all other redwards NIRCam wide bands must be detected at $>2\sigma$.
4. $\int_{0.9\times z_{\rm p}}^{1.1\times z_{\rm p}} P(z)dz \geqslant 0.6$, where $P(z)$ is the probability density function (pdf) and $z_{\rm p}$ is the best-fit photometric redshift from EAZY-py.
5. The best-fit EAZY-py (redshift-free) solution must satisfy $\chi^2_{\rm red.} < 3$, and the difference between the redshift-free and low-redshift best-fitting solutions must satisfy $\Delta\chi^2 > 4$.
6. The SExtractor half-light radius must be greater than or equal to 1.5 pixels in the LW F277W, F356W, and F444W JWST/NIRCam images to ensure the removal of F200W dropout (dithered) hot pixels.
7. If the SExtractor half-light radius is smaller than the PSF full width at half-maximum (FWHM) in F444W, then the difference between the best-fitting brown dwarf solution and the redshift-free EAZY-py run must satisfy $\Delta\chi^2_{\rm red.} > 4$.

In addition to the above selection criteria, we also remove interlopers from our sample by eye. This check was done independently by authors D.A., T.H., Q.L., and N.A. This splits our sample into "certain," "uncertain," and "rejected" candidates. In total we have 1214 unmasked galaxies and 59 brown dwarf candidates in the full EPOCHS catalog, which also includes the blank NIRCam parallel fields of the SMACS-0723 and CLIO strong gravitational lensing clusters.[30] Our "rejected" subsample contains 49 sources removed completely by eye (4% of the full sample), which are mainly sources containing obvious LW hot pixels that just pass our criterion 6 above. This leaves 111 "uncertain" galaxy candidates (9% of the full sample) and 1054 "certain" galaxy candidates. These uncertain candidates mainly comprise sources that are contaminated by stray wisps, claws, or diffuse foreground light. When limiting this to the fields and redshift range used in this work ($6.5 < z < 13$), and removing all galaxies at $6.5 < z < 7.5$ in fields without bluer HST ACS/WFC data (El Gordo, MACS-0416, and GLASS) due to the extreme blue β biases present (see Section 3.1), we are left with 1011 galaxies in our EPOCHS-III sample covering 178.9 arcmin^2 of unmasked blank-sky area (excluding CLIO and SMACS-0723 included in the full EPOCHS sample). Full catalogs and an associated README file will be distributed as part of EPOCHS-I.

2.6. Completeness and Contamination

To estimate the completeness and contamination in our sample, we utilize five realizations of the JAdes extraGalactic Ultradeep Artificial Realizations (JAGUAR; C. C. Williams et al. 2018) mock catalog of SFGs. The mock photometry in the catalog is generated from a family of BEAGLE (J. Chevallard & S. Charlot 2016) SEDs incorporating the G. Bruzual & S. Charlot (2003) SPS and J. Gutkin et al. (2016) nebular emission models. The distribution of redshifts and masses of these SEDs are selected to match the mass functions of A. R. Tomczak et al. (2014), extrapolated to match the $z > 4$ HST UVLFs of R. J. Bouwens et al. (2015b, 2016), V. Calvi et al. (2016), M. Stefanon et al. (2017), and P. A. Oesch et al. (2013, 2018), with $M_{\rm UV}$ calculated from the $M_{\rm UV}$–$M_\star$ relations from 3D-HST (R. E. Skelton et al. 2014; I. G. Momcheva et al. 2016). The UV β slopes in the catalog are calculated from the $M_{\rm UV}$–β relationship given in R. J. Bouwens et al. (2009, 2015b).

For each survey used in this work, we scatter the mock JAGUAR photometry within errors set by the 1σ measured depth with a minimum 10% flux error in each filter before running through our selection procedure outlined in Section 2.5. The absolute magnitude $M_{\rm UV}$ and UV continuum slope β were calculated for the selected sample at the fixed EAZY redshifts (as explained in Section 3), with stellar masses calculated with Bagpipes for the JAGUAR catalog using the setup in Table 2 taking the same bandpass filters and average depths from the CEERS survey.

To account for the SED modeling differences between BEAGLE and Bagpipes, we calculate a median mass difference, $\langle \Delta M_\star \rangle = \log_{10}(M_{\star,\rm obs}/M_{\star,\rm int})$, between observed and intrinsic stellar masses in the CEERS JAGUAR catalog and apply these scaling factors to estimate observed stellar masses

[30] The CLIO cluster is identified at $z = 0.42$ within the Galaxy and Mass Assembly (GAMA; S. P. Driver et al. 2011; J. Liske et al. 2015) survey and imaged with NIRCam as part of the GTO PEARLS JWST program.

Table 2
Summary of Fixed and Free Parameters Used in Our Bagpipes Bayesian SED-fitting Procedure

Parameter	Prior	Limits/Value	Description
Redshift			
z	Fixed	$z_{\rm phot}$	EAZY-py photo-z
Star formation history (log-normal)			
$t_{\rm start}$	$\log_{10}$	(1 Myr, t_U)	Time of star formation onset
$t_{\rm peak}$	$\log_{10}$	(10^{-3}, 15) Gyr	Time of peak star formation
FWHM	$\log_{10}$	(10^{-3}, 15) Gyr	SFH FWHM
Stellar properties			
$\log_{10}(M_\star/M_\odot)$	Uniform	(5, 12)	Stellar mass formed
$\log_{10}(Z_\star)$	Uniform	(-6, 1)	Stellar metallicity
$Z_{\rm gas}$	Fixed	$Z_\star$	Gas-phase metallicity
Nebular properties			
$\log_{10}(U)$	Uniform	(-3, -1)	Ionization parameter
$f_{\rm esc,LyC}$	$\log_{10}$	(0.001, 1)	Lyman continuum escape fraction
$t_{\rm BC}$	Fixed	10 Myr	Birth cloud lifetime
Dust properties			
A_V	$\log_{10}$	(10^{-4}, 10)	V-band attenuation
$\tau_{\rm BC}$	Fixed	0	Birth cloud optical depth

Note. Parameter names, descriptions, and prior distributions/limits for the parameters defining the stellar, nebular and dust properties, as well as the log-normal star formation history are outlined. We note that we have recomputed the default Bagpipes BC03 SPS grids using CLOUDY v17.03 to extend the range of $\log U$ to -1.

from the JAGUAR catalogs simulating other EPOCHS-III fields. For our assumed Bagpipes log-normal SFH, we find the differences between correctly identified high-z SFGs, $\langle \Delta M_{\star,{\rm high}-z} \rangle = 0.244$, and contaminant Balmer break interlopers, $\langle \Delta M_{\star,{\rm interlopers}} \rangle = 0.527$. A closer look at the mass differences for this sample using both the Bagpipes (A. C. Carnall et al. 2018) and Prospector (B. D. Johnson et al. 2021) Bayesian SED-fitting tools is presented in EPOCHS-IV, although we note the large dependence of the SFH assumption on the stellar masses we measure.

For each survey, we calculate the contamination from the respective JAGUAR catalogs following

$$\mathrm{Cont}(\Theta_{\rm obs}) = \frac{N_{\rm selected,interlopers}(\Theta_{\rm obs})}{N_{\rm selected}(\Theta_{\rm obs})}, \quad (1)$$

in bins of $\Theta = \{(M_{\rm UV}, \beta), (M_\star, \beta)\}$ in intrinsic and observed galaxy property frames for completeness and contamination, respectively. In theory, the derived quantities in Equation (1) are also redshift dependent; however, we decide not to bin the contamination by redshift due to the relatively small size of our JAGUAR catalogs. The contamination for our shallowest and deepest surveys (El Gordo and JADES-Deep-GS, where a summary of survey depths is given in EPOCHS-I/II/IV and Table 1) is shown in Figure 1.

We also use our JAGUAR catalogs to provide an estimate of the sample completeness, calculated as

$$\mathrm{Comp}(\Theta_{\rm int}) = \frac{N_{\rm selected}(\Theta_{\rm int})}{N_{\rm total}(\Theta_{\rm int})} \quad (2)$$

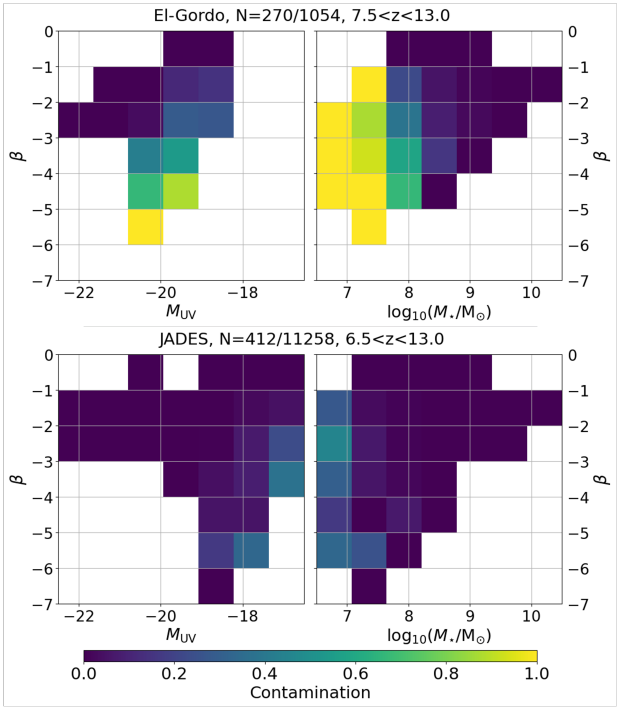

Figure 1. Contamination from lower-redshift SFGs in the El Gordo (upper panels) and JADES-Deep-GS (lower panels) fields for the entire redshift range used in this work ($7.5 < z < 13.0$ for NIRCam-only fields and $6.5 < z < 13.0$ otherwise) as a function of $\Theta = (M_{\rm UV}, \beta)$ (left panels) and $\Theta = (\log_{10} M_\star, \beta)$ (right panels) calculated from the JAGUAR mock galaxy catalog (C. C. Williams et al. 2018). The observed β plotted here is calculated using the photometric power-law method. The total number of selected low-z Balmer break interlopers and selected galaxies is shown in the plot titles. As expected, the most contamination occurs in the faintest, lowest-mass bins, which becomes larger in the bluer bins due to favoring the selection of redder galaxies at these intrinsic magnitudes/masses. JADES-Deep-GS has less contamination in total, which occurs in lower-mass/fainter bins due to its greater depth ($m_{\rm F277W} \simeq 30.2$) and increased number of filters (HST/ACS/WFC F606W and JWST/NIRCam F335M) compared to El Gordo ($m_{\rm F277W} \simeq 29.0$).

in the parameter spaces $\Theta = \{(z, M_{\rm UV}, \beta), (z, M_\star, \beta)\}$, where we bin the completeness in the redshift bins used in this work ($6.5 < z < 8.5$, $8.5 < z < 11$, and $11 < z < 13$). We plot both 20% completeness contours (red) and our JAGUAR simulation limits (black) in Sections 4.2 and 4.3. It is noteworthy that although the effective sky area across our five JAGUAR realizations ($\sim$605 arcmin^2) far exceeds the sky coverage of our EPOCHS-III galaxy sample, there still exists very few high-mass galaxies in our highest-redshift bin. This is most likely due to the rapid fall-off at the high-mass end of the JAGUAR GSMF, which could be somewhat resolved by running more JAGUAR realizations or using a simulation which more accurately matches the high-mass end of updated JWST GSMFs. As well as this, the mock catalogs have a limited range of β covered almost entirely by our SED-fitting template set, making 20% completeness contours difficult to extend past the mere faint, low-mass detection limits in the parameter spaces probed for this work.

3. Calculating UV Properties

In this section, we discuss the two methods of calculating β from the photometric data. The first method calculates β via a

power-law fit ($f_\lambda \propto \lambda^\beta$) to the wideband photometric fluxes for rest-frame wavelengths $1250 < \lambda_{\rm rest}/\text{Å} < 3000$. The second fits the 10 C94 filters using the same power law to the Bayesian SED template posterior for each source. These are discussed in Sections 3.1 and 3.2, respectively. We compare these methods in Section 3.3 and to spectroscopic β in Section 3.4. Since the Bayesian SED-fitting method is systematically biased against measuring the bluest β due to the implicit prior on β, we favor the photometric power-law method in this work.

3.1. Calculating β Slopes from Photometric Fluxes

Since the launch of JWST, we have attained deep, high-resolution imaging in the NIR redward of 1.6 μm, making the direct calculation of β using multiband photometry (as opposed to SED fitting) the preferred method. Where previously we could not calculate β in this way at $z \gtrsim 8.5$ using only the reddest F160W HST/WFC3-IR filter, the vastly improved rest-frame UV coverage from the JWST/NIRCam F200W, F277W, and F356W wide bands now makes this possible at these high redshifts.

In this work, we fit a power law of the form $f_\lambda \propto \lambda^\beta$ to the rest-frame UV photometry, as done by, e.g., A. B. Rogers et al. (2014) and R. J. Bouwens et al. (2014) in the HST era and more recently by, e.g., F. Cullen et al. (2023) and M. W. Topping et al. (2022) using early JWST ERS/ERO NIRCam data. We define which filters are used in this fitting procedure as those that fall entirely within $1250 < \lambda_{\rm rest}/\text{Å} < 3000$, as given by the same 50% flux limits used in our selection criteria in Section 2.5, where the rest-frame wavelengths are derived from the best-fitting `EAZY-py` redshift. For filter i, this is calculated as

$$f_{\lambda,i} \propto \frac{\int_0^\infty T_i(\lambda)\,\lambda^{1+\beta}\mathrm{d}\lambda}{\int_0^\infty T_i(\lambda)\,\lambda\mathrm{d}\lambda} \tag{3}$$

in the photon-counting convention, where T_i is the filter transmission profile for filter i taken from the SVO filter profile service. The filters used are plotted as a function of redshift and rest-wavelength coverage in the top panel of Figure 2.

From these power-law fits, we calculate $M_{\rm UV}$ from the bandpass-averaged flux in a 100 Å-wide top-hat filter centered on $\lambda_{\rm rest} = 1500$ Å. We correct these $M_{\rm UV}$ by a factor $-2.5\log_{10}$ ("FLUX_AUTO"/"FLUX_APER") in the band with effective wavelength closest to $\lambda_{\rm obs} = 1500(1+z)$ Å to account for extended sources when required. Occasionally `SExtractor` overcorrects faint extended sources, so in cases where FLUX_AUTO/FLUX_APER> 10, we instead switch to using the F444W band to apply the correction which avoids the issue.

In the lower panel of Figure 2, we plot the mean β errors, $\langle\sigma_\beta\rangle$, as a function of redshift for the entirely of the EPOCHS-III sample (black) and in three magnitude bins of $M_{\rm UV} < -20.5$, $-20.5 < M_{\rm UV} < -19.5$, and $M_{\rm UV} > -19.5$. Here we outline two main reasons for the trend in σ_β across our sample: the number of JWST/NIRCam bands present in the rest-frame UV, and the SNR of each galaxy in these aforementioned filters. From Figure 2, we see that for the majority of our redshift ranges of interest ($7.2 < z < 9.4$ and $9.5 < z < 12.3$) there are only two rest-UV wide bands, whereas this increases to three at $6.5 < z < 7.2$ and

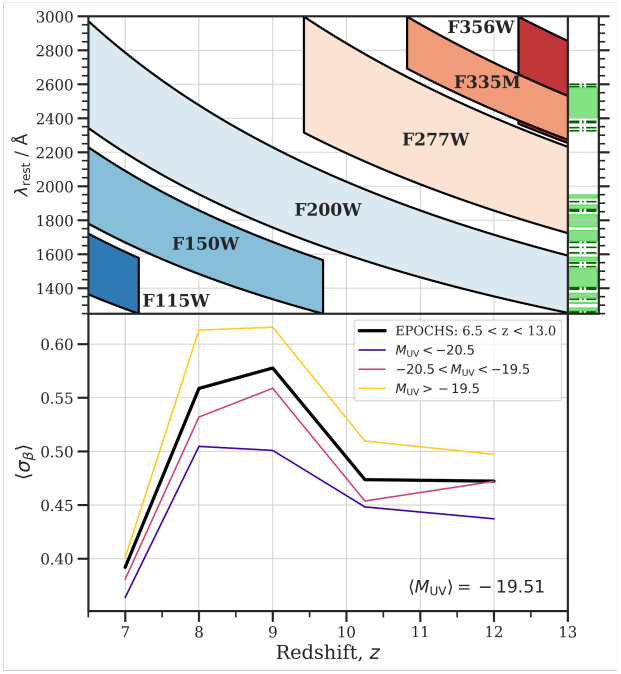

Figure 2. Top: rest-frame UV coverage of the JWST/NIRCam filters used in this work as a function of both redshift and $\lambda_{\rm rest}$. The right-hand side shows the rest-wavelength coverage of the 10 C94 filters in shaded lime green, which are used to avoid prominent rest-frame UV nebular emission lines, shown as dashed–dotted dark green lines in this same side plot. Bottom: average power-law measured β errors, $\langle\sigma_\beta\rangle$, as a function of both redshift and $M_{\rm UV}$. We plot our EPOCHS-III sample, with $\langle M_{\rm UV}\rangle = -19.51$, in black as well as in three $M_{\rm UV}$ bins: $M_{\rm UV} < -20.5$ (purple), $-20.5 < M_{\rm UV} < -19.5$ (pink), and $M_{\rm UV} > -19.5$ (yellow). As expected, we observe a trend of decreasing σ_β with increasing intrinsic UV magnitude due to the increased apparent magnitude (and hence decreased photometric errors) of the brighter sources in our sample.

$12.3 < z < 13$. In the JADES-Deep-GS data, the inclusion of the F335M medium band instead gives this data set three rest-UV filters at $10.8 < z < 12.3$ and four at $12.3 < z < 13$. It is clear to see that the increased number of rest-UV bands reduces σ_β for our entire sample from $\sigma_\beta \simeq 0.4$ at $z < 7.2$ to $\sigma_\beta \simeq 0.55$ at $7.2 < z < 9.4$ and $\sigma_\beta \simeq 0.47$ at $z > 9.4$. We also note that objects with brighter apparent UV magnitudes have reduced σ_β due to their smaller photometric errors. This is apparent in the lower panel of Figure 2, where the average for the full sample with $\langle M_{\rm UV}\rangle = -19.51$ lies between the $-20.5 < M_{\rm UV} < -19.5$ and $M_{\rm UV} > -19.5$ bins.

3.2. Calculating β Slopes via Bayesian SED Fitting with Bagpipes

In addition to measuring β with a power-law fit to the rest-frame UV photometry, we run the `Bagpipes` Bayesian SED-fitting code (A. C. Carnall et al. 2018) to measure β from the best-fit SED for all of the available photometric fluxes rather than just those in the rest-frame UV. We use the 2016 version of the G. Bruzual & S. Charlot (2003, hereafter BC03) SPS models assuming a P. Kroupa (2001) IMF and D. Calzetti et al. (2000) dust attenuation law with redshift fixed to that measured by `EAZY-py`. The A. K. Inoue et al. (2014) model for IGM attenuation is assumed, and we do not model the Lyα damping wing due to the uncertain nature of the patchy IGM during reionization. We assume a log-normal SFH parametrized by the timescales for star formation onset ($t_{\rm start}$), star

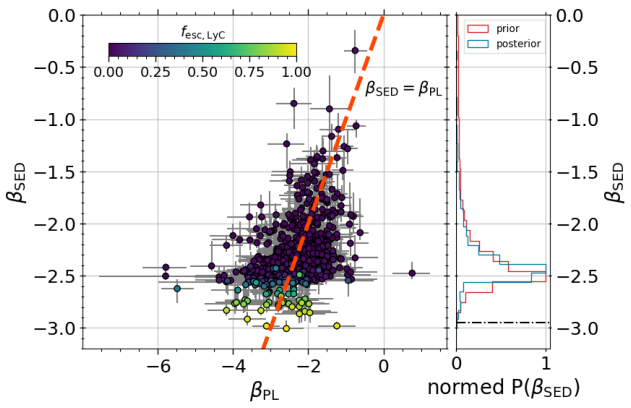

Figure 3. Left: comparison of photometrically measured β slopes for both the SED-fitting and bias-corrected power-law methods for our EPOCHS-III sample colored by `Bagpipes`-derived $f_{esc,LyC}$. $\beta_{PL,corr} = \beta_{SED}$ is shown in dashed orange, which does not represent the best fit to the data. Right: UV slope prior (red) and posterior probability density (blue) for β_{SED}. We see that the posterior β_{SED} somewhat follows the prior in that the extreme blue β values are largely avoided due to the limited range of parameter space explored by our `Bagpipes` template set. The black dotted–dashed line represents the bluest achievable $\beta_{SED} = -2.95$.

formation peak ($t_{max.}$), and log-normal FWHM. The stellar mass ($M_\star$), metallicity (Z), V-band dust attenuation (A_V), nebular ionization parameter (U), and Lyman continuum escape fraction ($f_{esc,LyC}$), are given wide priors in base 10 logarithmic space (equivalent to uniform priors on the logged parameter). We fix the age of the nebular birth clouds (BCs) to $t_{BC} = 10$ Myr, which are also assumed to have no additional dust attenuation (as in the default `Bagpipes` setup). A summary of the fixed and free parameters of our `Bagpipes` fits, as well as the underlying assumptions made about the family of SEDs we are using to perform the analysis, is given in Appendix C.

Several physical properties are calculated from these `Bagpipes` runs, including β, M_{UV}, and $M_\star$. β is calculated by fitting the same power-law function as in Section 3.1 to the posterior spectrum in the 10 C94 top-hat filters and M_{UV} is calculated in the same way as in Section 3.1. The posterior on stellar mass, $M_\star$, is an output from the base `Bagpipes` code. This is subsequently corrected for extended sources by "FLUX_AUTO"/"FLUX_APER" in the F444W, band where appropriate, which traces the rest-frame optical light.

We use the stellar masses calculated in our `Bagpipes` run when determining the contamination likeliness of each galaxy in Section 2.6 and when observing trends between β and $M_\star$ in Section 4.3. While we do not consider the majority of the constrained `Bagpipes` parameters in this work, it is noteworthy that the $f_{esc,LyC}$ values in Figure 3 are illustrative only, and are not well constrained due to their degeneracy with the stellar metallicities and galaxy ages derived from the assumed log-normal SFH.

3.3. Comparison of Photometric β Slope Methods

In this section, we compare and contrast our two different photometric methods to measure β in order to determine which values to use in the analysis performed in this work. A comparison of β measurements (with the power-law β corrected for the biases explored in Appendix A) is shown in the left-hand panel of Figure 3.

The SED-fitting method uses all available photometric data and produces more precise values of β for individual galaxies due to the mitigation of photometric errors that arise when fitting a power law to a small number of flux measurements. In addition, using the SED method means that the β values are calculated using the same underlying assumptions as the stellar masses, leading to more consistent conclusions. In addition, the power-law method is more susceptible to photometric scatter (see Section 3.5), rest-frame UV contamination by nebular emission lines (see Appendix A.1), as well as the redshift- and filter-set-dependent unequal coverage of the rest-frame UV (Figure 2).

Photometric SED fitting for β is the favored method of S. L. Finkelstein et al. (2012), R. Bhatawdekar & C. J. Conselice (2021), and A. M. Morales et al. (2024); however, it has previously been noted that this method is systematically biased by the limited range of β allowed by the choice of IMF and SPS model (e.g., A. B. Rogers et al. 2013; F. Cullen et al. 2023). This primarily impacts the range of allowed blue β slopes, which biases the SED-fitted β redwards (i.e., toward less negative values). While our template set reaches as blue as $\beta = -2.95$ for the youngest ($t \simeq 1$ Myr), most metal-poor ($Z_\star = 10^{-6} Z_\odot$), dust-free, stellar-dominated ($f_{esc,LyC} = 1$) galaxies, the likelihood of measuring blue β slopes via SED fitting is impacted by the implicit β prior (determined as a complex function of our other input priors outlined in Table 2).

We plot this β prior in the right-hand panel of Figure 3 and compare to the β posterior from our SED-fitting method. It is clear that while the bluest achievable β, shown as the black dashed–dotted line, is sufficiently blue, the probability of measuring $\beta \lesssim -2.7$ becomes increasingly unlikely using the `Bagpipes` setup given in Table 2. We therefore choose to adopt the power-law photometric β method in the rest of the analysis done in this paper so as to avoid truncating the measured β distribution blueward of $\beta \simeq -2.95$.

We test whether our β prior is strongly dependent on SFH by rerunning our SED-fitting procedure with the "continuity bursty" SFH parameterization used in EPOCHS-IV and originally by J. Leja et al. (2019) and S. Tacchella et al. (2022), finding minimal differences in the β value at which this prior falls off. Rerunning instead using templates derived from BPASS as opposed to BC03 pushes this soft limit bluewards by ∼0.1–0.2 and the lowest possible UV slope to $\beta = -3.1$; the values of these β limits are therefore impacted most strongly by choice of SPS model.

3.4. Spectroscopic Comparison

To assess the accuracy of our photometric β measurements, we compare to those derived from spectroscopic measurements using the low-resolution $R \sim 100$ NIRSpec PRISM/CLEAR disperser-filter combination from the DAWN JWST Archive (DJA).[31] An outline of the data reduction process using the public `msaexp`[32] tool is given in K. E. Heintz et al. (2024).

We cross-match our photometric sample from CEERS and JADES-Deep-GS with those with robust spectroscopic redshifts in DJA, finding a total of 55 matches, with 41 having robust NIRSpec redshifts (selected using "grade == 3"). This sample consists of 15 galaxies from CEERS, seven from the

[31] https://dawn-cph.github.io/dja/
[32] https://github.com/gbrammer/msaexp

CEERS DDT (PI: P. Arrabal Haro, PID: 2750; P. Arrabal Haro et al. 2023a, 2023b), eight from JADES program 1180 (PI: D. Eisenstein, PID: 1180; D. J. Eisenstein et al. 2023), and 11 from JADES program 1210 (PI: N. Lützgendorf, PID: 1210; A. J. Bunker et al. 2024). A summary of the spectroscopically measured β and previous literature studies publishing these sources is given in Table 8.

Additionally, we search the DJA for medium-resolution ($R \sim 1000$) and high-resolution ($R \sim 2700$) spectra, finding matches for four CEERS galaxies in the medium-resolution F100LP/G140M, F170LP/G235M, and F290LP/G395M filter-disperser pairs (CEERSP3-559,2668,9946 and CEERSP6-7138). Four JADES-Deep-GS galaxies have medium-resolution F070LP/G140M, F170LP/G235M, and F290LP/G395M (IDs 12248, 15023, 15705, and 26579) grating spectra only, and six more (IDs 14738, 15297, 18531, 18605, 19523, and 21391) have both medium-resolution and additional high-resolution F270LP/G395H grating spectra.

We calculate spectroscopic β slopes by fitting a power law in f_λ to the NIRSpec PRISM spectra both in the 10 C94 filters and in the $1250 < \lambda_{\rm rest}/\text{Å} < 3000$ wavelength range. In addition, rest-frame UV SNRs are calculated over this same wavelength range. We plot our spectroscopic β measurements against photometric β calculated using both the power law (described in Section 3.1) and SED-fitting methods (see Section 3.2) in Figure 4, including only those galaxies with UV continuum $\text{SNR}_{\rm UV} > 3$.

Figure 4 also shows a comparison of the spectroscopic and photometric redshifts, which, if significantly different, may provide a large impact on the measured β. We categorize the photo-z error by a quantity, ϵ, where

$$1 + \epsilon = \frac{1 + z_p}{1 + z_s} = \frac{\lambda_{\rm p}}{\lambda_{\rm s}} \tag{4}$$

also indicates a wavelength shift between photometric and spectroscopic observed-frame SED features at $\lambda_{\rm p}$ and $\lambda_{\rm s}$, respectively. We find that 40/41 galaxies in this spectroscopic sample fall within $|\epsilon| < 0.1$, hence we conclude that this is not a significant factor in the differences between β measurements here.

We measure the inverse-variance weighted mean and standard error for our different β measurements, finding photometric results of $\langle\beta_{\rm phot,SED}\rangle = -2.31 \pm 0.00$ and $\langle\beta_{\rm phot,PL}\rangle = -2.40 \pm 0.02$. In addition, we also correct the power-law β measurements for the β bias explored in Appendix A, which reddens the inverse-variance weighted mean by 0.04 to $\langle\beta_{\rm phot,PL,corr}\rangle = -2.36 \pm 0.02$. To assess whether our photometric and spectroscopic β measurements are statistically likely to arise from the same underlying distribution (which they should since they are the same galaxies), we perform a two-sided Kolmogorov–Smirnoff (KS) test using the "scipy.stats.ks_2samp" (J. L. Hodges 1958) python function. For our power-law photometric β, we measure KS = 0.18 with a corresponding $p = 0.67$ after bias corrections compared to (KS, p) = (0.29, 0.11) for the SED-fitting photometric β, suggesting that the SED-fitting results likely contain larger systematic errors.

Since the SED-fitting method uses the same wavelength coverage as the spectroscopic results, we may naively expect these results to match closely. However, they remain systematically red (with 6.8σ significance) due to the limited parameter space covered by the SED template set. This is portrayed by the

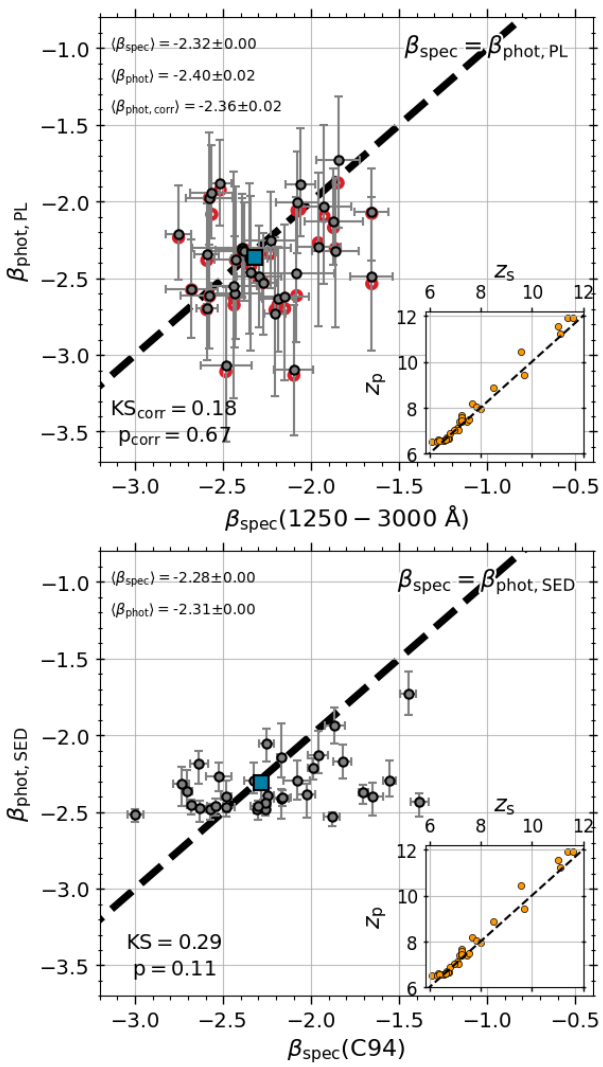

Figure 4. Comparison of redshifts and β slopes for our $6.5 < z < 13$ EPOCHS photometric sample cross-matched with $>3\sigma$ UV-continuum-detected PRISM/CLEAR NIRSpec spectroscopic results from DJA. Top: power-law-measured β that are both corrected (gray circles) and uncorrected (hollow red circles) for the β bias in Appendix A against spectroscopic β measured over $1250 < \lambda_{\rm rest}/\text{Å} < 3000$. The blue square shows the inverse-variance weighted mean for our bias-corrected results. Bottom: SED-measured β from our `Bagpipes` fitting against spectroscopic β measured in the 10 C94 filters. Inverse-variance weighted mean values are given in the upper left and a photometric vs. spectroscopic redshift comparison is given in the lower right. $\beta_{\rm phot} = \beta_{\rm spec}$ is shown as a thick dashed line. Two-sided KS-test results and corresponding p-values are shown in the lower left of both panels, where the power-law β in the upper panel has been bias corrected.

`Bagpipes` β prior in the right-hand panel of Figure 3. Even though the photometric power-law fits for β do not have complete coverage over $1250 < \lambda_{\rm rest}/\text{Å} < 3000$ (with redshift and filter-set dependence shown in Figure 2), they disagree at just the 2.0σ significance level with the spectroscopic results. In addition, we note that the difference could be compounded by additional β biases caused by strong rest-frame UV emission lines, Lyα emitter (LAE), or damped Lyα (DLA) systems that we do not correct for in this work (see Appendix A).

In the rest of this work, we favor the power-law photometric β calculation method due to the fewer systematic biases associated with measuring β in this way, albeit at the expense of greater photometric σ_β errors.

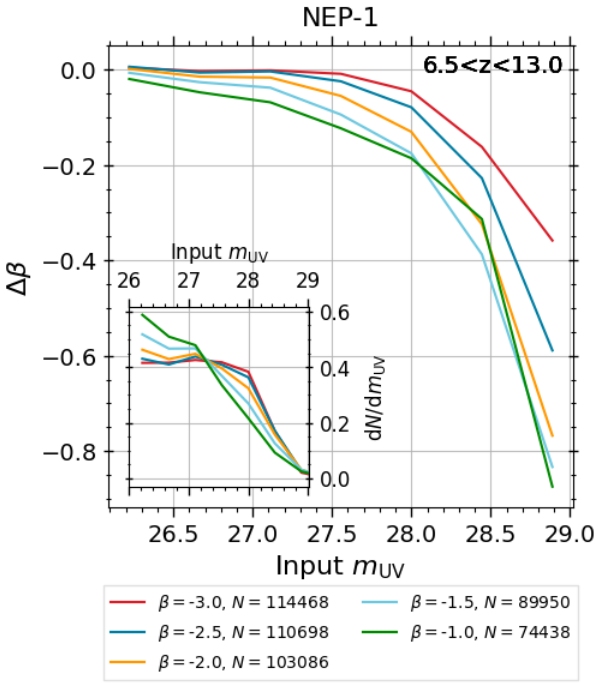

Figure 5. β bias as a function of $m_{\rm UV}$ for the NEP-TDF field calculated from 200,000 power-law SEDs with intrinsic $\beta = \{-1, -1.5, -2, -2.5, -3\}$, shown in green, light blue, yellow, dark blue, and red, respectively. The number of selected SEDs is given in the legend for each intrinsic β, with bluer β (at fixed $m_{\rm UV}$) more efficiently selected. The lower-left inset shows the number density of sources detected as a function of $m_{\rm UV}$, normalized such that the total area equals 1. Since the reddest $\beta = -1$ mock SEDs are less efficiently selected in the faintest magnitude bin (shown by the $dN/dm_{\rm UV}$ being largest at $m_{\rm UV} \simeq 26$ and smallest at $m_{\rm UV} \simeq 29$ in the normalized inset plot), they exhibit the greatest β bias, which can reach as large as -0.85 for $\beta = -1$, $m_{\rm UV} = 29$ in the NEP.

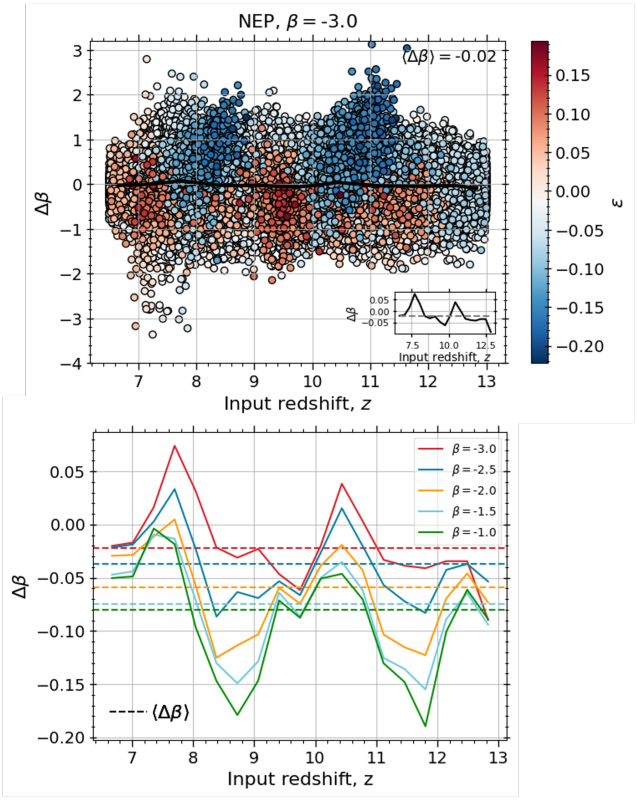

Figure 6. Top: $\Delta\beta$ for galaxies with intrinsic $\beta = -3$ in the NEP-TDF as a function of input redshift. The mock galaxies are colored by the photometric redshift error, where blue (red) points have underestimated (overestimated) photo-z's, respectively. The overplotted thick black line shows the average bias in the selected sample, a zoomed-in version of which is shown in the lower right. Bottom: β bias as a function of simulation input redshift in the NEP-TDF from 200,000 power-law SEDs with results for intrinsic $\beta = \{-1, -1.5, -2, -2.5, -3\}$, shown in green, light blue, yellow, dark blue, and red, respectively. Median $\Delta\beta$ values, $\langle\Delta\beta\rangle$, are shown as horizontal dashed lines, which become bluer with reddening intrinsic β.

3.5. Photometric β Biases

The most widely reported β bias is the so-called "photometric error coupling bias" (termed by R. J. Bouwens et al. 2012), which biases faint objects approaching our detection limit blue. This bias impacts our high-redshift galaxy sample, which is selected based on SNR requirements either side of the Lyα break at 1216 Å, favoring the selection of sources with upscattered photometry at luminosities just below the survey detection limit. Since the same flux measurements are used to measure β, the boost in flux bluewards of the Lyα break biases our measurements blue. In contrast, galaxies where the first photometric band at $\lambda_{\rm rest} > 1216$ Å scatters down have a reduced Lyα break strength and a more prominent Balmer break photo-z solution, and hence are less likely to be selected in our sample.

This bias has been analyzed extensively for β measurements using HST/WFC3-IR F125W, F140W and F160W fluxes in the 2009 Hubble Ultra Deep Field (or HUDF09; PI: G. Illingworth, HST PID: 11563; see R. J. Bouwens et al. 2011), the 2012 Hubble Ultra Deep Field (or HUDF12; PI: R. Ellis, HST PID: 12498; R. S. Ellis et al. 2013; A. M. Koekemoer et al. 2013) and CANDELS (A. M. Koekemoer et al. 2011; N. A. Grogin et al. 2011) campaigns at $z \sim 6$–8 (e.g., S. L. Finkelstein et al. 2012; R. J. Bouwens et al. 2012; J. S. Dunlop et al. 2012; A. B. Rogers et al. 2013; J. S. Dunlop et al. 2013; R. J. Bouwens et al. 2014), as well as in the HFF MACS-0416 lensing cluster (R. Bhatawdekar & C. J. Conselice 2021). More recently, this has been done for large photometrically selected JWST samples using both power-law (F. Cullen et al. 2023; M. W. Topping et al. 2024a; F. Cullen et al. 2024) and SED-fitting (A. M. Morales et al. 2024) measurements of β.

To analyze this photometric error coupling bias, we produce 200,000 power-law SEDs for each intrinsic $\beta = \{-1, -1.5, -2, -2.5, -3\}$, which appropriately match the UV slopes in our observed data, for each field used in this work. Each SED is next randomly assigned an intrinsic $m_{\rm UV}$ in the interval $26 < m_{\rm UV} < 30$ and bandpass-averaged fluxes are measured with the appropriate filter set for the field. Photometric errors are calculated exactly as for the real data, assuming each galaxy has a local depth given by the average 5σ depths in the field with a 10% minimum error floor to reflect the same NIRCam ZP tolerance allowed in our real photometry. We next scatter our photometric flux measurements within their respective Gaussian errors and rerun through the same high-z `EAZY-py` photo-z calculation and selection as in Section 2.4. As before, we remeasure β using the power-law method and calculate $\Delta\beta$ for selected objects only. Results of this simulation for the NEP-TDF field are shown as a function of input $m_{\rm UV}$ in Figure 5 and redshift in Figure 6.

In Figure 5, we observe two effects that play a role in the observed β bias, namely the selection volume and the aforementioned "photometric error coupling" biases. The first

effect arises since bluer objects are inherently more selectable with the EPOCHS selection criteria: Approximately 57% of mock galaxies with intrinsic $\beta = -3$ are selected compared to 37% with $\beta = -1$. The reasoning for this is twofold, namely that faint red galaxies more regularly fail the 5σ SNR cut in the first band entirely at $\lambda_{\rm rest} > 1216$ Å (criterion 3 in Section 2.5) and are more likely confused with Balmer break galaxies at lower redshift (criteria 4 and 5 in Section 2.5) due to their shallower Lyα breaks.

The photometric error coupling bias exacerbates this since objects scattering to bluer β become more selectable. This can be seen in the inset plot of Figure 5 showing the normalized selection function ($dN/dm_{\rm UV}$), which at the faintest magnitudes is greater for bluer galaxies. The difference between the two biases is thus subtle, and the combination leads to the largest $\Delta\beta \sim -0.85$ for $\{\beta, m_{\rm UV}\} = \{-1, 29.0\}$ in the NEP. Similar trends are observed across all of the fields in this study.

In Figure 6, we observe both a red bias at $z \simeq 7.6, 10.5$ and a blue bias at $z \simeq 8.6, 11.8$, caused mainly by photo-z inaccuracy. At these redshifts, the Lyα break passes between the F090W/F115W and F115W/F150W bands, leading to minor systematic redshift errors $|\epsilon| \sim 0.15$ as a result (the second of these is also noted in F. Cullen et al. 2024). We note that these redshift-dependent effects can be mitigated considerably by the inclusion of deep HST/WFC3-IR and medium-band JWST/NIRCam photometry, where additional wavelength coverage surrounding the break likely reduces these photo-z errors.

The β correction factors used in this work are estimated based on the redshift, $m_{\rm UV}$, and observed β dependence of the photometric error coupling bias only. This is calculated for each individual galaxy following

$$\Delta\beta_{\rm tot} = \Delta\beta_{z,i} + \Delta\beta_{m_{\rm UV},i} - \langle\Delta\beta\rangle_i. \quad (5)$$

Here $\Delta\beta_{\rm tot}$ is the total β bias, $\Delta\beta_{z,i}$ and $\Delta\beta_{m_{\rm UV},i}$ are the photometric error coupling biases in terms of redshift and $m_{\rm UV}$ in field i, and $\langle\Delta\beta\rangle_i$ is the median bias included to avoid double-counting. For our EPOCHS-III sample, we measure an average bias measurement of $\langle\Delta\beta\rangle = -0.06^{+0.06}_{-0.10}$. While this measurement seems like a minor correction, we note that at the extremes we measure galaxies with $\Delta\beta = -0.55$ and $\Delta\beta = 0.24$. It is also clear from Figure 5 that the bias is greater for redder galaxies, which are fainter and have lower masses due to the preferential upscattering of red compared to blue galaxies at a given $m_{\rm UV}$. This means the bias corrections made in this work will mostly act to redden already red galaxies, increasing the slope of our measured β–$M_{\rm UV}$ and decreasing the slope of our β–$M_\star$ relations in Sections 4.2 and 4.3, respectively.

The use of power-law SEDs, however, does not describe the full picture from the real Universe. Additional constraints in the rest-frame optical (i.e., nebular emission lines, the $\lambda_{\rm rest} = 3646$ Å Balmer jump, or the Balmer break at $\lambda_{\rm rest} \simeq 4000$ Å) will increase the accuracy of photo-z measurements. We conclude, therefore, that the bias corrections as a result of photo-z uncertainties are likely overestimated in all fields due to this necessary simplification. In addition, we note that this technique neglects possible degeneracies that may exist between $\Delta\beta_{z,i}$ and $\Delta\beta_{m_{\rm UV},i}$, and that an even more computationally expensive procedure is required to adequately measure these using a more statistically significant sample size.

In Appendices A.1, A.2, and A.3, we outline potential photometric β biases from UV line emission, DLAs, and LAEs using power-law SEDs and the eight wideband PEARLS NIRCam filters in great detail. We conclude that, while it is important to note their potential impact, the biases from DLAs and LAEs are expected to be much smaller than those from the photometric redshift coupling bias. Maximum biases of $\Delta\beta_{\rm DLA} \simeq 0.5$ for DLAs (at $z \simeq \{6.5, 8.3, 12\}$ for the highest possible H I column densities, $N_{\rm HI} = 10^{23.5}\,{\rm cm}^{-2}$) and $\Delta\beta_{\rm LAE} \simeq -0.6$ for LAEs (at $z \simeq 7.3$ for the largest ${\rm EW_{rest}(Ly}\alpha) = 300$ Å) are possible, although these describe extreme systems and the sample averages are likely $|\Delta\beta| \lesssim 0.05$.

The bias from line emission can approach $|\Delta\beta| \simeq 0.2$ for the strongest UV line emitters, although this remains very sensitive to the emission-line strengths and ratios of the rest-frame UV nebular lines, which are largely inaccessible in wideband photometric data. Perhaps with medium- and narrowband SW filters on NIRCam, for instance from the Medium Bands, Mega Science (PI: K. Suess, PID: 4111; K. A. Suess et al. 2024) or Medium-band Imaging with NIRCam to Explore ReVolutionary Astrophysics (or MINERVA; PI: A. Muzzin, PID: 7814; A. Muzzin et al. 2025) programs, or alternatively additional deep WFC3-IR imaging from HST, we may be able to correct for this in the near future. We therefore do not correct for any of these three biases in this work.

4. Results

4.1. Redshift Evolution

We now determine whether the decreasing trend of β with redshift found in HST data (e.g., S. L. Finkelstein et al. 2012; R. J. Bouwens et al. 2014; R. Bhatawdekar & C. J. Conselice 2021) extends to $z > 10$ in JWST data. We plot our bias-corrected power-law β–z relation for the EPOCHS-III sample in Figure 7, with circular beige points showing bootstrapped median data points at $z \simeq 7$, $z \simeq 9$, and $z \simeq 11.5$. For each of our 10,000 bootstraps, we (1) randomly scatter each galaxy within their redshift and β pdfs; (2) bin the galaxies in redshift and randomly select (with replacement) a number of galaxies chosen from a Gaussian centered on the number of galaxies in the bin, with width given by the Poisson error on this; (3) calculate the median of each bin; and (4) calculate the median and 16th–84th percentiles of the bootstrapped median values in each bin. We also follow this method to calculate bootstrapped median data points in Sections 4.2 and 4.3. Our bootstrapped median data points, as well as the corresponding median $\langle M_{\rm UV}\rangle$ values, are given in Table 3.

We find that the individual data points in Figure 7 are best fit by the power law

$$\beta = -1.51 \pm 0.08 - (0.097 \pm 0.010) \times z, \quad (6)$$

implying a decreasing β at earlier cosmic times. The negative slope of β–z is steeper than the JWST photometric results of M. W. Topping et al. (2024a) and shallower than those of F. Cullen et al. (2024), who measure $d\beta/dz = -0.030^{+0.024}_{-0.029}$ and $d\beta/dz = -0.28^{+0.04}_{-0.04}$, respectively, at similarly high redshifts, although it remains consistent with the $d\beta/dz = -0.10 \pm 0.06$ derived at $z < 6$ by R. J. Bouwens et al. (2014). These trends are dependent on both the method used to measure β and the

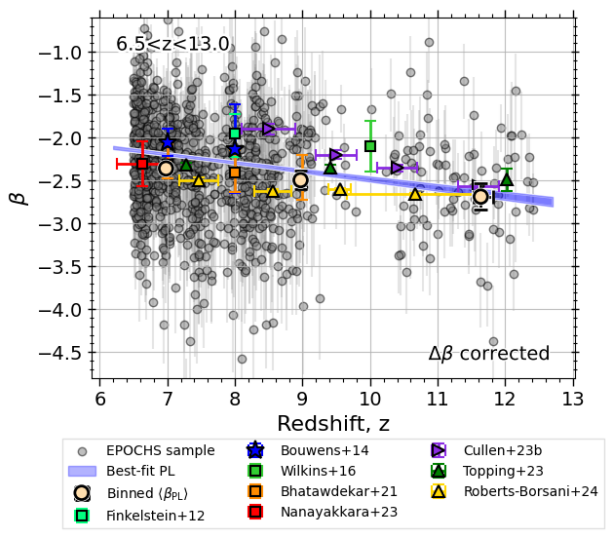

Figure 7. Bias-corrected power-law β evolution as a function of z. Black background points show measurements for individual galaxies, and beige circular points show our bootstrapped median points. The 16th–84th percentiles of the posterior power-law fit to the data, as given in Equation (6), is shown in blue. We compare our results to the observational HST studies of R. J. Bouwens et al. (2014, blue stars), S. M. Wilkins et al. (2016, lime green squares), and R. Bhatawdekar & C. J. Conselice (2021, orange squares), and more recent JWST work by T. Nanayakkara et al. (2023, red squares), F. Cullen et al. (2024, purple triangles), M. W. Topping et al. (2024a, dark green triangles), and G. Roberts-Borsani et al. (2024, yellow triangles).

Table 3
Bootstrapped Binned Results of Median z and Bias-corrected Power-law β for Our EPOCHS-III Sample as Plotted In Figure 7

z Bin	$N_{\rm gals}$	$\langle z\rangle$	$\langle\beta\rangle$	$\langle M_{\rm UV}\rangle$
$6.5 < z < 8.5$	823	$6.98^{+0.03}_{-0.04}$	$-2.36^{+0.03}_{-0.03}$	$-19.27^{+0.79}_{-0.75}$
$8.5 < z < 11$	138	$8.97^{+0.04}_{-0.03}$	$-2.50^{+0.11}_{-0.10}$	$-19.54^{+0.51}_{-0.74}$
$11 < z < 13$	50	$11.64^{+0.19}_{-0.10}$	$-2.69^{+0.15}_{-0.15}$	$-19.79^{+0.53}_{-0.56}$

Note. We show median $M_{\rm UV}$ values in each redshift bin with the errors representing the 16th–84th percentiles of the $M_{\rm UV}$ distribution. It is clear that at higher redshift our EPOCHS-III selection criteria select, on average, intrinsically brighter sources.

average $M_{\rm UV}$ of the galaxy sample. The differences may be explained by the dependence of $d\beta/dz$ on the average intrinsic UV brightness of the galaxy sample, as noted by M. W. Topping et al. (2024a), with brighter $\langle M_{\rm UV}\rangle$ samples showing a steeper evolution. Our $\langle M_{\rm UV}\rangle = -19.35$ is brighter than that of M. W. Topping et al. (2024a), who measure $-18.61 < \langle M_{\rm UV}\rangle < -18.16$ in their 0.78–1.15 μm dropout samples from deep JADES data in GOODS-South. At $z \simeq \{9.5, 10.5, 11.5\}$, F. Cullen et al. (2024) measure $\langle M_{\rm UV}\rangle = \{-18.9 \pm 0.8, -19.5 \pm 0.7, -19.1 \pm 0.5\}$ in their combined sample, although their $\langle M_{\rm UV}\rangle = -21.2 \pm 1.6$ at $7.5 < z < 9$ is significantly brighter due to their use of much wider ground-based COSMOS/UltraVISTA data, which drives their measured $d\beta/dz$ steeper as a result of their redder $\langle\beta\rangle$ at $z \simeq 8$–8.5. The stacked spectroscopic results of G. Roberts-Borsani et al. (2024) at $z > 5$ yield $d\beta/dz = -0.06 \pm 0.01$, deviating from our results by $\simeq 2.6\sigma$.

We test the $M_{\rm UV}$ dependence of our derived $d\beta/dz$ by splitting our sample into bright ($M_{\rm UV} < -19.5$) and faint ($M_{\rm UV} > -19.5$) subsamples before repeating our $\beta - z$ power-law fitting procedure. In our faint ($\langle M_{\rm UV}\rangle = -18.94$) and bright ($\langle M_{\rm UV}\rangle = -19.92$) subsamples, we measure $d\beta/dz = -0.108 \pm 0.015$ and $d\beta/dz = -0.092 \pm 0.013$, respectively. It is clear that there exists no clear evolution in β–z with $M_{\rm UV}$ in our sample, which we attribute to the flatter $d\beta/dM_{\rm UV}$ found in this work compared to the works of F. Cullen et al. (2024), M. W. Topping et al. (2024a), and R. J. Bouwens et al. (2014). This highlights the susceptibility of conclusions related to the evolution of sample-averaged β to minor differences in SFG selection criteria between different studies. A further discussion regarding trends with $M_{\rm UV}$ is presented in Section 4.2.

Our derived β–z slope implies that over cosmic time there is an increasing metal enrichment and dust content within galaxies. We compare our results to the representative UV continuum slope of dwarf galaxies enriched by Pop III stars, given as $\langle\beta\rangle = -2.51 \pm 0.07$ by J. Jaacks et al. (2018). Our Equation (6) suggests that this transition occurs at a redshift $z = 10.3$, although we note that this is later than suggested by the β–z fits of F. Cullen et al. (2024) and M. W. Topping et al. (2024a), who measure $z = 11.1$ and $z = 14.3$, respectively.

4.2. Correlations with M_{UV} Magnitude

We next analyze the trends of observed β with $M_{\rm UV}$, with β calculated using both methods explained in Section 3. We correct our power-law β results using the average correction factors outlined in Section 3.5 based on interpolated $m_{\rm UV}$, β, and z. Results using bias-corrected power-law β measurements are shown in Figure 8, where we split the galaxies into our three redshift bins ($6.5 < z < 8.5$, $8.5 < z < 11$, and $11 < z < 13$). We calculate bootstrapped median $\langle M_{\rm UV}\rangle$ and $\langle\beta\rangle$ for our sample (in two, three, and four magnitude bins, respectively, for the $6.5 < z < 8.5$, $8.5 < z < 11$, and $11 < z < 13$ redshift bins) following the same procedure introduced in Section 4.1, with $\langle\beta\rangle$ and $\langle M_{\rm UV}\rangle$ for each bin given in Table 4. Additionally, we quantify the amplitude and slope of these relations by fitting a power law of the form

$$\beta = \frac{d\beta}{d\,M_{\rm UV}}(M_{\rm UV} + 19) + \beta(M_{\rm UV} = -19) \tag{7}$$

to each individual data point in our three redshift bins to allow direct comparison with recent JWST studies on β (e.g., M. W. Topping et al. 2024a; F. Cullen et al. 2024). The fitted amplitude at $M_{\rm UV} = -19$, $\beta(M_{\rm UV} = -19)$, and slope, $d\beta/dM_{\rm UV}$, for fits using SED-fitting β as well as both bias-corrected and uncorrected power-law β are given in Table 5 and plotted in relation to other observation results in Figure 9.

We compare our results with binned observational studies from both HST (R. J. Bouwens et al. 2012; J. S. Dunlop et al. 2012; S. L. Finkelstein et al. 2012; J. S. Dunlop et al. 2013; R. J. Bouwens et al. 2014; R. Bhatawdekar & C. J. Conselice 2021) and JWST (M. W. Topping et al. 2024a; F. Cullen et al. 2024; G. Roberts-Borsani et al. 2024) in the left-hand panels of Figure 8. In addition, we also plot individual galaxies from both S. M. Wilkins et al. (2016) and A. M. Morales et al. (2023) as starred points. In addition to observational comparisons, we also compare to a wide range of simulated results from THESAN (R. Kannan et al. 2022; $z = \{7, 9\}$), SC-SAM GUREFT (L. Y. A. Yung et al. 2023; L. Y. A. Yung et al. 2024a; $z = \{7, 9, 11\}$), DELPHI (V. Mauerhofer & P. Dayal 2023; $z = \{7.1, 9.1, 12.2\}$), FLARES (C. C. Lovell et al. 2021;

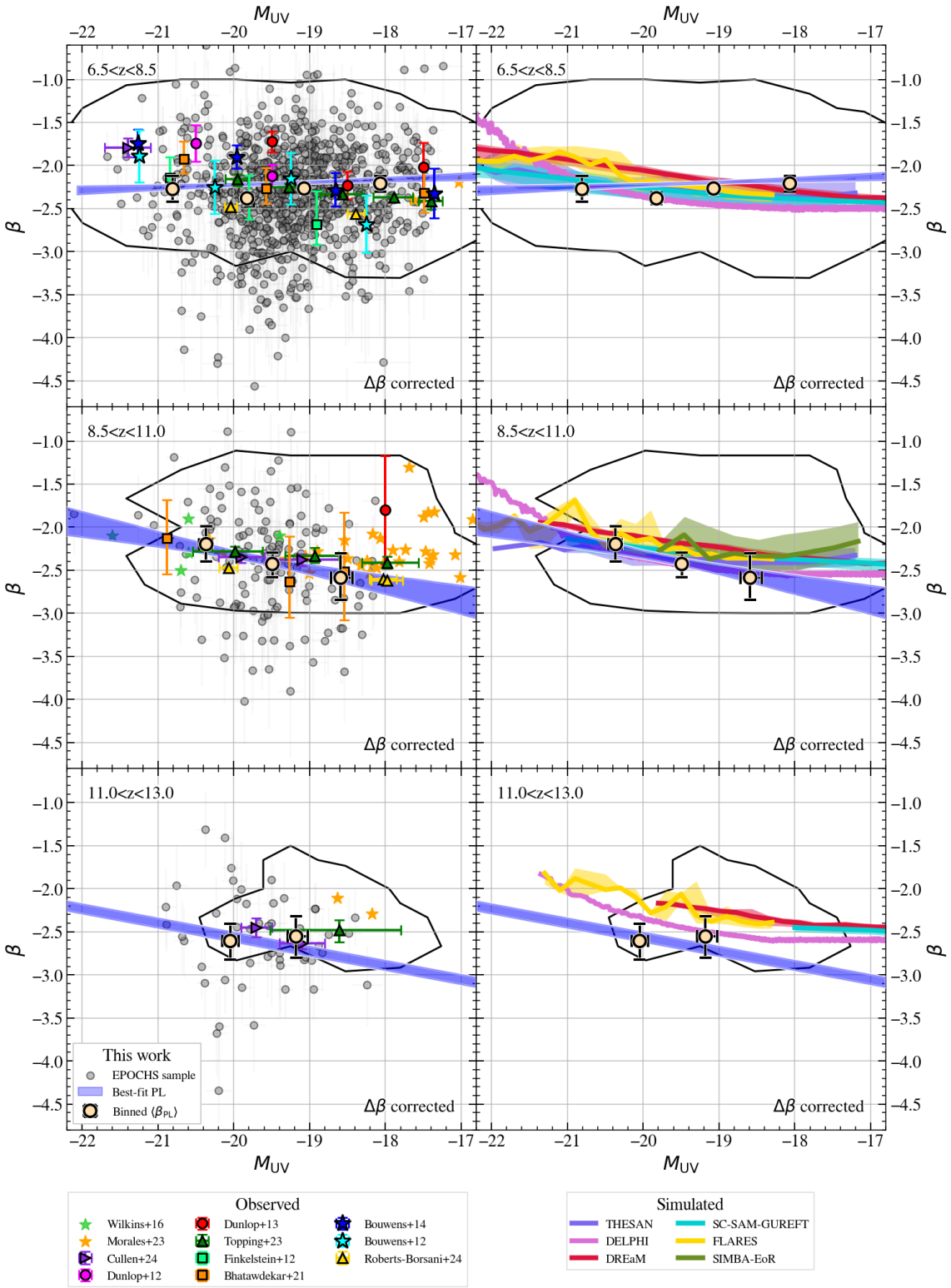

Figure 8. β–$M_{\rm UV}$ split by redshift for $6.5 < z < 8.5$ (upper), $8.5 < z < 11.0$ (middle), and $11.0 < z < 13.0$ (lower). The shaded blue line shows the 16th–84th percentiles of the fit to the power-law β bias-corrected EPOCHS-III sample (black background points), with the slope at $11.0 < z < 13.0$ bin fixed to that at $8.5 < z < 11.0$. Comparisons to observations (S. L. Finkelstein et al. 2012; J. S. Dunlop et al. 2012; R. J. Bouwens et al. 2012; J. S. Dunlop et al. 2013; R. J. Bouwens et al. 2014; S. M. Wilkins et al. 2016; R. Bhatawdekar & C. J. Conselice 2021; M. W. Topping et al. 2024a; A. M. Morales et al. 2024; F. Cullen et al. 2024; G. Roberts-Borsani et al. 2024) and simulations—THESAN (R. Kannan et al. 2022; $z = \{7, 9\}$), SC-SAM GUREFT (L. Y. A. Yung et al. 2024a, 2024b; $z = \{7, 9, 11\}$), DELPHI (V. Mauerhofer & P. Dayal 2023; $z = \{7.1, 9.1, 12.2\}$), FLARES (C. C. Lovell et al. 2021; A. P. Vijayan et al. 2021; S. M. Wilkins et al. 2023b; $z = \{7, 9, 12\}$), DREaM (N. E. Drakos et al. 2022; $z = \{6.5, 8.5, 11\}$), and SIMBA-EoR (R. Davé et al. 2019; X. Wu et al. 2020; $z = 9$)—are plotted in the left and right panels, respectively. The black lines show limits of the JAGUAR catalog, which mimics the JADES observations.

Table 4
Bootstrapped Binned Results of Median $M_{\rm UV}$ and Bias-corrected Power-law β for Our EPOCHS-III Sample as Plotted in Figure 8

$M_{\rm UV}$ Bin	$\langle M_{\rm UV}\rangle$	$\langle\beta\rangle$
$6.5 < z < 8.5$		
$M_{\rm UV} < -20.5$	$-20.81^{+0.06}_{-0.07}$	$-2.27^{+0.15}_{-0.15}$
$-20.5 < M_{\rm UV} < -19.5$	$-19.82^{+0.03}_{-0.04}$	$-2.38^{+0.07}_{-0.07}$
$-19.5 < M_{\rm UV} < -18.5$	$-19.07^{+0.03}_{-0.03}$	$-2.27^{+0.05}_{-0.06}$
$M_{\rm UV} > -18.5$	$-18.07^{+0.05}_{-0.05}$	$-2.21^{+0.09}_{-0.09}$
$8.5 < z < 11.0$		
$M_{\rm UV} < -20.0$	$-20.36^{+0.08}_{-0.10}$	$-2.20^{+0.21}_{-0.20}$
$-20.0 < M_{\rm UV} < -19.0$	$-19.49^{+0.05}_{-0.05}$	$-2.43^{+0.13}_{-0.16}$
$M_{\rm UV} > -19.0$	$-18.59^{+0.15}_{-0.13}$	$-2.59^{+0.28}_{-0.26}$
$11.0 < z < 13.0$		
$M_{\rm UV} < -19.5$	$-20.05^{+0.11}_{-0.10}$	$-2.61^{+0.20}_{-0.21}$
$M_{\rm UV} > -19.5$	$-19.18^{+0.16}_{-0.12}$	$-2.55^{+0.24}_{-0.25}$

Note. We show results at $6.5 < z < 8.5$ in four $M_{\rm UV}$ bins, as well as in three and two bins at the higher redshifts of $8.5 < z < 11$ and $11 < z < 13$, respectively.

A. P. Vijayan et al. 2021; S. M. Wilkins et al. 2023b; $z = \{7, 9, 11\}$), DREaM (N. E. Drakos et al. 2022; $z = \{6.5, 8.5, 11\}$), and SIMBA-EoR (R. Davé et al. 2019; X. Wu et al. 2020; $z = 9$). It is challenging to identify the reasons for the differences between these simulations due to the differing initial assumptions made and techniques used. For the most part, however, there is no large discrepancy between the simulations at $6.5 < z < 8.5$, although they begin to diverge at $11 < z < 13$. This is most likely due to the fact that these simulations are often calibrated to observational results, more of which are available from HST at $z \simeq 7$ than at $z \simeq 12$. When comparing to these studies, our results show a far flatter $d\beta/dM_{\rm UV}$ in our lowest-redshift bin at $6.5 < z < 8.5$ as well as much bluer β slopes at $11 < z < 13$ than the simulations (also seen in F. Cullen et al. 2024).

4.2.1. *Flat* $d\beta/dM_{UV}$ *at* $6.5 < z < 8.5$

The flatter observed $d\beta/dM_{\rm UV}$ at $6.5 < z < 8.5$ could be due to a number of factors. In order for this slope to be flattened compared to other results, we could have either discovered a new population of faint red galaxies and/or missed a large population of faint blue galaxies compared to other studies. In our bias simulations in Appendix A, we have found that our SED-fitting templates favor the selection of blue galaxies over red ones, making it unlikely that we have missed a large sample of blue galaxies unless they have $\beta < -3.1$ (the bluest R. L. Larson et al. 2023 template), which is challenging to reproduce with standard SPS models and IMFs. Our sample covers less sky area than many of these other HST studies, and even the JWST work of F. Cullen et al. (2024), which contains bright $z > 7.5$ objects from COSMOS/UltraVISTA (see C. T. Donnan et al. 2023), meaning we almost certainly miss the rarer bright red galaxies at $6.5 < z < 8.5$ in this work compared to others. As well as this, we note that we could have either overcorrected for the β bias, which can reduce our $d\beta/dM_{\rm UV}$ by $\sim$0.04 toward the other observational results, or we could be impacted by sample contamination (this is explored in more detail in Section 4.4).

4.2.2. *Blue* β $(M_{UV} = -19)$ *at* $11 < z < 13$

In our highest-redshift bin, we observe a bluer β than predicted by the SC-SAM GUREFT, DELPHI, FLARES, and DREaM simulations. Previous JWST observations by M. W. Topping et al. (2024a) and F. Cullen et al. (2024) found $\beta(M_{\rm UV} = -19) = \{-2.42 \pm 0.13, -2.63 \pm 0.09\}$ at $z \simeq 12$ and $11 < z < 12$, respectively, whereas we observe bluer values of $\beta(M_{\rm UV} = -19) = -2.73 \pm 0.06$. We note that this may well be exacerbated by sample contamination, which we assess in Section 4.4, although for the rest of this subsection we explore the physical interpretation of this ultra-blue average β measurement.

We use the FLARES simulations to test the impact of changing $f_{\rm esc,LyC}$ and $A_{\rm UV}$ on both $\beta(M_{\rm UV} = -19)$ and $d\beta/dM_{\rm UV}$ in our highest-redshift $11 < z < 13$ bin. The results from FLARES that are plotted in Figure 8 assume $f_{\rm esc,LyC} = 0$ with the dust attenuation switched on. We find that turning this dust attenuation off both changes $\beta(M_{\rm UV} = -19)$ by $\simeq -0.2$ to $\beta(M_{\rm UV} = -19) \simeq -2.53$ and flattens the slope from $\simeq -0.2$ to $\simeq 0.0$. The FLARES $d\beta/dM_{\rm UV}$ predictions are approximate only as their $\beta - M_{\rm UV}$ does not strictly follow a power law. Since our measured $11 < z < 13 d\beta/dM_{\rm UV} \simeq -0.2$ (which is fixed to the slope in the $8.5 < z < 11$ bin) is similar to the dusty FLARES simulations, we conclude that turning off the dust law completely does not adequately solve the problem. If we additionally switch off the galactic nebular emission (i.e., by setting $f_{\rm esc,LyC} = 1$), we obtain a significantly bluer $\beta(M_{\rm UV} = -19) \simeq -2.78$ and shallower $d\beta/dM_{\rm UV} \simeq -0.05$. We therefore conclude that a combination of a reduction in dust attenuation and increase in LyC escape fraction is expected toward higher redshifts. If the v2.2.1 BPASS SPS models (E. R. Stanway & J. J. Eldridge 2018) and G. Chabrier (2003) IMF assumed in FLARES are indeed correct, then a galaxy at $M_{\rm UV} = -19$ is expected to be completely dust-free with $f_{\rm esc,LyC} = 1$ in order to match our observations.

The FLARES multicomponent dust model calculates the UV optical depth by including contributions from both the ISM, $\tau_{\rm ISM}$, as well as additional attenuation from young stars in BCs $<$10 Myr old, $\tau_{\rm BC}$ (S. Charlot & S. M. Fall 2000). These V-band optical depths are calibrated by the dust-to-metal (see Equation (15) from A. P. Vijayan et al. 2019) and integrated line-of-sight metal column densities (for the ISM optical depth), and spatially resolved stellar metallicities (for $\tau_{\rm BC}$). In addition, the ISM normalizing factor, $\kappa_{\rm ISM}$, is chosen to match the $z = 5$ R. J. Bouwens et al. (2015b) UVLF, and the BC normalizing factor, $\kappa_{\rm BC}$, is chosen to match the $z = 5$ β observations from R. J. Bouwens et al. (2012, 2014) and the $z = 8$ [O III] $\lambda\lambda$4959, 5007+Hβ EW distribution from S. De Barros et al. (2019). Since we expect there to be some contribution from dust in order to retain the $d\beta/dM_{\rm UV}$ slope at these high redshifts, there may exist either a lag between dust and metal production and/or a change in grain shape, size, and composition (impacting $\kappa_{\rm ISM}/\kappa_{\rm BC}$). A more in-depth discussion of the dust implications of this work is presented in Section 5.2.

4.3. *Comparisons with Stellar Mass*

The relationship between the UV spectral slope and stellar mass of galaxies has been studied in deep blank-field surveys since the emergence of HST/WFC3-IR data at $1.0 < \lambda_{\rm obs}/\mu{\rm m} < 1.6$ in the early 2010s. However, with the launch of JWST we now have access to rest-frame optical data

Table 5
Median Redshifts, Amplitudes, and Slopes for Our Power-law Fits to the β–$M_{\rm UV}$ and β–$M_\star$ Relations in Our Three Redshift Bins Ranging $6.5 < z < 13$

z Bin	$N_{\rm gals}$	$\langle z \rangle$	$\beta(M_{\rm UV} = -19)$	$d\beta/dM_{\rm UV}$	$d\beta/d\log(M_\star/M_\odot)$
$\beta_{\rm PL}$ ($\beta_{\rm PL,corr}$)					
$6.5 < z < 8.5$	823	$6.98^{+1.01}_{-0.39}$	$-2.28(-2.19) \pm 0.01$	$-0.01(0.03) \pm 0.02$	$0.22(0.22) \pm 0.02$
$8.5 < z < 11$	138	$8.97^{+1.56}_{-0.38}$	$-2.59(-2.49) \pm 0.06$	$-0.19(-0.17) \pm 0.06$	$0.29(0.31) \pm 0.06$
$11 < z < 13$	50	$11.64^{+0.49}_{-0.43}$	$-2.83(-2.73) \pm 0.06$	$-0.19(-0.17)^{\dagger}$	$0.70(0.81) \pm 0.13$
$\beta_{\rm SED}$					
$6.5 < z < 8.5$	823	$6.98^{+1.01}_{-0.39}$	-2.40 ± 0.01	-0.03 ± 0.02	0.09 ± 0.01
$8.5 < z < 11$	138	$8.97^{+1.56}_{-0.38}$	-2.48 ± 0.02	-0.05 ± 0.03	0.09 ± 0.04
$11 < z < 13$	50	$11.64^{+0.49}_{-0.43}$	-2.53 ± 0.02	$-0.05^{\dagger}$	0.18 ± 0.07

Note. We show results using both the power-law ($\beta_{\rm PL}$) and SED-fitting ($\beta_{\rm SED}$) methods to measure β. In the upper panel results for the bias-corrected power-law β are shown in brackets, and have the same error as the uncorrected values. In our highest-redshift bin ($11 < z < 13$), we fix the slope of our β–$M_{\rm UV}$ to that of our $8.5 < z < 11$ bin (shown by †).

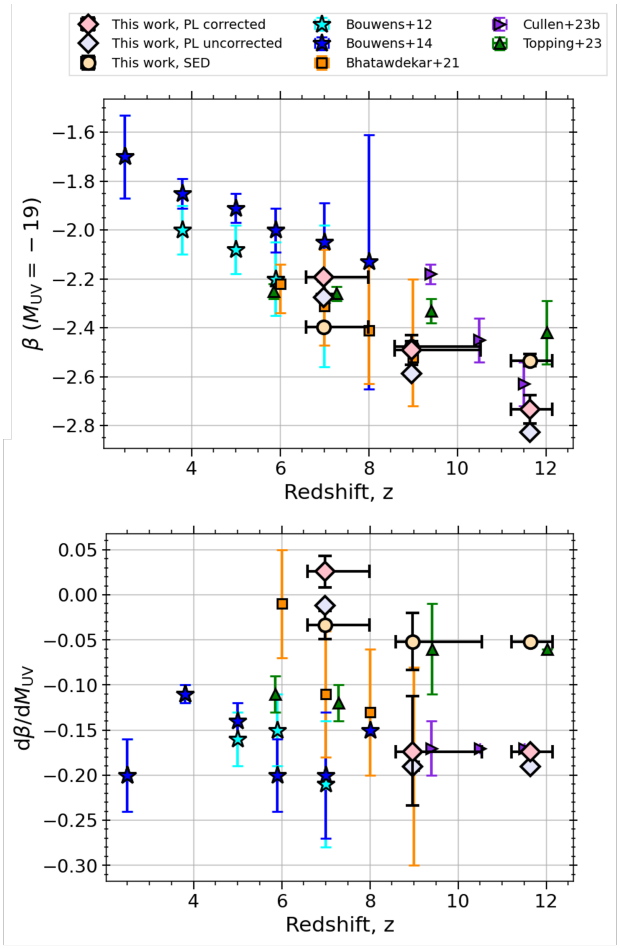

Figure 9. Amplitude (upper panel) and power-law slope (lower panel) of the β–$M_{\rm UV}$ relations in Figure 8 showing the redshift evolution of $\beta(M_{\rm UV} = -19)$ and $d\beta/dM_{\rm UV}$, respectively, as defined in Equation (7). β results for both the bias-corrected/uncorrected power-law (pink/turquoise diamonds) and SED-fitting (beige circles) methods are shown. Observational results collated from the literature from HST (R. J. Bouwens et al. 2012, 2014; R. Bhatawdekar & C. J. Conselice 2021) and JWST (F. Cullen et al. 2024; M. W. Topping et al. 2024a) are also plotted.

up to $z \sim 7$–8, allowing for better constraints on stellar masses at high redshift, which presents an ideal opportunity to investigate this relation further.

We plot our bias-corrected power-law β values against our Bagpipes-derived $\log_{10} M_\star$ in Figure 10, fitting a power-law function of the form

$$\beta = \beta_0 + \frac{d\beta}{d\log_{10}(M_\star/M_\odot)} \log_{10}(M_\star/M_\odot), \quad (8)$$

where $\beta_0 = \beta(\log_{10}(M_\star/M_\odot) = 0)$ is a physically meaningless normalization factor. The limits of the JADES JAGUAR catalog are shown in black. Observational (S. L. Finkelstein et al. 2012; R. Bhatawdekar & C. J. Conselice 2021) and simulated results from DELPHI (V. Mauerhofer & P. Dayal 2023), SC-SAM GUREFT (L. Y. A. Yung et al. 2024a, 2024b), DREaM (N. E. Drakos et al. 2022), and FLARES (C. C. Lovell et al. 2021; A. P. Vijayan et al. 2021; S. M. Wilkins et al. 2023b) are shown in the left-hand panel. We additionally show results using the Atacama Large Millimeter/submillimeter Array (ALMA) from R. J. McLure et al. (2018) and R. Bouwens et al. (2020). Bootstrapped median $\langle\beta\rangle$ and $\langle\log_{10} M_\star\rangle$ values in stellar mass bins are given in Table 6, and $d\beta/d\log_{10}(M_\star/M_\odot)$ for bias-corrected/uncorrected power-law $\beta_{\rm PL}$ and Bagpipes$\beta_{\rm SED}$ are tabulated in Table 5 and plotted in comparison to observational results from S. L. Finkelstein et al. (2012) and R. Bhatawdekar & C. J. Conselice (2021) in Figure 11.

In our lowest-redshift bin in Figure 10, we see that the bootstrapped median points do not match the best-fit power law to the individual galaxies particularly well. While the choice of bin size plays a role here, we note that a power law is probably not the best-fitting function to use in the future, although we use it here to provide direct comparisons to previous HST studies.

The two most important takeaways from Figure 10, however, are that the slope at $6.5 < z < 8.5$ and $8.5 < z < 11$ is shallower than observed by both S. L. Finkelstein et al. (2012) and R. Bhatawdekar & C. J. Conselice (2021) due to the presence of a large sample of low-mass ($M_\star \sim 10^{7.5} M_\odot$) red ($-2 \lesssim \beta \lesssim -1$) galaxies, and that the slope at $11 < z < 13$ is much steeper than at lower redshift due to the nondetection of these low-mass red objects.

4.3.1. *Shallow* dβ/dM$_\star$ *at* $6.5 < z < 8.5$

While we do not go as deep as R. Bhatawdekar & C. J. Conselice (2021), who utilize the strong gravitational

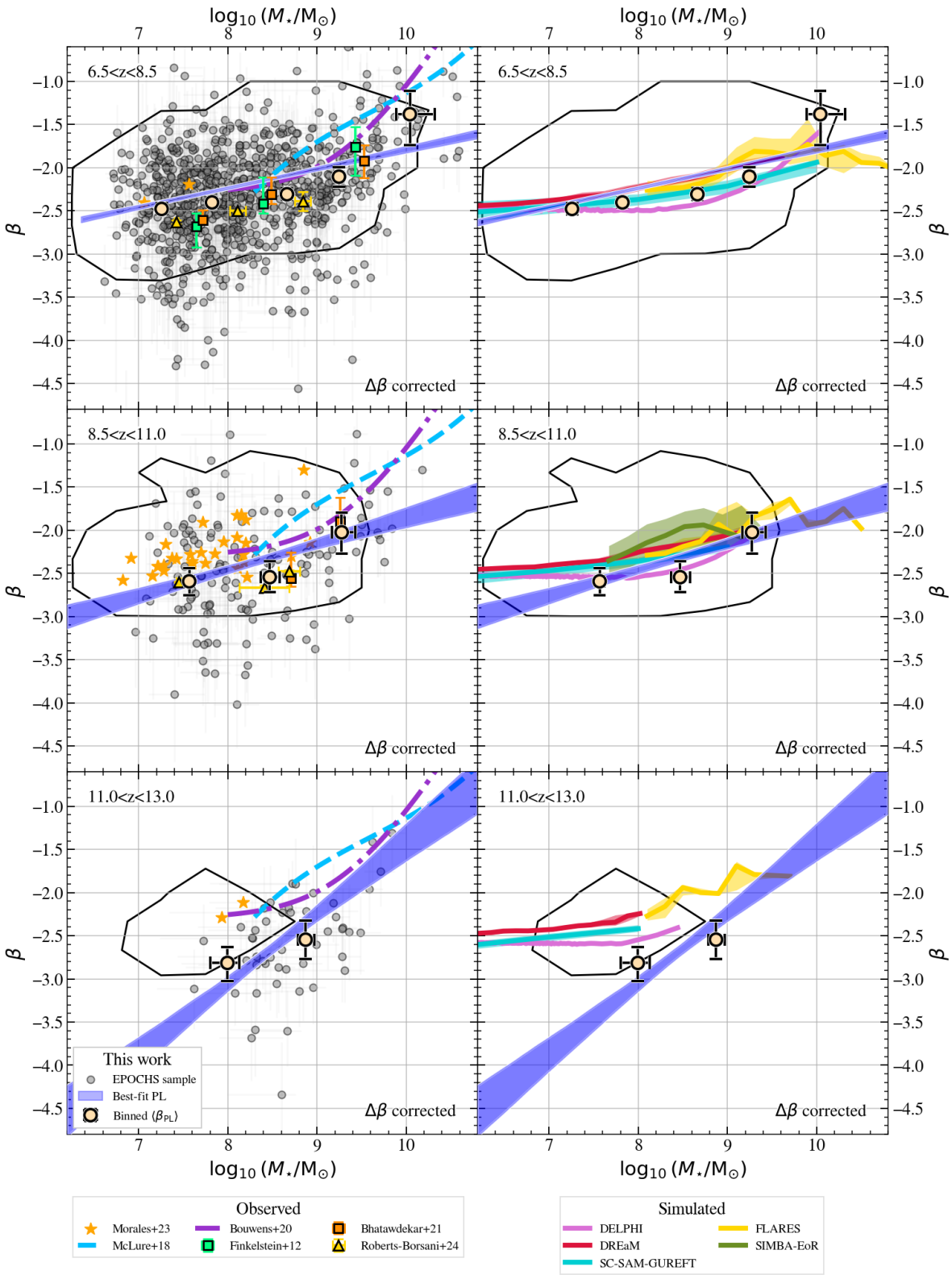

Figure 10. Redshift evolution of β–$M_\star$ for our EPOCHS-III sample, where the power-law-measured β has been bias corrected. Bootstrapped median points are shown as beige circles, with individual galaxies in gray and the 16th–84th percentiles of the power-law fit shown in blue. We compare to observations in the optical/NIR from HST/JWST (S. L. Finkelstein et al. 2012; R. Bhatawdekar & C. J. Conselice 2021; A. M. Morales et al. 2024; G. Roberts-Borsani et al. 2024) and far-IR from ALMA (R. J. McLure et al. 2018; R. Bouwens et al. 2020), as well as simulations—SC-SAM GUREFT (L. Y. A. Yung et al. 2024a, 2024b; $z = \{7, 9, 11\}$), DELPHI (V. Mauerhofer & P. Dayal 2023; $z = \{7.1, 9.1, 12.2\}$), FLARES (C. C. Lovell et al. 2021; A. P. Vijayan et al. 2021; S. M. Wilkins et al. 2023b; $z = \{7, 9, 12\}$), DREaM (N. E. Drakos et al. 2022; $z = \{6.5, 8.5, 11\}$) and SIMBA-EoR (R. Davé et al. 2019; X. Wu et al. 2020; $z = 9$)—in the left and right panels, respectively. The black lines show limits of the JAGUAR catalog, which mimics the JADES observations.

Table 6
Bootstrapped Binned Results of Median $\log_{10}(M_\star/M_\odot)$ and Bias-corrected Power-law β for Our EPOCHS-III Sample as Plotted In Figure 10

$\log_{10}(M_\star/M_\odot)$ Bin	$\langle\log_{10}(M_\star/M_\odot)\rangle$	$\langle\beta\rangle$
$6.5 < z < 8.5$		
$\log_{10}(M_\star/M_\odot) < 7.5$	$7.26^{+0.02}_{-0.02}$	$-2.48^{+0.07}_{-0.07}$
$7.5 < \log_{10}(M_\star/M_\odot) < 8.25$	$7.82^{+0.03}_{-0.03}$	$-2.40^{+0.06}_{-0.06}$
$8.25 < \log_{10}(M_\star/M_\odot) < 9.0$	$8.66^{+0.03}_{-0.03}$	$-2.31^{+0.07}_{-0.07}$
$9.0 < \log_{10}(M_\star/M_\odot) < 9.75$	$9.25^{+0.05}_{-0.05}$	$-2.10^{+0.11}_{-0.11}$
$\log_{10}(M_\star/M_\odot) > 9.75$	$10.04^{+0.28}_{-0.15}$	$-1.38^{+0.27}_{-0.36}$
$8.5 < z < 11.0$		
$\log_{10}(M_\star/M_\odot) < 8.0$	$7.57^{+0.05}_{-0.05}$	$-2.59^{+0.16}_{-0.16}$
$8.0 < \log_{10}(M_\star/M_\odot) < 9.0$	$8.47^{+0.11}_{-0.10}$	$-2.54^{+0.18}_{-0.18}$
$\log_{10}(M_\star/M_\odot) > 9.0$	$9.28^{+0.15}_{-0.11}$	$-2.02^{+0.23}_{-0.25}$
$11.0 < z < 13.0$		
$\log_{10}(M_\star/M_\odot) < 8.5$	$8.00^{+0.13}_{-0.19}$	$-2.81^{+0.18}_{-0.21}$
$\log_{10}(M_\star/M_\odot) > 8.5$	$8.87^{+0.09}_{-0.09}$	$-2.55^{+0.22}_{-0.23}$

Note. We show results at $6.5 < z < 8.5$ in five $\log_{10}(M_\star/M_\odot)$ bins, as well as in three and two bins at the higher redshifts of $8.5 < z < 11$ and $11 < z < 13$, respectively. The positive $d\beta/d\,M_\star$ slope is evident from these values in all three redshift bins.

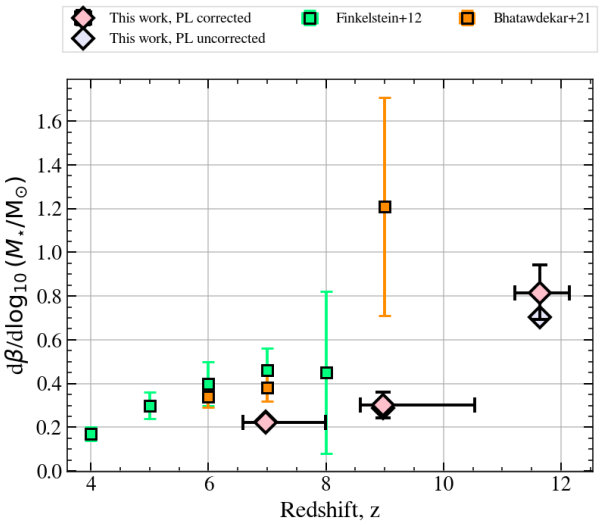

Figure 11. Evolution of the slope of the β–$M_\star$ relation, $d\beta/d\log(M_\star/M_\odot)$, for both our bias-corrected (pink diamonds) and uncorrected (turquoise diamonds) power-law β measurements. We compare our results to those given in S. L. Finkelstein et al. (2012, lime green) and R. Bhatawdekar & C. J. Conselice (2021, orange), which use the SED-fitting method to measure β. Consistently shallower results are measured at $z \simeq 7$ and $z \simeq 9$, and the first measurement at $z \simeq 11.5$ is shown. We caution that we may be completeness dominated in the highest-redshift bin.

lens of the MACS-0416 cluster to probe down to $M_{\rm UV} \lesssim -13.5$ at $z = 6$, we notice that our selection criteria detect faint ($M_{\rm UV} \simeq -17.5$), low-mass red objects more efficiently than their bluer counterparts. The reasoning behind this is somewhat unclear and depends on the difference in selection criteria used, although we note that these redder β could potentially become accessible due to the increased rest-frame UV coverage up to 3000 Å provided by the F200W and F277W JWST/NIRCam wideband filters compared to HST/WFC3-IR. The extent to which we are able to select these low-mass red objects with JWST is apparent when comparing the 20% completeness curves plotted in Figure 10 to those by S. L. Finkelstein et al. (2012) and R. Bhatawdekar & C. J. Conselice (2021; see their Figures 7 and 6, respectively). At $z \simeq 7$, these pre-JWST completeness curves do not cover detections of galaxies redder than $\beta \simeq -2$ at $\log_{10}(M_\star/M_\odot) = 7.5$, whereas our JAGUAR completeness curves extend to $\beta \simeq -1.6$ at $6.5 < z < 8.5$.

4.3.2. Steepening of dβ/dM⋆ with Increasing Redshift

From Figure 11, we can see that our $d\beta/d\log(M_\star/M_\odot)$ increases significantly in our highest-redshift bin from 0.31 ± 0.06 at $8.5 < z < 11$ to 0.81 ± 0.13 at $11 < z < 13$ due to the nondetection of low-mass red galaxies that are seen in the lower-redshift bins. At $11 < z < 13$, the most massive galaxies at $M_\star = 10^{9.5}\,M_\odot$ are very red (with the reddest having $\beta = -1.3$), meaning that dust formation channels must already exist at these redshifts. Due to the young ages of these galaxies, Type II SNe are the most promising candidates as the major dust production mechanism. Since such red galaxies are not observed at lower masses, it is likely that the dust produced by these Type II SNe is lost in outflows instead of being retained by the large gravitational potential wells of the most massive galaxies (S. L. Finkelstein et al. 2012).

While our JAGUAR 20% completeness contours suggest that this parameter space should be detectable, we note that there are few galaxies in our JAGUAR simulation at $11 < z < 13$. This is complemented by the fact that the JAGUAR mock SEDs may not adequately reproduce the real Universe at high redshift, meaning that our completeness contours may not accurately represent the real completeness limits in this redshift bin. Galaxies with $\beta \gtrsim -2$, such as our sample of NIRCam-selected red sources, lie outside of the HST 20% completeness contours of S. L. Finkelstein et al. (2012) and R. Bhatawdekar & C. J. Conselice (2021), meaning that these studies are likely completeness limited at these redshifts. In our highest-redshift bin, we therefore cannot conclude that the trend is not induced by sample incompleteness since previous studies seem to have been.

4.3.3. Analysis of Potential β–M⋆ Biases

We now analyze the potential biases stemming from the coupling of β and $M_\star$ measurement errors which would potentially drive trends in our β–$M_\star$ relation. Two tests are performed, the first simulating the impact of photometric noise on an assumed β–$M_\star$ relation using mock galaxy SEDs from the JAGUAR catalog, and the second looking at the impact of a lack of rest-frame optical data on the stellar mass measurements.

For the first simulation, mock photometric data are produced from the JAGUAR catalog adopting the CEERS filter set, with errors derived assuming the average CEERS depth profile. The flux measurements are then scattered within their photometric errors. β and $M_\star$ measurements are made for both the scattered and unscattered photometry following the same techniques used on the real data (and using the fiducial Bagpipes setup) on a subset of 876 galaxies at $6.5 < z < 13$ detected at SNR > 5 in the first two bands redwards of Lyα, with all other wide bands having SNR > 2, approximately mimicking the

selection criteria outlined in Section 2.5. Negligible differences in both β_0 and $d\beta/d\log_{10}(M_\star/M_\odot)$ are found.

To test the bias induced by a lack of rest-frame optical data at the highest $z > 11$ sources in our sample, we recompute the stellar masses for our robust sample with the same fiducial `Bagpipes` setup excluding filters covering rest-frame wavelengths $\lambda_{\rm rest} < 3400$ Å. As a result, we observe a steepening of $d\beta/d\log_{10}(M_\star/M_\odot)$ by a factor $\sim$2 due to an average stellar mass overestimation of the least massive and underestimation of the most massive sources. The steepening of $\mathrm{d}\beta/\mathrm{d}\log_{10}(M_\star/M_\odot)$ in our highest-redshift ($11 < z < 13$) bin outlined in Section 4.3.2 may indeed be produced entirely by this bias.

4.4. The Impact of Sample Contamination

As in all galaxy samples, there will be some contaminant objects in our sample; these most likely arise as lower-redshift galaxy interlopers due to the Balmer–Lyman break degeneracy. In this work, we predict the number of these interlopers we expect to find using the `JAGUAR` simulation (C. C. Williams et al. 2018), as explained in more detail in Section 2.6. We assign a contamination percentage likelihood to each galaxy dependent on its origin survey and position in the ($M_{\rm UV}$, β) and ($M_\star$, β) parameter spaces. Adding these percentages together, we expect our sample to have {40–90/823, 6–15/138, and 2–3/50} contaminants in the respective $6.5 < z < 8.5$, $8.5 < z < 11$, and $11 < z < 13$ redshift bins (which are likely to be the bluest in our sample) corresponding to 5%–10%. This, of course, assumes that the distribution of galaxy colors in `JAGUAR` matches the real Universe, and may not accurately represent the real contamination in our sample. A thorough comparison of the colors of simulations, including `JAGUAR`, with NIRCam wideband photometric data from the CEERS survey is presented in S. M. Wilkins et al. (2023a). Consequently, our simulation work identifies which regions of parameter space may be subject to contamination, but the precise contamination level may not be reliable. The reconciliation of this potential systematic is deemed beyond the scope of this work.

We exclude objects from our relationship fits that lie in the regions of parameter space found to have 10%, 25%, and 50% contamination likelihood according to our `JAGUAR`-based simulations and refit our β–$M_{\rm UV}$ and β–$M_\star$ scaling relations to observe the difference that this has on our results. We perform the power-law fitting of Equation (7) in the same fashion as in Figure 7, except this time we weight each galaxy, i, by a factor $w_i = 1 - \mathrm{Cont}_i(M_{\rm UV}, \beta)$, where $\mathrm{Cont}_i(M_{\rm UV}, \beta)$ is calculated for each galaxy as explained in Section 2.6.

The impact of this on our β–$M_{\rm UV}$ fits is plotted in Figure 12. We find that the largest impact on the power-law slope of our β–$M_\star$ relation occurs at $6.5 < z < 8.5$, where we observe a decrease of $\simeq$0.043 from $d\beta/dM_{\rm UV} = 0.026 \pm 0.017$ to $d\beta/dM_{\rm UV} = -0.017 \pm 0.017$ when removing all galaxies with contamination likelihood >10%. Negligible evolution in $d\beta/dM_{\rm UV}$ is observed at $z > 8.5$. We also observe a significant reddening of $\beta(M_{\rm UV} = -19)$ by $\simeq$0.07 ($6.5 < z < 8.5$), $\simeq$0.10 ($8.5 < z < 11$), and $\simeq$0.16 ($11 < z < 13$) when removing contaminant galaxies with contamination likelihood >10%. This somewhat dampens our discussion on blue β slopes should this high level of contamination be accurate, although we note that even with this reddening we still observe

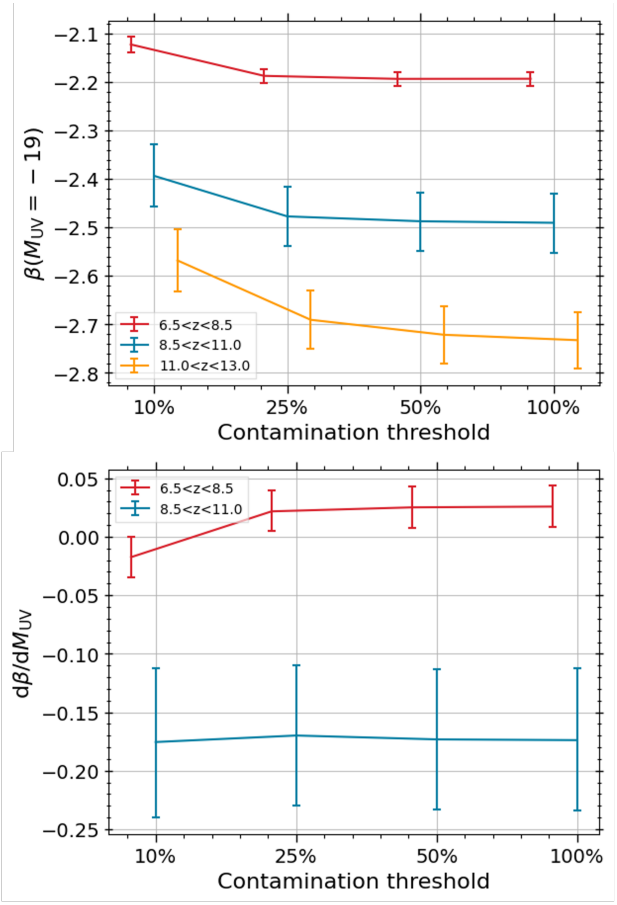

Figure 12. The impact of `JAGUAR`-estimated contamination on the amplitude (at $M_{\rm UV} = -19$; top panel) and slope (bottom panel) on our power-law β bias-corrected β–$M_{\rm UV}$ relation measured in our three redshift bins. Shown on the right are the results when no contaminant objects are removed, and moving leftwards we remove objects with $\mathrm{Cont}(M_{\rm UV}, \beta) < \{0.5, 0.25, 0.1\}$. Since we fix the $11 < z < 13$ slope, the trend of $d\beta/dM_{\rm UV}$ with contamination removal percentage in the lower panel matches the $8.5 < z < 11$ bin.

$\beta(M_{\rm UV} = -19) = -2.57 \pm 0.06$ in our $11 < z < 13$ bin, which is still significantly bluer than the most up-to-date simulated results. Due to the small dependence on β when binning the contamination in $\Theta = (M_\star, \beta)$, we find very little impact on the slope of β–$M_\star$ at any redshift.

5. Discussion

5.1. An Abundance of Faint, Low-mass Red Galaxies at $6.5 < z < 11$

In the two lowest-redshift bins of Figure 10, we observe an abundance of $\log_{10}(M_\star/M_\odot) < 8.0$, $\beta > -2$ galaxies which are missed by studies of S. L. Finkelstein et al. (2012) and R. Bhatawdekar & C. J. Conselice (2021). The abundance of these low-mass red objects observed with `JWST` may be as a result of the increased wavelength coverage extending further into the rest-frame optical at these redshifts and depths than previous HST and Spitzer studies, which has been shown to flatten the $\beta - \log_{10}(M_\star/M_\odot)$ relation in Section 4.3.3. These objects are also observed with $M_{\rm UV} \gtrsim -19$ at $6.5 < z < 8.5$, which results in a flattening of $d\beta/dM_{\rm UV}$. Comparison with other β–$M_{\rm UV}$ studies from the literature from S. L. Finkelstein et al. (2012), R. J. Bouwens et al. (2012, 2014), J. S. Dunlop et al. (2013), and F. Cullen et al. (2024) show that a similar

proportion of candidates (approximately 10%–20%) fall within this β–$M_{\rm UV}$ regime.

To test whether these faint, low-mass, $\beta > -2$ objects at $6.5 < z < 8.5$ are contaminants, we perform an inverse-variance weighted stack of the photometric data bluewards of Lyα. Out of 39 sources which meet this criteria, 38 have F606W data, while only 11 have F814W and F090W coverage, with the latter restricted to the higher redshifts within the bin. The stacked SNRs are 1.08, 1.78, and 1.33 for F606W, F814W, and F090W, respectively. While these SNRs do not rule out the possibility of contamination within this regime, they strongly suggest that contaminants do not appear to represent the dominant share of this population.

These could be a result of our failure to accurately trace the UV continuum; we may be biased red by high H I column density DLAs (already observed by JWST; see K. E. Heintz et al. 2024) or strong resonant Mg II line emission, which may help trace $f_{\rm esc,LyC}$ (J. Chisholm et al. 2020; H. Katz et al. 2022). In addition, D. Schaerer (2002) note that nebular-dominated galaxies with hard ionizing fields (large $\log U$ values) can be biased red should they exist in the real Universe. Candidate nebular-dominated galaxies, such as those presented in A. J. Cameron et al. (2024), would also provide evidence for a long hypothesized top-heavy IMF in the early Universe should they exist. We use the `synthesizer`(A. P. Vijayan et al. 2021)[33] python code to measure the expected β slope of a pure nebular-dominated galaxy using a template with assumed $\log U = -2$, BPASS v2.2 SPS model, and G. Chabrier (2003) IMF. We find $\beta_{\rm neb,C94} \simeq -1.0$ in the C94 filters (which have been seen to be biased red due to the increased wavelength coverage approaching two-photon continuum emission turnover) and $\beta_{\rm neb,2-window} \simeq -1.4$ in two rest-wavelength windows covering $\lambda_{\rm rest} = \{1250\text{–}1750, 2250\text{–}2750\}$ Å. This two-window β more accurately reflects our power-law measurement technique, and therefore any nebular-dominated galaxies, should they exist in our sample, would appear with $\beta \simeq -1.4$.

We do not attempt to quantify the number density of DLAs and nebular-dominated galaxies in our EPOCHS-III sample as the defining features of these SEDs are not traceable with the JWST/NIRCam wide bands used in these early blank-field surveys. Increased medium-band coverage utilizing JWST/NIRCam F210M, F250M, F300M, and F335M probing $2000 < \lambda_{\rm rest}/\text{Å} < 3000$ at $6.5 < z < 8.5$ can be used to both estimate Mg II EWs and detect the Balmer jump at 3646 Å in nebular-dominated galaxies. The detection of these features in unbiased medium-band photometric surveys, and subsequent modeling of the expected number densities of these systems, will allow us to distinguish whether these red galaxies are indeed as dusty as their red β suggests.

5.2. Dust Implications

From the results of our β–$M_\star$ relations, we propose possible scenarios for the average buildup of galactic dust. We start in our highest-redshift bin at $11 < z < 13$, where we observe a steep $d\beta/d\log_{10}(M_\star/M_\odot) = 0.81 \pm 0.13$. The most massive galaxies in this redshift bin have $M_\star \simeq 10^{9.5}\,M_\odot$ and $\beta \simeq -1.5$, meaning galactic dust must have been formed at these epochs. Due to the relatively young ages of galaxies at these redshifts, we attribute this to dust formed in Type II SNe on the smallest $\sim$10 Myr timescales (see also S. L. Finkelstein et al. 2012). Since these SNe must also occur in the lowest-mass systems, the lack of observed red, $M_\star < 10^8\,M_\odot$ galaxies means that this dust is not retained, most likely via SNe feedback-induced outflows that remove dust from the small gravitational potential wells of the low-mass host galaxies.

As well as this, O/B main-sequence stars may also remove gas and dust via radiation-pressure-driven outflows, which are expected to dominate over SNe for high-specific-SFR systems, which is particularly relevant for low-mass, bursty galaxies (A. Ferrara 2024). These outflows may also be prominent in high-mass galaxies, with the β–$M_\star$ slope being a reflection of the increased clearing timescale. Additional possibilities for the lack of observed dust in low-mass systems may stem from spatial segregation of UV-emitting regions and dust (F. Ziparo et al. 2023), or more efficient ISM grain–grain shattering in SNe reverse shocks (F. Kirchschlager et al. 2022).

Following the initial phase of Type II SNe-dominated dust production at $z > 11$, we observe an average reddening in galaxies across all stellar masses. This reddening is more prominent for the lower-mass galaxies, which flattens the slope of the β–$M_\star$ relation. One plausible explanation for this reddening is by dust production on slightly longer timescales than Type II SNe from short-lived WC stars, which have been seen to produce copious amounts of dust (10^{-10}–$10^{-6}\,M_\odot\,{\rm yr}^{-1}$ per WC) in the local Universe (R. M. Lau et al. 2020). This production mechanism has been somewhat overlooked in the past due to the requirement of an O/B main-sequence companion star for efficient dust production, however with newer BPASS SPS models this can now be studied more thoroughly (see R. M. Lau et al. 2020).

While WR stars are quite rare in typical local IMFs, more top-heavy IMFs which may be naively expected in the early Universe (proposed by, e.g., E. Rasmussen Cueto et al. 2023; C. L. Steinhardt et al. 2023) may produce enough WC stars (if sufficiently carbon-enriched) to fully account for the reddening observed between $z \simeq 12$ and $z \simeq 9$ should dust destruction processes not be prevalent in the reverse shock of the resulting SNe. Quantitatively, the IMF required for the two-photon nebular continuum to dominate in GS-NDG-9422 from A. J. Cameron et al. (2024) would produce a WR star for every $\sim$140 $M_\odot$ of normal stellar population compared to every $\sim$1300 $M_\odot$ in a typical local IMF. Evidence for dust produced via WC binaries, for instance from the $\lambda_{\rm rest} = 2175$ Å carbonaceous signature found at $z = 6.71$ by J. Witstok et al. (2023), would likely point toward a more top-heavy IMF.

By $z = 6.5$ the Universe is approximately 825 Myr old, with 500 Myr of time having passed since the upper-redshift limit of this study at $z = 13$. Should all galaxies in our $6.5 < z < 8.5$ bin be $\sim$500 Myr old, we expect the stellar winds of asymptotic giant branch (AGB) stars to dominate the production of dust. Although these stars are less massive (0.5–8 $M_\odot$), longer-lived ($\gtrsim$100 Myr timescales), and produce less dust than WR stars, they are also more common. In addition, ISM dust grain growth may also be prevalent in this stage of galaxy evolution, although little is known regarding the size, shape, and chemical composition of dust grains at $z = 6.5$ beyond theoretical predictions (e.g., B. S. Hensley & B. T. Draine 2023).

As well as the average reddening, we also observe an increasing scatter in β–$M_\star$ with decreasing redshift. Even though at lower redshift there is more diversity in ages,

[33] https://github.com/flaresimulations/synthesizer

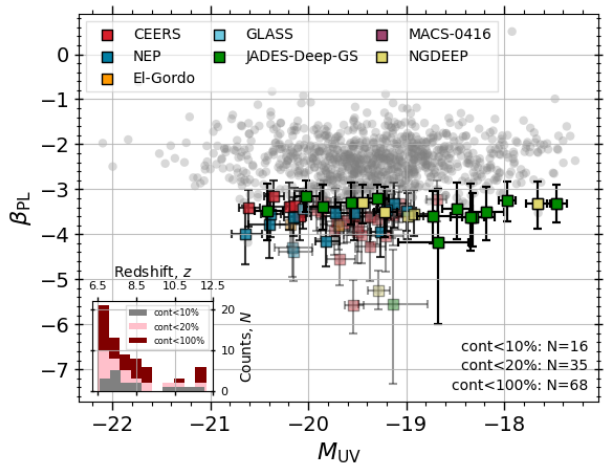

Figure 13. Subsample of 68 ultra-blue $\beta + \sigma_\beta < -2.8$ candidates, with 35 and 35 having less than 20% and 10% contamination likelihood, respectively, plotted as colored points with more solid colors (less transparency). The rest of the EPOCHS-III sample within our redshift range of interest is plotted in black. Redshift distributions of the three subsamples of ultra-blue candidate galaxies are shown in the lower-left plot inset.

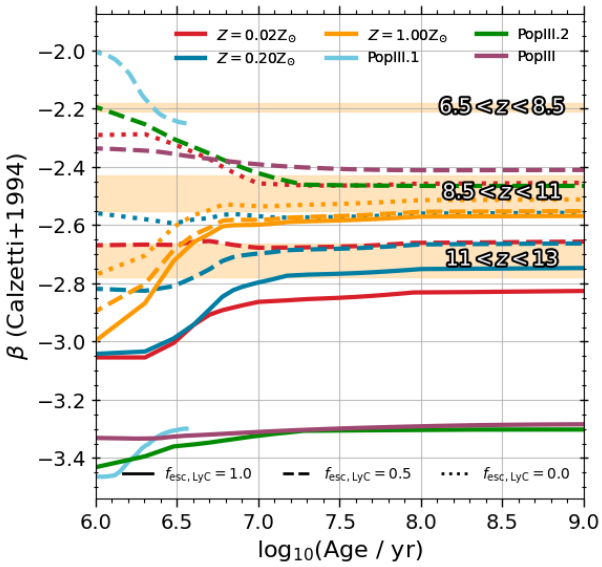

Figure 14. Power-law-measured UV β slopes as a function of galaxy age for the instantaneous burst Yggdrasil Population I, II, and III SEDs (E. Zackrisson et al. 2011) measured in the 10 C94 filters to avoid bias from nebular rest-UV line emission prevalent at young ages. Bias-corrected power-law β constraints for our three redshift bins are highlighted in light orange showing the most notable new $11 < z < 13$ ultra-blue $\langle\beta\rangle$ measurements. The solid ($f_{esc,LyC} = 1.0$), dashed ($f_{esc,LyC} = 0.5$), and dotted ($f_{esc,LyC} = 0.0$) lines show the values with various assumed $f_{esc,LyC}$.

metallicities, and environment at a given mass, R. J. Bouwens et al. (2012) show (in their Figure 18) that the scatter in dust attenuation provides the largest impact on the scatter in β. We conclude, therefore, that the increase in scatter between $z = 13$ and $z = 6.5$ is due to the variety of dust production methods available in these galaxies (from Type II SNe, ISM dust grain growth, or WC/RSG/AGB stars), which are on average older, and may lead to a diversity of dust attenuation laws diverging from the standard D. Calzetti et al. (2000) or SMC/LMC laws adopted in the local Universe.

5.3. A Robust Sample of Blue $\beta < -2.8$ Galaxies

Our fits to β–M_{UV} in Figure 9 show that, on average, the galaxy population is uniformly blue at $z \gtrsim 11.0$, most likely due to the lack of dust at these high redshifts. Much work has been done in the past to investigate galaxies with ultra-blue β slopes with minimal A_{UV} dust extinction, including the possibility of Pop III stars and an increasingly top-heavy IMF (e.g., D. Schaerer 2002, 2003; A. Raiter et al. 2010; E. Zackrisson et al. 2011).

We produce a tiered sample of 68 ultra-blue galaxies with $\beta + \sigma_\beta < -2.8$, 35 of which have Cont($M_{UV}$, β) < 0.2, with 16 galaxies from NGDEEP and JADES-Deep-GS having Cont(M_{UV}, β) < 0.1. We plot this tiered sample in Figure 13 with transparency defined by 1 − Cont(M_{UV}, β). While one might expect that some of the measured colors are extremely blue due to photometric scatter, a simple test finds that only 2.7% of galaxies with mean $\beta = -2.39$ and $\sigma_\beta = 0.45$ (i.e., the median and standard deviation of our EPOCHS-III sample) are expected to scatter to $\beta + \sigma_\beta < -2.8$, as opposed to the observed 6.4%. Splitting this by redshift bin instead yields an expected 1.8%, 4.8%, and 8.5%, compared to the observed 5.2%, 10.1%, and 16.0% in the $6.5 < z < 8.5$, $8.5 < z < 11$, and $11 < z < 13$ redshift bins, respectively. Our simulation results thus strongly suggest that some sources genuinely have extremely blue colors, and that this population does not arise entirely from photometric scatter.

To analyze the possible scenarios that could give rise to these extreme blue average β values, we compare our results to the Pop I, II, and III instantaneous burst SED models produced by the Yggdrasil SPS code (E. Zackrisson et al. 2011). The Pop I and Pop II models are plotted with metallicities $Z_\star = \{0.02, 0.2, 1\}\ Z_\odot$, a Starburst99 single stellar population (SSP) based on Padova-AGB tracks (C. Leitherer et al. 1999; G. A. Vázquez & C. Leitherer 2005), a gas density $n_H = 100\,\mathrm{cm}^{-2}$, and a universal P. Kroupa (2001) IMF in the range 0.1–100 $M_\odot$. The "PopIII" model uses the same P. Kroupa (2001) IMF as the Pop I and Pop II models, although with a rescaled SSP from D. Schaerer (2002). The "PopIII.2" model uses a moderately top-heavy IMF (log-normal with 10 $M_\odot$ characteristic mass, dispersion $\sigma = 1.0$, and 1–500 $M_\odot$ wings) from A. Raiter et al. (2010), while the "PopIII.1" model uses the most top-heavy IMF (50–500 $M_\odot$ with an E. E. Salpeter 1955 IMF slope) from D. Schaerer (2002). All Pop III models assume zero metallicity by definition.

In Figure 14, we calculate β in the 10 C94 filters for a range of ages, 10^6–10^9 yr, and plot against our average β results at $M_{UV} = -19$ given in Table 5 from our best-fitting power law to the β–M_{UV} relation in our three redshift bins. First of all, we conclude that since none of these dust-free models can reproduce our results at $6.5 < z < 8.5$, there must have been dust built up in the majority of these galaxies already at this epoch. We now focus our attention toward our highest-redshift bin, where the bluest and most extreme $\langle\beta\rangle$ are observed. At these redshifts, we cannot rule out the possibility that there are Pop III sources within our sample, and propose two plausible scenarios which could explain our observational results:

1. We are dominated by low-metallicity, $Z_\star < Z_\odot$, stellar populations with moderate to extreme Lyman continuum leakage, $f_{esc,LyC} > 0.5$, in dust-free environments. It has been shown, however, that both the FSPS (C. Conroy et al. 2009;

C. Conroy & J. E. Gunn 2010; N. Byler et al. 2017) and α-enhanced BPASS (C. M. Byrne et al. 2022) models reduce the dependence of β of $f_{\rm esc,LyC}$, and hence allow for lower values of $f_{\rm esc,LyC}$ to coincide with our observations (see F. Cullen et al. 2024, Figure 9).

2. There exists a nonnegligible number of galaxies in the sample with a more top-heavy (potentially Pop III) IMF which either must have $f_{\rm esc,LyC} \simeq 1$, if enshrouded in dust, or moderate $f_{\rm esc,LyC} \gtrsim 0.5$, if dust-free. We note that we have already seen evidence of strong metal lines in spectra at $z > 11$ (e.g., GN-z11), making it unlikely that many of our high-redshift galaxy sample host entirely metal-free Pop III stellar populations. There remains the possibility, however, that Pop III stars contribute a nonnegligible amount to the stellar SED due to the coexistence and incomplete mixing of these with more metal-enriched stars (R. Sarmento et al. 2018, 2019).

Aside from these two scenarios that would explain the blue β mentioned above, there still remains the possibility that our subsample is biased blue by Lyα emission (as much as $\Delta\beta = -0.6$ for $\mathrm{EW}_{\mathrm{Ly}\alpha} = 300$ Å at $z \sim 7$), is dominated by contamination from Balmer break galaxies, or is simply produced as a result of photometric scatter in our wideband photometric NIRCam surveys.

6. Conclusions

In this paper, we have calculated the UV continuum slopes, β, absolute UV magnitudes, $M_{\rm UV}$, and stellar masses, $M_\star$, for 1011 high-redshift galaxies at $6.5 < z < 13$ taken from the EPOCHS v1 sample across 178.9 arcmin^2 of unmasked blank-sky area. The main aims of this study are to both trace the build up of dust from the average β values as well as search for extremely blue $\beta < -3$ in individual galaxies in the EoR. We favor the power-law method to measure β as it is not biased red by the Bayesian prior on β and it better matches 41 cross-matched NIRSpec PRISM-derived $\beta_{\rm spec}$ collated from the DJA. We summarize the main results of this paper below:

1. We quantify the potential impact of rest-frame UV line emission, LAEs, and DLAs on the measured β as a function of redshift in the range $6.5 < z < 13$. Biases can be seen as large as $|\Delta\beta| \simeq 0.1$ for UV line emitters per 10 Å EW, $\Delta\beta = -0.6$ for the strongest LAEs with EW = 300 Å, and $\Delta\beta = 0.5$ for proximate DLAs with $N_{\rm HI} = 10^{23.5}\,\mathrm{cm}^{-2}$. Though some JWST/NIRCam medium-band filters are present in several wide-field surveys, expanding the number of filters used in deep fields can help in reducing these biases, for instance in the JADES Origin Field (PID: 3215).
2. Our β bias simulations show that the faintest galaxies in our sample are biased blue, with maximum $\Delta\beta \simeq -0.55$. This bias is larger for redder galaxies due to the increased selectability of blue objects, and is especially poor ($\Delta\beta \sim -0.3$ even in the brightest sources) for red objects at $6.5 < z < 7.5$ in fields where blue supplementary HST/ACS data are not included and at $7.5 < z < 9.5$ in CEERS and NGDEEP where there is no F090W filter even when including F814W data from HST/ACS.
3. We measure a decreasing trend of β with redshift, $\beta = -1.51 \pm 0.08$–$(0.097 \pm 0.010) \times z$. This is corroborated by our $\beta(M_{\rm UV} = -19)$ decreasing from $\beta(M_{\rm UV} = -19) = -2.19 \pm 0.06$ at $z \simeq 7$ to $\beta(M_{\rm UV} = -19) = -2.73 \pm 0.06$ at $z \simeq 11.6$, implying minimal *average* dust attenuation at the highest redshifts and deviating from the FLARES, DELPHI, SC-SAM GUREFT, and DREaM simulations. Our β–z relation is also discrepant with recent JWST observations by M. W. Topping et al. (2024a), and falls between those by F. Cullen et al. (2024) and G. Roberts-Borsani et al. (2024) due to differing sample $M_{\rm UV}$ distributions and selection procedures.
4. We measure a flatter $d\beta/dM_{\rm UV} = 0.03 \pm 0.02$, leading to an $M_{\rm UV}$-independent β–z relation, and a shallower $d\beta/d\log_{10}(M_\star/M_\odot) = 0.24 \pm 0.01$ at $z \simeq 7$ than seen in previous HST studies (e.g., S. L. Finkelstein et al. 2012; R. Bhatawdekar & C. J. Conselice 2021), revealing a large population of low-mass, faint, red galaxies. These could be DLAs or nebular-dominated galaxies, but if indeed reddened by dust this would imply either early dust production in the stellar winds of AGB or carbon-rich WR (i.e., WC) binaries coupled with reduced dust destruction in subsequent SNe reverse shocks.
5. The observed steepening of $d\beta/d\log_{10}(M_\star/M_\odot)$ toward high redshift implies that dust produced by core-collapse SNe at the earliest times is ejected by SNe-induced outflows and retained by the large gravitational potential wells of high-mass galaxies.
6. We identify 68 $\beta + \sigma_\beta < -2.8$ ultra-blue galaxy candidates that are potential LyC leakers and which may host Pop III or top-heavy IMFs, although comparison to spectroscopy shows the β of individual objects is difficult to accurately constrain.

We have collated one of the largest samples of high-redshift galaxies at $z > 6.5$ and performed a comprehensive analysis of the β biases associated with this sample. While we speculate on the implications of our results regarding the dust content and production channels, we note that many scenarios here are degenerate and indistinguishable with photometric data alone. Our candidate ultra-blue ($\beta + \sigma_\beta < -2.8$) galaxies may provide evidence for Pop III stellar populations and/or significant LyC leakage, although high UV continuum SNR spectra from NIRSpec remain crucial to confirm these theories.

Acknowledgments

We acknowledge support from the ERC Advanced Investigator Grant EPOCHS (grant No. 788113), as well as two studentships from STFC for D.A. and T.H. L.W. acknowledges funding from the Faculty of Science & Engineering at the University of Manchester. L.F. acknowledges financial support from Coordenação de Aperfeiçoamento de Pessoal de Nível Superior - Brazil (CAPES) in the form of a PhD studentship. R.W., S.H.C., and R.A.J. acknowledge support from NASA JWST Interdisciplinary Scientist grant Nos. NAG5 12460, NNX14AN10G, and 80NSSC18K0200 from the Goddard Space Flight Center. C.C. is supported by National Natural Science Foundation of China, grant Nos. 11803044, 11933003, and 12173045. This work is sponsored (in part) by the Chinese Academy of Sciences (CAS), through a grant to the CAS South America Center for Astronomy

(CASSACA). We acknowledge the science research grants from the China Manned Space Project with grant No. CMS-CSST-2021-A05. M.A.M. acknowledges the support of a National Research Council of Canada Plaskett Fellowship, and the Australian Research Council Centre of Excellence for All Sky Astrophysics in 3 Dimensions (ASTRO 3D), through project number CE17010001. M.N. acknowledges INAF-Mainstreams 1.05.01.86.20. C.N.A.W. acknowledges support from the NIRCam Science Team contract to the University of Arizona, NAS 5-02015. E.Z. acknowledges project grant No. 2022-03804 from the Swedish Research Council (Vetenskapsrådet) and has also benefited from a sabbatical at the Swedish Collegium for Advanced Study.

This work is based on observations made with the NASA/ESA Hubble Space Telescope (HST) and NASA/ESA/CSA JWST obtained from the Mikulski Archive for Space Telescopes (MAST) at the Space Telescope Science Institute (STScI), which is operated by the Association of Universities for Research in Astronomy, Inc., under NASA contract NAS 5-03127 for JWST, and NAS 5–26555 for HST. The PEARLS observations used in this work are associated with JWST programs 1176 and 2738. In addition, public data sets from JWST programs 1180, 1210, 1895, 1963 (JADES), 1324 (GLASS), 1345 (CEERS), and 2079 (NGDEEP) are also used within the work presented. Some of the data products presented herein were retrieved from the Dawn JWST Archive (DJA). DJA is an initiative of the Cosmic Dawn Center, which is funded by the Danish National Research Foundation under grant No. 140. The authors thank all involved in the construction and operations of the telescope as well as those who designed and executed these observations; their number are too large to list here, and without each of their continued efforts such work would not be possible. The authors also thank Adam Carnall for their prompt help with `Bagpipes` via email, as well as helpful discussions with Rebecca Bowler, Fergus Cullen, and Albert Zijlstra, which significantly improved the discussion of results. This work is dedicated to the memory of our dedicated colleague and coauthor, Mario Nonino, who sadly passed during the completion of this work.

The authors thank Anthony Holloway and Sotirios Sanidas for providing their expertise in high-performance computing and other IT support throughout this work. This work makes use of `astropy` (Astropy Collaboration et al. 2013, 2018, 2022), `matplotlib` (J. D. Hunter 2007), `reproject`, `DrizzlePac` (S. L. Hoffmann et al. 2021), `SciPy` (P. Virtanen et al. 2020), `photutils` (L. Bradley et al. 2022), and `galfind`. v1 of the `galfind` code is expected to be released to the public within the next year.

Data Availability

The data presented in this article were obtained from the Mikulski Archive for Space Telescopes (MAST) at the Space Telescope Science Institute (STScI). The specific observations analyzed are the same as from the EPOCHS-II UVLF, which can be accessed at DOI:10.17909/5h64-g193. A machine-readable EPOCHS catalog including a Boolean "EPOCHS-III" selection column as well as the β measurements used in this work is made available in Table 2 of C. J. Conselice et al. (2025).

Appendix A
UV Continuum Slope Biases

A.1. The Impact of Strong Rest-frame UV Emission Lines

It is well known that modeling the rest-frame UV as a power law is not strictly correct due to the presence of the 2175 Å dust bump (T. P. Stecher & B. Donn 1965; B. S. Hensley & B. T. Draine 2023) from carbonaceous dust grains (see J. Witstok et al. 2023 for more details), as well as rest-frame UV emission lines and nebular continuum emission in SFGs. In this section, we simulate the impact of rest-UV emission lines on β. We produce 10,000 mock power-law SEDs evenly spaced in redshift between $6.5 < z < 13$ at fixed intrinsic $\beta_{\rm int} = -2.5$, with photometric errors calculated assuming the galaxy has $m_{\rm UV} = 26$, with each filter having a 5σ depth of $m_{\rm AB} = 30$. Doppler-broadened rest-frame UV emission lines with fixed Doppler parameter, $b = 150\,{\rm km\,s^{-1}}$, and rest-frame EWs 1–25 Å were individually added to the SEDs before calculating bandpass-averaged fluxes in the standard eight PEARLS JWST/NIRCam bands. From these photometric fluxes, we then measured β using our preferred power-law method at the fixed input redshift with the bias in β measured as $\Delta\beta_{\rm line} = \beta_{\rm line} - \beta_{\rm int}$. We did this for the rest-UV emission lines C IV λ1549, He II λ1640, O III] λ1665, and C III] λ1909, which contaminate the F115W, F150W, and F200W SW NIRCam wideband filters. The resulting bias as a function of input redshift is shown in Figure 15 for ${\rm EW_{rest}} = 10$ Å. We note that this simulation is independent of β, $m_{\rm UV}$, and Doppler b, and that the biases scale linearly with rest-frame EW such that

$$\Delta\beta({\rm EW_{rest}}) = {\rm EW_{rest}}\frac{\Delta\beta({\rm EW_{rest}} = 10\ \text{Å})}{10}. \tag{A1}$$

Previous observations of SFGs from the ground have found rest-UV emission-line EWs as high as 27 Å for the semi-forbidden C III] λ1909 (J. R. Rigby et al. 2015; D. P. Stark et al. 2017) and ∼8–10 Å for O III] λ1665 and He II λ1640 (T. Nanayakkara et al. 2019; A. Saxena et al. 2020) at $z \sim 4$. Strong He II λ1640 emitters are often associated with AGN when C IV λ1549 emission is also present (e.g., A. Feltre et al. 2016), although it has been shown that BPASS SPS models can explain the observed ratios through star formation alone (L. Xiao et al. 2018). In addition, A. E. Jaskot & S. Ravindranath (2016) find that the BPASS models show C III] λ1909 is the strongest line bluewards of 2700 Å, which becomes more prominent in young, metal-poor systems with high ionization parameters.

More recently, several authors have reported strong rest-frame UV emission lines at $z > 6$ in NIRSpec spectroscopic data. At $z \simeq 8$–8.5, M. Tang et al. (2023) find C III] λ1909 EWs as large as 12–16 Å, with T. Y.-Y. Hsiao et al. (2024) and S. Fujimoto et al. (2023) finding highly ionized bubbles at $z = 8.5$–13 and $z = 10.17$ in the Ultradeep NIRSpec and NIRCam Observations before the Epoch of Reionization survey (or UNCOVER; PIs: I. Labbe & R. Bezanson; PID: 2561; R. Bezanson et al. 2024) and the MACS-0647 lensing cluster. Recent JWST observations have also detected strong C IV λ1549 due to the presence of hard ionizing fields at early times, with M. W. Topping et al. (2024b) observing a rest-frame C IV λ1549 EW of 34 Å in a gravitationally lensed $z = 6.11$ object behind the RXCJ2248 lensing cluster (see also R. Mainali et al. 2017; K. B. Schmidt et al. 2017).

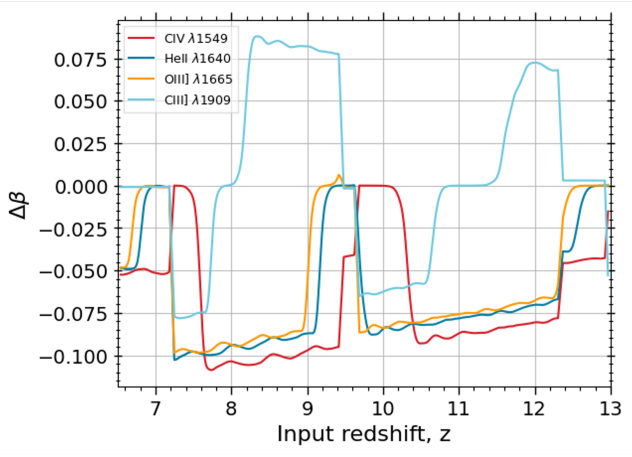

Figure 15. β bias from rest-frame UV line emission. Shown are results assuming rest-frame EWs of 10 Å for C IV λ1549, He II λ1640, O III] λ1665, and C III] λ1909 applied to a set of 10,000 power-law SEDs with $\beta_{\rm int} = -2.5$ evenly spaced across $6.5 < z < 13$. These biases scale linearly with emission-line EW and are true under the assumption that $\epsilon = 0$, or that the emission line does not impact the photometrically derived redshift.

M. Castellano et al. (2024) also find the strongest EoR C IV λ1549 EW of 45.8 ± 1.2 Å in the spectroscopically confirmed GHZ2/GLASS-z12 object at $z = 12.34$; this source was initially detected in GLASS NIRCam photometry by R. P. Naidu et al. (2022) and M. Castellano et al. (2022) and is included in our EPOCHS-III sample (see EPOCHS-I, Figures 2 and 3) and provides evidence for UV line emission bias in our sample. Additionally, C. Charbonnel et al. (2023), A. J. Cameron et al. (2023), and P. Senchyna et al. (2024) also observe strong nitrogen abundance in the well-studied GN-z11 (P. A. Oesch et al. 2016; A. J. Bunker et al. 2024).

While we cannot determine rest-frame UV line EWs in our sample using broadband photometry alone, these studies give us an idea of the expected β biases and ionization conditions in reionization era galaxies. The rest-UV line EWs and intrinsic β slopes measured in the C94 filters for the blue R. L. Larson et al. (2023) templates used in this work are given in Table 7. Due to the strong rest-frame UV emission lines in these templates, there is a redshift- and filter-set-dependent bias between the power-law fit to the photometry and from the SED in the C94 filters. Even when accounting for the emission lines, we find that using the C94 filters biases β red by up to 0.1 compared to our power-law method. We attribute this to the increased wavelength coverage of the C94 filters toward the nebular continuum two-photon turnover in the youngest R. L. Larson et al. (2023) templates quantified by $\Delta\beta_{\rm neb} = \beta_{\rm C94}(f_{\rm esc,LyC} = 0) - \beta_{\rm C94}(f_{\rm esc,LyC} = 1)$.

Table 7
Rest-frame EWs of the Most Prominent UV Emission Lines from the Blue R. L. Larson et al. (2023) Templates Used in Our SED-fitting Procedure (Set 4) for Ages Ranging 1–10 Myr

$\log_{10}$(Template Age/yr)	6.0	6.5	7.0
$\rm EW_{rest}(Ly\alpha)/Å$	0.0	0.0	0.0
$\rm EW_{rest}$(C IV λ1549)/Å	5.6	2.0	0.5
$\rm EW_{rest}$(He II λ1640)/Å	0.3	1.0	1.1
$\rm EW_{rest}$(O III] λ1665)/Å	5.2	3.6	1.0
$\rm EW_{rest}$(C III] λ1909)/Å	28.7	21.5	7.3
$\beta_{\rm C94}(f_{\rm esc,LyC} = 0)$	−2.36	−2.32	−2.52
$\beta_{\rm C94}(f_{\rm esc,LyC} = 1)$	−3.11	−2.82	−2.77
$\Delta\beta_{\rm neb}$	0.75	0.50	0.25

Note. There is no Lyα present in these templates, and C III] λ1909 is consistently the strongest of these lines, which appears especially potent at the youngest ages. Intrinsic β slopes calculated in the 10 C94 filters for $f_{\rm esc,LyC} = \{0, 1\}$ (i.e., including and excluding CLOUDY nebular emission) are also given. For a decreasing galaxy age, the reddening of the underlying continuum by nebular emission ($\Delta\beta_{\rm neb}$) increases in addition to the stellar continuum becoming bluer.

A.2. Proximate Damped Lyα Systems and the Lyα Damping Wing

When traversing the IGM in the EoR, Lyα photons from the source galaxy are absorbed by neutral hydrogen along the line of sight to the observer. This, combined with attenuation from the Lyα forest bluewards of 1216 Å, produces the characteristic red-skewed Lyα damping wing. The most widely used prescription of the Lyα damping wing is presented in J. Miralda-Escudé (1998). This model assumes that the IGM has a constant (volume-averaged) neutral hydrogen fraction, $x_{\rm HI}$, between the source redshift, $z_{\rm gal}$, and that the end of reionization occurs at $z_{\rm Re,end}$, and neglects the patchy nature of reionization. The Lyα optical depth through the neutral IGM, $\tau_{\rm IGM,Ly\alpha}(\lambda_{\rm obs}, z_{\rm gal}, x_{\rm HI}, R_{\rm b}, \tau_{\rm GP}, z_{\rm Re,end})$,[34] is also given as a function of $R_{\rm b}$, the radius of the surrounding ionized H II bubble, and $\tau_{\rm GP}$, the cosmology-dependent J. E. Gunn & B. A. Peterson (1965) optical depth. Using NIRSpec data from the first year of JWST operation, large ionized bubbles with $R_{\rm b} \gtrsim 1$ cMpc have been inferred from these Lyα damping wings at high redshift (H. Umeda et al. 2024; L. Whitler et al. 2024; J. Witstok et al. 2024), with a large implied contribution from faint galaxies with $M_{\rm UV} > -16$ in large-scale galaxy overdensities (T.-Y. Lu et al. 2024). Recent comparisons to theorized damping wing profiles assuming a more realistic patchy reionization process (e.g., L. C. Keating et al. 2024) suggest that the presence of small amounts of residual H I as low as $x_{\rm HI} \sim 10^{-5}$ (M. McQuinn 2016) within these ionized bubbles and strong Lyα emission (seen observationally by A. Saxena et al. 2023a) may instead be responsible for these large $R_{\rm b}$ values. Due to the uncertainties in modeling this damping wing, we choose not to quantify any associated β biases. We do note, however, that this is likely to bias our β slightly redwards due to the softening of the Lyα break, leading to minor redshift overestimations when SED fitting using templates that do not include this dampening.

In addition, DLA systems with high column densities of neutral hydrogen $N_{\rm HI} > 2 \times 10^{20}\,{\rm cm}^{-2}$ (K. Lanzetta 2000), arising from dense gas clouds in the vicinity of starburst galaxies, have been observed at high redshift both in quasar (T. Totani et al. 2006) and galaxy spectra (K. E. Heintz et al. 2024). These systems act to soften the Lyman break and increase photometric Lyman–Balmer break degeneracy, decreasing photo-z accuracy. The UV β slopes of these systems are often biased red due to the reduction in flux associated with the first band redwards of 1250 Å. In addition, photo-z's are often overestimated when SED-fitting codes confuse the reduction in flux in the first band redwards of the Lyα break with the break itself. At certain filter-set-dependent redshifts, $\Delta\beta_{\rm DLA}$ becomes smaller with increasing $N_{\rm HI}$ when

[34] It is noteworthy that $z_{\rm Re,end}$ has a minor impact on calculated values of $\tau_{\rm IGM,Ly\alpha}$ in the J. Miralda-Escudé (1998) model.

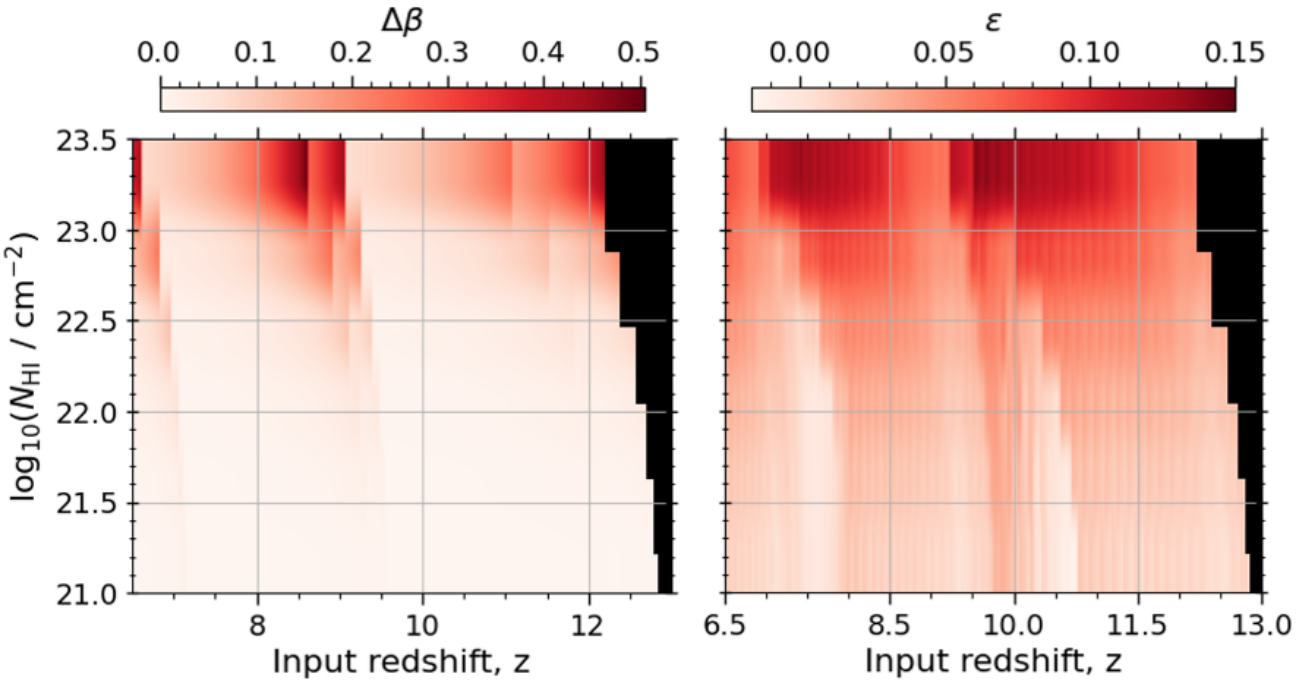

Figure 16. Left: power-law-measured β bias as a function of input redshift and DLA H I column density, $N_{\rm HI}$. Biases as large as 0.5 redwards are observed in DLAs with the largest column densities, $N_{\rm HI} = 10^{23.5}$ cm^{-2}, at redshifts $z \sim \{6.5, 9, 12\}$. Right: DLA β bias as a function of photo-z error, ϵ, as defined in Equation (4), with red values showing overestimated photo-z, reaching a maximum of 15%. The black region toward the highest redshifts shows the region that would fail the observed $z < 13$ cut due to the photo-z overestimation.

this band is no longer included in the rest-frame UV range used to calculate β. We do not attempt to identify DLAs in our selection procedure, but instead simulate the impact on simple power-law SED models.

We produce 10,000 mock power-law SEDs with $\beta = -2.5$ and $m_{\rm UV} = 26$, with redshifts evenly spaced in the interval $6.5 < z < 13$ assuming an A. K. Inoue et al. (2014) IGM attenuation post-reionization. These SEDs are then propagated through the ISM with fixed Lyα velocity offset $\Delta v_{\rm Ly\alpha} = 0$, Doppler $b = 150$ km s^{-1}, and a range of neutral hydrogen column densities $\log_{10}(N_{\rm HI}/{\rm cm}^{-2}) = \{21, 21.5, 22, 22.5, 23, 23.5\}$. The DLA optical depth is calculated as

$$\tau_{\rm DLA}(\lambda_{\rm rest}) = CaN_{\rm HI}H(a, x(\lambda_{\rm rest} + \Delta v_{\rm Ly\alpha}, b)), \quad \text{(A2)}$$

where C and a are the Lyα photon absorption constant and damping parameters, and $H(a, x(\lambda, b))$ is the Voijt–Hjerting approximation to the Voigt profile (T. Tepper-García 2006), which is dependent on the Doppler parameter, $b = \sqrt{2k_B T_{\rm HI}/m_p}$, via

$$x(\lambda, b) = \frac{c(\lambda - \lambda_{\rm Ly\alpha})}{b\lambda_{\rm Ly\alpha}}. \quad \text{(A3)}$$

This Voigt profile is insensitive to the choice of b for DLAs with large $N_{\rm HI}$, where the Lorentzian wings from the naturally broadened Lyα dominate.

We then calculate bandpass-averaged fluxes from the standard eight-band PEARLS JWST/NIRCam filter set and rerun through our `EAZY-py` photo-z fitting procedure before recalculating β using the photometric power-law method at the derived photo-z to calculate the bias $\Delta\beta_{\rm DLA} = \beta_{\rm DLA} - \beta_{\rm int}$. It is noteworthy that in this process we include only photometric bands at $\lambda_{\rm rest} < 3000$ Å to avoid the non-power-law nature of the Balmer jump at 3646 Å, Balmer break at ∼4000 Å, and strong rest-optical nebular emission lines including [O III]/Hβ.

We plot $\Delta\beta_{\rm DLA}$ as a function of $N_{\rm HI}$ in Figure 16, finding $\Delta\beta_{\rm DLA} = 0.5$ even in the most extreme DLA scenarios with $N_{\rm HI} = 10^{23.5}$ cm^{-2}, meaning that our sample may well be biased red by DLAs in some specific cases. This upper $N_{\rm HI}$ limit is set by the required H I column density should the A. J. Cameron et al. (2024) objects be contrived DLAs as opposed to nebular-dominated systems. As of now, the highest DLA column densities observed in the early Universe ($z > 10$) are approximately $\log_{10}(N_{\rm HI}/{\rm cm}^{-2}) = 22$–$22.5$ (F. D'Eugenio et al. 2024; K. E. Heintz et al. 2024; H. Umeda et al. 2024), and large spectroscopic studies have recently been performed to assess the abundance of these DLA systems (K. E. Heintz et al. 2025). Much is still to be determined about these systems, however, including whether large neutral gas reservoirs can form in the presence of strong winds, producing larger Lyα velocity offsets $\Delta v_{\rm Ly\alpha} \gtrsim +400$ km s^{-1}, as well as how common DLAs are at high redshift where gas masses are expected to be larger. We conclude that it is likely that some of our sources are biased red, however the extent of this in our photometric sample is largely unknown.

A.3. The Impact of Lyα Emission

Although LAEs are known to exist at low redshift, during the EoR the observed Lyα rest-frame EWs are expected to reduce due to absorption by neutral hydrogen along the line of sight (i.e., the Lyα damping wing). Although the exact nature of this damping wing, and indeed the size of ionized bubbles in the early Universe, is largely unknown, several studies have observed high-EW Lyα systems at $z > 6$ in recent spectroscopic JWST data (e.g., A. Saxena et al. 2023a, 2023b; M. Nakane et al. 2024; J. Witstok et al. 2024; Z. Chen et al. 2024;

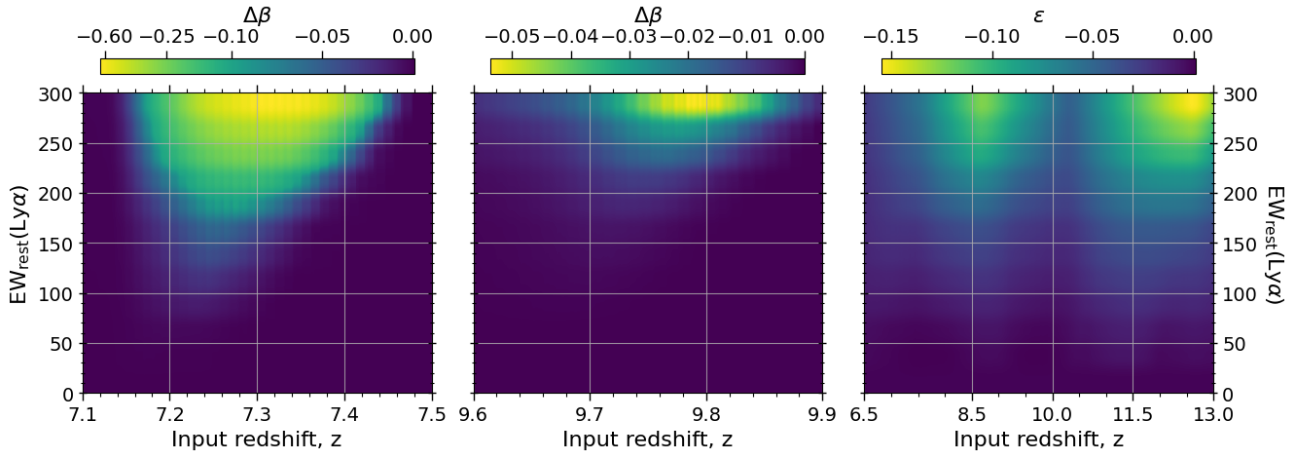

Figure 17. Left and center: β bias as a function of rest-frame Lyα EW at input redshift $z \simeq 7.3$ (left panel) and $z \simeq 9.8$ (center panel). It is worth noting the color bar scaling in these two panels, where the bias at $z \simeq 7.3$ is far greater than at $z \simeq 9.8$, even before accounting for the reduction in observed EW due to absorption in the neutral IGM along the line of sight. Right: photo-z error as a function of input redshift and Lyα EW. We see that the photo-z is underestimated by as much as $\epsilon = -0.15$ (i.e., 15%) in the case of strong Lyα emission at $z \simeq \{8.5, 12.5\}$.

L. Napolitano et al. 2024). In this section, we study the impact of these LAEs on measured β slopes in JWST/NIRCam wideband studies. Even though both the number density (Z. Haiman 2002; S. Malhotra & J. E. Rhoads 2006) and EW evolution (M. Tang et al. 2024) of these EoR LAEs has already been studied, we do not quantify the average bias in our sample as the selection efficiency of LAEs by our specific EPOCHS criteria in Section 2.5 is not well known.

The impact of Lyα emission on photometrically measured β slopes has in fact already been studied by A. B. Rogers et al. (2013), who found a blue bias that increases with EW. Their work analyses the bias in β measured from a power-law fit to HST/WFC3-IR F105W (Y_{105}), F125W (J_{125}), F140W (J_{140}), and F160W (H_{160}) photometry at $6.5 < z < 7.5$, finding $-0.8 \lesssim \Delta\beta_{\mathrm{Ly}\alpha} \lesssim -0.5$ at $z \simeq 7$ for rest-frame EWs of 50–100 Å. In this section, we analyze the bias in β measured using JWST/NIRCam wide bands, which may be systematically different from the β measured using $Y_{105}J_{125}J_{140}H_{160}$ HST/WFC3-IR photometry.

We calculate the impact of Lyα emission on the measured β slopes using a similar method to that used to calculate the DLA bias in Appendix A.2. Ten thousand mock power-law SED templates are created with fixed $\beta = -2.5$, $m_{\mathrm{UV}} = 26$ at redshifts $6.5 < z < 13$ for each rest-frame Lyα EW = {5, 10, 20, 30, 40, 50, 75, 100, 150, 200, 300} Å, including Lyα forest IGM attenuation following the A. K. Inoue et al. (2014) prescription, with the upper EW limit set by the largest observable values in A. Saxena et al. (2023a). Bandpass-averaged fluxes are generated for the standard eight JWST/NIRCam filters used in PEARLS, with errors produced assuming a 5σ depth of $m_{\mathrm{AB}} = 30$, and the photometry is run through `EAZY-py` to determine photo-z's. β is then calculated by the power-law method using the rest-frame UV filters determined by the `EAZY-py` photo-z and compared to the intrinsic $\beta = -2.5$ to determine $\Delta\beta_{\mathrm{Ly}\alpha}$, with results shown in Figure 17.

In order to account for the increased flux in the first redwards band of the Lyα break due to this Lyα emission, SED-fitting procedures with underestimated Lyα emission typically underestimate photo-z's (right panel of Figure 17). This introduces the band containing Lyα into the rest-frame UV, and hence biases β blue. As can be seen from Figure 17, there are two redshift ranges of interest (left and central panels) where Lyα emission may produce significant $\Delta\beta_{\mathrm{Ly}\alpha} \simeq -0.6$. At $z = 7.3$, the photo-z underestimation induced by the Lyα emission causes the F090W filter to be incorrectly identified as the dropout filter, with the highly elevated F115W flux density now strongly biasing β blue. The scenario is similar at $z = 9.8$ instead with the F115W and F150W filters, although the effect is a lot weaker than at $z = 7.3$ due to the gap between the F115W and F150W filters not present between F090W and F115W, resulting in weaker Lyα throughput and hence little impact on $\Delta\beta$. We note that this estimate of bias is likely an upper limit due to the additional redshift constraints provided by photometric data at $\lambda_{\mathrm{rest}} > 3000$ Å.

The bias methodology mentioned above falls short of a complete implementation of Lyα due to our neglect of Doppler broadening due to H I velocity dispersion, $\sigma_{\mathrm{Ly}\alpha}$, galactic dynamics/outflows shifting the major Lyα peak by $\Delta v_{\mathrm{Ly}\alpha}$, or doubly or triply peaked emission. The profiles of LAEs are explored in more detail using simulations (J. Blaizot et al. 2023), however this is not expected to have a major impact on our bias simulation results. We also do not consider the impact of the Lyα damping wing, the shape of which is not well known due to the unknown volume-averaged neutral fraction of H I as a function of redshift, $\langle x_{\mathrm{HI}}(z) \rangle$, and the patchy reionization process. A further discussion of the Lyα damping wing is presented in Appendix A.2.

Appendix B
The Impact of Little Red Dots

Initial JWST images have uncovered a large sample of LRDs that have been cataloged from photometric (e.g., I. Labbe et al. 2025; V. Kokorev et al. 2024) and spectroscopic (e.g., J. Matthee et al. 2024; D. D. Kocevski et al. 2024) data, some of which have been confirmed to be partially dust-obscured AGN via their broadened Hα lines. We identify 34 LRDs when applying the "red2" color selection criteria, compactness criterion, and SNR requirements from V. Kokorev et al. (2024) to our EPOCHS-III sample, representing the same subsample as in EPOCHS-IV. The locations of these systems in

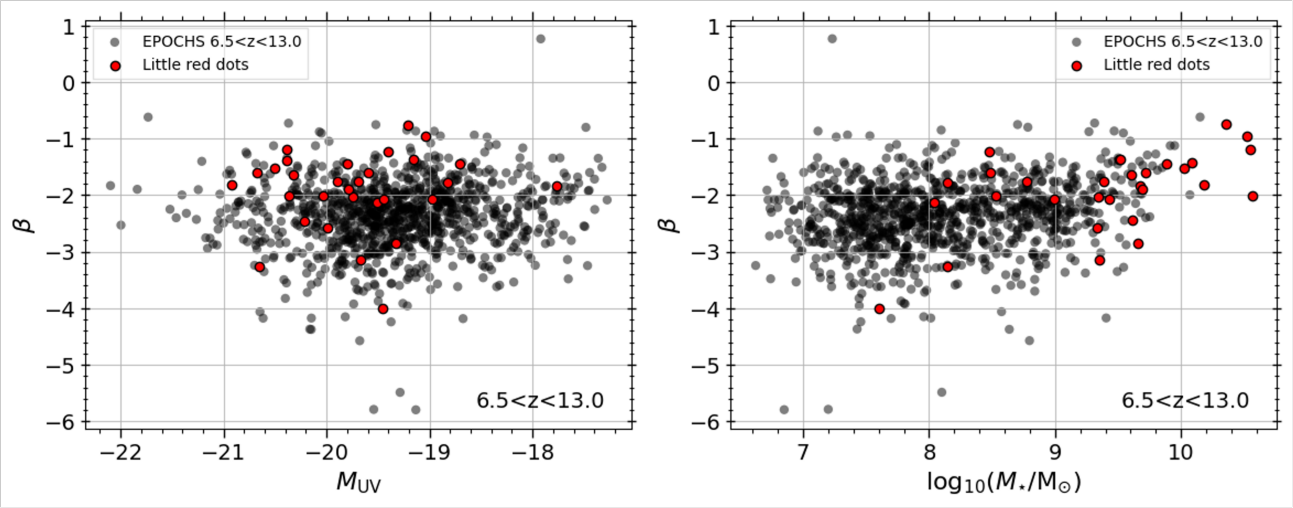

Figure 18. The locations of the 34 LRDs identified in our EPOCHS-III sample using the V. Kokorev et al. (2024) selection criteria. The majority host high observed stellar masses, many of which are likely overestimated, and red rest-frame UV colors, although we note the large scatter in the β distribution of these sources.

the (β, $M_{\rm UV}$) and (β, $M_\star$) parameter spaces are plotted in Figure 18.

These LRDs in general fall within the lowest-redshift $6.5 < z < 8.5$ bin and are mainly intermediate to bright in the rest-frame UV compared with the rest of our EPOCHS-III sample. They are also known to exhibit high stellar masses due to the confusion of the red AGN SED component with an aged stellar population. The β slopes of these LRDs exhibit a wide range of values, but on average are redder than the general SFG population, most likely due to dust production in enriched quasar-driven winds (e.g., R. Valiante et al. 2014; A. Sarangi et al. 2019). We recompute our β–$M_\star$ fit excluding these sources, finding a $\Delta d\beta/d\log_{10}(M_\star/M_\odot) = -0.03$ with 1.5σ significance. Limiting the fit to $M_\star > 10^8 M_\odot$, where all but one of the LRDs are located, produces consistent fitting results. This minor difference is likely due to the small relative sample size compared to our full EPOCHS-III sample (34/1011).

Appendix C
NIRSpec PRISM Cross-matches from the DJA

A total of 24 of the 41 spectroscopically confirmed galaxies in our sample have been found by previous studies (P. Arrabal Haro et al. 2023a; A. J. Bunker et al. 2024; E. Curtis-Lake et al. 2023; K. N. Hainline et al. 2024; K. E. Heintz et al. 2023a, 2024; K. Nakajima et al. 2023; M. Tang et al. 2023; R. L. Sanders et al. 2024), with three found in photometric surveys by C. T. Donnan et al. (2023) and K. N. Hainline et al. (2024). We provide results of these cross-matches in Table 8, where we calculate β both from the NIRSpec PRISM data as well as the NIRCam photometry using the two techniques discussed in this work. The spectroscopic β are measured in the C94 filters and the $1250 < \lambda_{\rm rest}/\text{Å} < 3000$ wavelength range, showing the wavelength dependence of these β measurements, especially in cases of low UV continuum SNR.

Table 8
Spectroscopically Confirmed Galaxies from a Cross-match of Our EPOCHS-III Sample with the DJA

PID	R.A.	Decl.	z_{spec}	β_{spec} (C94)	β_{spec} (1250–3000 Å)	SNR_{UV}	z_{phot}	$\beta_{phot,PL}$	$\beta_{phot,SED}$	References
1180	53.155144	−27.760742	6.3139	-2.26 ± 0.03	-2.27 ± 0.08	9.51	$6.52^{+0.05}_{-0.07}$	$-2.53^{+0.34}_{-0.32}$	$-2.44^{+0.07}_{-0.05}$	⋯
1180	53.127316	−27.788040	6.3845	-3.00 ± 0.05	-2.58 ± 0.16	3.81	$6.57^{+0.04}_{-0.07}$	$-2.62^{+0.35}_{-0.33}$	$-2.52^{+0.05}_{-0.04}$	⋯
1180	53.137429	−27.765207	6.6223	-2.30 ± 0.04	-2.40 ± 0.15	3.53	$6.59^{+0.03}_{-0.06}$	$-2.32^{+0.30}_{-0.34}$	$-2.46^{+0.09}_{-0.04}$	⋯
1180	53.169516	−27.753317	6.6284	-2.53 ± 0.07	-2.68 ± 0.15	4.66	$6.60^{+0.02}_{-0.02}$	$-2.58^{+0.32}_{-0.32}$	$-2.27^{+0.10}_{-0.09}$	⋯
1180	53.118187	−27.793008	6.7895	-1.96 ± 0.06	-2.38 ± 0.18	3.12	$6.89^{+0.03}_{-0.04}$	$-2.31^{+0.32}_{-0.32}$	$-2.13^{+0.12}_{-0.16}$	⋯
1180	53.138054	−27.781863	7.1391	-2.66 ± 0.06	-2.24 ± 0.25	2.12	$7.40^{+0.05}_{-0.24}$	$-2.73^{+0.48}_{-0.51}$	$-2.40^{+0.10}_{-0.06}$	⋯
1180	53.161709	−27.785391	7.2349	-1.45 ± 0.04	-1.96 ± 0.13	4.05	$7.45^{+0.07}_{-0.11}$	$-2.27^{+0.52}_{-0.48}$	$-1.73^{+0.14}_{-0.14}$	⋯
1180	53.164824	−27.788258	7.2406	-1.87 ± 0.06	-1.86 ± 0.13	3.47	$7.39^{+0.09}_{-0.08}$	$-2.31^{+0.50}_{-0.48}$	$-1.94^{+0.12}_{-0.11}$	⋯
1210	53.162377	−27.803300	6.2942	1.88 ± 0.25	-2.27 ± 0.88	0.88	$6.51^{+0.04}_{-0.28}$	$-1.92^{+0.46}_{-0.40}$	$-2.32^{+0.07}_{-0.07}$	(4)
1210	53.175819	−27.774465	6.3351	-1.70 ± 0.03	-1.66 ± 0.10	8.22	$6.58^{+0.04}_{-0.11}$	$-2.08^{+0.32}_{-0.28}$	$-2.37^{+0.07}_{-0.05}$	(4)
1210	53.169041	−27.778842	6.6322	-2.68 ± 0.02	-2.59 ± 0.06	13.86	$6.59^{+0.03}_{-0.02}$	$-2.70^{+0.34}_{-0.36}$	$-2.45^{+0.06}_{-0.04}$	(4)
1210	53.151385	−27.819159	6.7074	-2.03 ± 0.05	-1.87 ± 0.17	4.58	$6.63^{+0.04}_{-0.04}$	$-2.17^{+0.28}_{-0.34}$	$-2.39^{+0.15}_{-0.07}$	(4)
1210	53.155794	−27.815199	6.7186	-2.33 ± 0.05	-2.30 ± 0.13	6.18	$6.65^{+0.03}_{-0.03}$	$-2.50^{+0.33}_{-0.33}$	$-2.30^{+0.08}_{-0.12}$	(4)
1210	53.152839	−27.801940	7.2621	-2.26 ± 0.03	-2.35 ± 0.10	5.59	$7.56^{+0.11}_{-0.29}$	$-2.36^{+0.49}_{-0.49}$	$-2.48^{+0.04}_{-0.03}$	(4)
1210	53.155083	−27.801769	7.2697	-2.31 ± 0.02	-2.34 ± 0.04	17.63	$7.69^{+0.14}_{-0.39}$	$-2.42^{+0.51}_{-0.49}$	$-2.48^{+0.03}_{-0.03}$	(4)
1210	53.156825	−27.767159	7.9807	-2.17 ± 0.02	-2.21 ± 0.06	10.22	$7.95^{+0.14}_{-0.08}$	$-2.71^{+0.53}_{-0.50}$	$-2.15^{+0.13}_{-0.22}$	(4)
1210	53.164468	−27.802181	8.4790	-2.08 ± 0.07	-1.93 ± 0.15	3.15	$8.89^{+0.07}_{-0.20}$	$-2.10^{+0.51}_{-0.53}$	$-2.29^{+0.13}_{-0.13}$	(4), (5)
1210	53.167357	−27.807502	9.6886	-2.71 ± 0.03	-2.75 ± 0.07	7.19	$9.44^{+0.72}_{-0.04}$	$-2.23^{+0.30}_{-0.32}$	$-2.36^{+0.10}_{-0.13}$	⋯
1210	53.164763	−27.774625	11.5922	-2.48 ± 0.03	-2.52 ± 0.06	8.25	$11.94^{+0.19}_{-0.21}$	$-1.92^{+0.27}_{-0.29}$	$-2.40^{+0.10}_{-0.11}$	(3), (4), (5)
1345	214.731462	52.736427	5.3535	-1.73 ± 0.16	-3.70 ± 0.96	0.69	$7.08^{+0.23}_{-1.16}$	$-2.72^{+0.42}_{-0.48}$	$-2.37^{+0.11}_{-0.15}$	⋯
1345	214.806478	52.878827	6.1086	-2.25 ± 0.04	-2.08 ± 0.12	6.36	$6.51^{+0.04}_{-0.30}$	$-2.06^{+0.33}_{-0.33}$	$-2.06^{+0.11}_{-0.10}$	(8)
1345	214.832181	52.885089	6.6203	-2.30 ± 0.06	-2.60 ± 0.23	2.42	$6.61^{+0.04}_{-0.17}$	$-1.58^{+0.35}_{-0.37}$	$-2.13^{+0.15}_{-0.19}$	(8)
1345	215.128019	52.984951	6.6815	-3.74 ± 0.20	-2.39 ± 0.28	6.40	$6.69^{+0.02}_{-0.03}$	$-2.34^{+0.33}_{-0.35}$	$-1.64^{+0.06}_{-0.07}$	⋯
1345	214.789828	52.730794	6.7370	-2.25 ± 0.04	-2.19 ± 0.09	7.17	$6.67^{+0.03}_{-0.04}$	$-2.67^{+0.35}_{-0.33}$	$-2.39^{+0.05}_{-0.05}$	(8)
1345	214.948681	52.853273	6.7501	0.56 ± 0.30	-1.00 ± 0.55	1.32	$6.77^{+0.03}_{-0.04}$	$-2.18^{+0.28}_{-0.32}$	$-2.41^{+0.09}_{-0.05}$	⋯
1345	215.001120	53.011273	7.1028	-2.17 ± 0.04	-2.44 ± 0.16	3.33	$7.12^{+0.23}_{-0.06}$	$-2.67^{+0.35}_{-0.38}$	$-2.42^{+0.12}_{-0.07}$	(2), (8), (10)
1345	214.859185	52.853595	7.1135	-1.38 ± 0.05	-2.23 ± 0.15	4.08	$7.03^{+0.33}_{-0.03}$	$-2.34^{+0.31}_{-0.32}$	$-2.43^{+0.10}_{-0.06}$	(8)
1345	214.813057	52.834241	7.1785	-2.54 ± 0.05	-2.48 ± 0.14	3.98	$7.37^{+0.08}_{-0.19}$	$-3.11^{+0.49}_{-0.51}$	$-2.46^{+0.06}_{-0.05}$	(8), (10)
1345	214.812062	52.746747	7.4757	-2.74 ± 0.04	-2.43 ± 0.12	4.34	$7.38^{+0.06}_{-0.24}$	$-2.38^{+0.52}_{-0.48}$	$-2.32^{+0.14}_{-0.12}$	(8)
1345	214.806079	52.750868	7.6487	-2.16 ± 0.05	-2.15 ± 0.14	3.86	$8.20^{+0.15}_{-0.38}$	$-2.70^{+0.54}_{-0.47}$	$-2.40^{+0.06}_{-0.05}$	(6)
1345	214.882999	52.840419	7.8314	-1.55 ± 0.04	-1.66 ± 0.12	4.34	$8.06^{+0.12}_{-0.12}$	$-2.54^{+0.48}_{-0.52}$	$-2.29^{+0.11}_{-0.13}$	(2), (8), (9), (10)
1345	214.961271	52.842360	8.6351	-2.96 ± 0.16	-1.73 ± 0.30	1.74	$8.64^{+0.25}_{-0.27}$	$-2.82^{+0.63}_{-0.66}$	$-2.02^{+0.16}_{-0.16}$	(6), (8)
1345	214.811853	52.737113	9.5635	-2.64 ± 0.05	-2.58 ± 0.13	3.86	$10.42^{+0.20}_{-0.65}$	$-1.98^{+0.40}_{-0.42}$	$-2.18^{+0.13}_{-0.08}$	(6)
1345	214.732527	52.758097	9.8505	-3.07 ± 0.07	-2.90 ± 0.17	2.95	$9.61^{+0.79}_{-0.04}$	$-2.18^{+0.28}_{-0.30}$	$-2.30^{+0.10}_{-0.13}$	(6)
2750	214.878972	52.896751	6.5357	-2.57 ± 0.03	-2.59 ± 0.07	10.34	$6.58^{+0.03}_{-0.13}$	$-2.38^{+0.33}_{-0.33}$	$-2.48^{+0.07}_{-0.04}$	⋯
2750	214.877890	52.897677	6.5361	-2.63 ± 0.05	-2.56 ± 0.12	5.22	$6.54^{+0.03}_{-0.32}$	$-2.08^{+0.29}_{-0.31}$	$-2.47^{+0.09}_{-0.05}$	⋯
2750	214.941618	52.929132	6.9806	-1.99 ± 0.03	-2.06 ± 0.08	6.43	$7.04^{+0.38}_{-0.01}$	$-2.05^{+0.34}_{-0.37}$	$-2.21^{+0.08}_{-0.06}$	⋯
2750	214.940489	52.932559	7.5524	-2.48 ± 0.04	-2.44 ± 0.13	4.41	$7.47^{+0.53}_{-0.45}$	$-2.62^{+0.73}_{-0.75}$	$-2.46^{+0.07}_{-0.05}$	⋯
2750	214.906639	52.945504	11.0419	-1.82 ± 0.05	-1.85 ± 0.13	5.48	$11.54^{+0.23}_{-0.34}$	$-1.88^{+0.44}_{-0.41}$	$-2.17^{+0.11}_{-0.11}$	⋯
2750	214.922777	52.911524	11.1168	-1.65 ± 0.06	-2.08 ± 0.21	3.62	$11.22^{+0.37}_{-0.85}$	$-2.61^{+0.45}_{-0.50}$	$-2.40^{+0.12}_{-0.09}$	(1), (6)
2750	214.943146	52.942446	11.4111	-1.88 ± 0.04	-2.10 ± 0.11	5.14	$11.90^{+0.17}_{-0.32}$	$-3.13^{+0.43}_{-0.42}$	$-2.53^{+0.06}_{-0.03}$	(6), (7)

Note. We provide spectroscopic β measurements in the C94 filters and the 1250–3000 Å rest-frame wavelength range as well as photometric β from β bias-corrected power-law fits to the photometry and `Bagpipes` SED fitting. SNR_{UV} indicates the SNR obtained from the PRISM spectrum averaged over $1250 < \lambda_{rest}/\text{Å} < 3000$. We reference works that have previously reported these galaxies following the numbering system: (1) C. T. Donnan et al. (2023), (2) K. E. Heintz et al. (2023a), (3) E. Curtis-Lake et al. (2023), (4) A. J. Bunker et al. (2024), (5) K. N. Hainline et al. (2024), (6) P. Arrabal Haro et al. (2023a), (7) K. E. Heintz et al. (2024), (8) K. Nakajima et al. (2023), (9) R. L. Sanders et al. (2024), (10) M. Tang et al. (2023).

ORCID iDs

Duncan Austin https://orcid.org/0000-0003-0519-9445
Christopher J. Conselice https://orcid.org/0000-0003-1949-7638
Nathan J. Adams https://orcid.org/0000-0003-4875-6272
Thomas Harvey https://orcid.org/0000-0002-4130-636X
Qiao Duan https://orcid.org/0009-0009-8105-4564
James Trussler https://orcid.org/0000-0002-9081-2111
Qiong Li https://orcid.org/0000-0002-3119-9003
Ignas Juodžbalis https://orcid.org/0009-0003-7423-8660
Katherine Ormerod https://orcid.org/0000-0003-2000-3420
Leonardo Ferreira https://orcid.org/0000-0002-8919-079X
Lewi Westcott https://orcid.org/0009-0008-8642-5275
Honor Harris https://orcid.org/0009-0005-0817-6419
Stephen M. Wilkins https://orcid.org/0000-0003-3903-6935
Rachana Bhatawdekar https://orcid.org/0000-0003-0883-2226
Joseph Caruana https://orcid.org/0000-0002-6089-0768

Dan Coe https://orcid.org/0000-0001-7410-7669
Seth H. Cohen https://orcid.org/0000-0003-3329-1337
Simon P. Driver https://orcid.org/0000-0001-9491-7327
Jordan C. J. D'Silva https://orcid.org/0000-0002-9816-1931
Brenda Frye https://orcid.org/0000-0003-1625-8009
Lukas J. Furtak https://orcid.org/0000-0001-6278-032X
Norman A. Grogin https://orcid.org/0000-0001-9440-8872
Nimish P. Hathi https://orcid.org/0000-0001-6145-5090
Benne W. Holwerda https://orcid.org/0000-0002-4884-6756
Rolf A. Jansen https://orcid.org/0000-0003-1268-5230
Anton M. Koekemoer https://orcid.org/0000-0002-6610-2048
Madeline A. Marshall https://orcid.org/0000-0001-6434-7845
Mario Nonino https://orcid.org/0000-0001-6342-9662
Rafael Ortiz, III https://orcid.org/0000-0002-6150-833X
Nor Pirzkal https://orcid.org/0000-0003-3382-5941
Aaron Robotham https://orcid.org/0000-0003-0429-3579
Russell E. Ryan, Jr. https://orcid.org/0000-0003-0894-1588
Jake Summers https://orcid.org/0000-0002-7265-7920
Christopher N. A. Willmer https://orcid.org/0000-0001-9262-9997
Rogier A. Windhorst https://orcid.org/0000-0001-8156-6281
Haojing Yan https://orcid.org/0000-0001-7592-7714
Erik Zackrisson https://orcid.org/0000-0003-1096-2636

References

Adams, N. J., Conselice, C. J., Austin, D., et al. 2024, ApJ, 965, 169
Adams, N. J., Conselice, C. J., Ferreira, L., et al. 2023, MNRAS, 518, 4755
Arrabal Haro, P., Dickinson, M., Finkelstein, S. L., et al. 2023a, ApJL, 951, L22
Arrabal Haro, P., Dickinson, M., Finkelstein, S. L., et al. 2023b, Natur, 622, 707
Astropy Collaboration, Price-Whelan, A. M., Lim, P. L., et al. 2022, ApJ, 935, 167
Astropy Collaboration, Price-Whelan, A. M., Sipőcz, B. M., et al. 2018, AJ, 156, 123
Astropy Collaboration, Robitaille, T. P., Tollerud, E. J., et al. 2013, A&A, 558, A33
Atek, H., Shuntov, M., Furtak, L. J., et al. 2023, MNRAS, 519, 1201
Austin, D., Adams, N., Conselice, C. J., et al. 2023, ApJL, 952, L7
Bagley, M. B., Finkelstein, S. L., Koekemoer, A. M., et al. 2023, ApJL, 946, L12
Bagley, M. B., Pirzkal, N., Finkelstein, S. L., et al. 2024, ApJL, 965, L6
Barbary, K. 2016, JOSS, 1, 58
Bertin, E., & Arnouts, S. 1996, A&AS, 117, 393
Bezanson, R., Labbe, I., Whitaker, K. E., et al. 2024, ApJ, 974, 92
Bhatawdekar, R., & Conselice, C. J. 2021, ApJ, 909, 144
Bianchi, S., Schneider, R., & Valiante, R. 2009, in ASP Conf. Ser. 414, Cosmic Dust— Near and Far, ed. T. Henning, E. Grün, & J. Steinacker (San Francisco, CA: ASP), 65
Blaizot, J., Garel, T., Verhamme, A., et al. 2023, MNRAS, 523, 3749
Bocchio, M., Marassi, S., Schneider, R., et al. 2016, A&A, 587, A157
Bohlin, R. C. 2016, AJ, 152, 60
Böker, T., Beck, T. L., Birkmann, S. M., et al. 2023, PASP, 135, 038001
Bouwens, R., González-López, J., Aravena, M., et al. 2020, ApJ, 902, 112
Bouwens, R., Illingworth, G., Oesch, P., et al. 2023, MNRAS, 523, 1009
Bouwens, R. J., Illingworth, G. D., Franx, M., et al. 2009, ApJ, 705, 936
Bouwens, R. J., Illingworth, G. D., Oesch, P. A., et al. 2010, ApJL, 708, L69
Bouwens, R. J., Illingworth, G. D., Oesch, P. A., et al. 2011, ApJ, 737, 90
Bouwens, R. J., Illingworth, G. D., Oesch, P. A., et al. 2012, ApJ, 754, 83
Bouwens, R. J., Illingworth, G. D., Oesch, P. A., et al. 2014, ApJ, 793, 115
Bouwens, R. J., Illingworth, G. D., Oesch, P. A., et al. 2015a, ApJ, 811, 140
Bouwens, R. J., Illingworth, G. D., Oesch, P. A., et al. 2015b, ApJ, 803, 34
Bouwens, R. J., Oesch, P. A., Labbé, I., et al. 2016, ApJ, 830, 67
Bouwens, R. J., Smit, R., Schouws, S., et al. 2022, ApJ, 931, 160
Bowler, R. A. A., Inami, H., Sommovigo, L., et al. 2024, MNRAS, 527, 5808
Bradley, L., Sipőcz, B., Robitaille, T., et al., 2022 astropy/photutils: v1.5.0, Zenodo, doi:10.5281/zenodo.6825092
Brammer, G. B., van Dokkum, P. G., & Coppi, P. 2008, ApJ, 686, 1503
Bruzual, G., & Charlot, S. 2003, MNRAS, 344, 1000
Bunker, A. J., Cameron, A. J., Curtis-Lake, E., et al. 2024, A&A, 690, A288
Bushouse, H., Eisenhamer, J., Dencheva, N., et al., 2022 JWST Calibration Pipeline, v1.8.2, Zenodo, doi:10.5281/zenodo.7325378
Byler, N., Dalcanton, J. J., Conroy, C., & Johnson, B. D. 2017, ApJ, 840, 44
Byrne, C. M., Stanway, E. R., Eldridge, J. J., McSwiney, L., & Townsend, O. T. 2022, MNRAS, 512, 5329
Calvi, V., Trenti, M., Stiavelli, M., et al. 2016, ApJ, 817, 120
Calzetti, D., Armus, L., Bohlin, R. C., et al. 2000, ApJ, 533, 682
Calzetti, D., Kinney, A. L., & Storchi-Bergmann, T. 1994, ApJ, 429, 582
Cameron, A. J., Katz, H., Rey, M. P., & Saxena, A. 2023, MNRAS, 523, 3516
Cameron, A. J., Katz, H., Witten, C., et al. 2024, MNRAS, 534, 523
Carnall, A. C., McLure, R. J., Dunlop, J. S., & Davé, R. 2018, MNRAS, 480, 4379
Castellano, M., Fontana, A., Treu, T., et al. 2022, ApJL, 938, L15
Castellano, M., Fontana, A., Treu, T., et al. 2023, ApJL, 948, L14
Castellano, M., Napolitano, L., Fontana, A., et al. 2024, ApJ, 972, 143
Chabrier, G. 2003, PASP, 115, 763
Charbonnel, C., Schaerer, D., Prantzos, N., et al. 2023, A&A, 673, L7
Charlot, S., & Fall, S. M. 2000, ApJ, 539, 718
Chen, Z., Stark, D. P., Mason, C., et al. 2024, MNRAS, 528, 7052
Chevallard, J., & Charlot, S. 2016, MNRAS, 462, 1415
Chisholm, J., Prochaska, J. X., Schaerer, D., Gazagnes, S., & Henry, A. 2020, MNRAS, 498, 2554
Chisholm, J., Saldana-Lopez, A., Flury, S., et al. 2022, MNRAS, 517, 5104
Choustikov, N., Katz, H., Saxena, A., et al. 2024, MNRAS, 529, 3751
Conroy, C., & Gunn, J. E., 2010 FSPS: Flexible Stellar Population Synthesis, Astrophysics Source Code Library, ascl:1010.043
Conroy, C., Gunn, J. E., & White, M. 2009, ApJ, 699, 486
Conselice, C. J., Adams, N., Harvey, T., et al. 2025, ApJ, 983, 30
Cullen, F., McLeod, D. J., McLure, R. J., et al. 2024, MNRAS, 531, 997
Cullen, F., McLure, R. J., McLeod, D. J., et al. 2023, MNRAS, 520, 14
Curtis-Lake, E., Carniani, S., Cameron, A., et al. 2023, NatAs, 7, 622
Davé, R., Anglés-Alcázar, D., Narayanan, D., et al. 2019, MNRAS, 486, 2827
De Barros, S., Oesch, P. A., Labbé, I., et al. 2019, MNRAS, 489, 2355
D'Eugenio, F., Maiolino, R., Carniani, S., et al. 2024, A&A, 689, A152
Donnan, C. T., McLeod, D. J., Dunlop, J. S., et al. 2023, MNRAS, 518, 6011
Donnan, C. T., McLure, R. J., Dunlop, J. S., et al. 2024, MNRAS, 533, 3222
Draine, B. T. 2009, in ASP Conf. Ser. 414, Cosmic Dust—Near and Far, ed. T. Henning, E. Grün, & J. Steinacker (San Francisco, CA: ASP), 453
Draine, B. T. 2011, Physics of the Interstellar and Intergalactic Medium (Princeton, NJ: Princeton Univ. Press)
Draine, B. T., & Salpeter, E. E. 1979, ApJ, 231, 77
Drakos, N. E., Villasenor, B., Robertson, B. E., et al. 2022, ApJ, 926, 194
Driver, S. P., Hill, D. T., Kelvin, L. S., et al. 2011, MNRAS, 413, 971
Dunlop, J. S., McLure, R. J., Robertson, B. E., et al. 2012, MNRAS, 420, 901
Dunlop, J. S., Rogers, A. B., McLure, R. J., et al. 2013, MNRAS, 432, 3520
Eisenstein, D. J., Willott, C., Alberts, S., et al. 2023, arXiv:2306.02465
Eldridge, J. J., Stanway, E. R., Xiao, L., et al. 2017, PASA, 34, e058
Ellis, R. S., McLure, R. J., Dunlop, J. S., et al. 2013, ApJL, 763, L7
Endsley, R., Stark, D. P., Whitler, L., et al. 2023, MNRAS, 524, 2312
Faber, S. 2011, The Cosmic Assembly Near-IR Deep Extragalactic Legacy Survey ("CANDELS"), STScI/MAST, doi:10.17909/T94S3X
Feltre, A., Charlot, S., & Gutkin, J. 2016, MNRAS, 456, 3354
Ferland, G. J., Chatzikos, M., Guzmán, F., et al. 2017, RMxAA, 53, 385
Ferrara, A. 2024, A&A, 684, A207
Ferrara, A., Pallottini, A., & Dayal, P. 2023, MNRAS, 522, 3986
Ferreira, L., Adams, N., Conselice, C. J., et al. 2022, ApJL, 938, L2
Ferruit, P., Jakobsen, P., Giardino, G., et al. 2022, A&A, 661, A81
Finkelstein, S. L., Bagley, M. B., Arrabal Haro, P., et al. 2022, ApJL, 940, L55
Finkelstein, S. L., Bagley, M. B., Ferguson, H. C., et al. 2023, ApJL, 946, L13
Finkelstein, S. L., Leung, G. C. K., Bagley, M. B., et al. 2024, ApJL, 969, L2
Finkelstein, S. L., Papovich, C., Giavalisco, M., et al. 2010, ApJ, 719, 1250
Finkelstein, S. L., Papovich, C., Salmon, B., et al. 2012, ApJ, 756, 164
Fujimoto, S., Arrabal Haro, P., Dickinson, M., et al. 2023, ApJL, 949, L25
Furtak, L. J., Shuntov, M., Atek, H., et al. 2023, MNRAS, 519, 3064
Gaia Collaboration, Brown, A. G. A., Vallenari, A., et al. 2018, A&A, 616, A1
Gail, H. P., Zhukovska, S. V., Hoppe, P., & Trieloff, M. 2009, ApJ, 698, 1136
Gardner, J. P., Mather, J. C., Abbott, R., et al. 2023, PASP, 135, 068001
Gonzalez-Perez, V., Lacey, C. G., Baugh, C. M., Frenk, C. S., & Wilkins, S. M. 2013, MNRAS, 429, 1609

Gordon, K. D., Clayton, G. C., Misselt, K. A., Landolt, A. U., & Wolff, M. J. 2003, ApJ, 594, 279
Grogin, N. A., Kocevski, D. D., Faber, S. M., et al. 2011, ApJS, 197, 35
Groth, E. J., Kristian, J. A., Lynds, R., et al. 1994, AAS Meeting, 185, 53.09
Gunn, J. E., & Peterson, B. A. 1965, ApJ, 142, 1633
Gutkin, J., Charlot, S., & Bruzual, G. 2016, MNRAS, 462, 1757
Haiman, Z. 2002, ApJL, 576, L1
Hainline, K., Robertson, B., Tacchella, S., et al. 2023, AAS Meeting, 55, 212.02
Hainline, K. N., Johnson, B. D., Robertson, B., et al. 2024, ApJ, 964, 71
Harikane, Y., Ouchi, M., Oguri, M., et al. 2023, ApJS, 265, 5
Harvey, T., Conselice, C. J., Adams, N. J., et al. 2025, ApJ, 978, 89
Hathi, N. P., Cohen, S. H., Ryan, R. E. J., et al. 2013, ApJ, 765, 88
Hathi, N. P., Malhotra, S., Rhoads, J. E., et al. 2008, ApJ, 673, 686
Heintz, K. E., Brammer, G. B., Giménez-Arteaga, C., et al. 2023a, NatAs, 7, 1517
Heintz, K. E., Brammer, G. B., Watson, D., et al. 2025, A&A, 693, A60
Heintz, K. E., Watson, D., Brammer, G., et al. 2024, Sci, 384, 890
Hensley, B. S., & Draine, B. T. 2023, ApJ, 948, 55
Hodges, J. L. 1958, ArM, 3, 469
Hoffmann, S. L., Mack, J., Avila, R., et al. 2021, AAS Meeting, 53, 216.02
Höfner, S., & Olofsson, H. 2018, A&ARv, 26, 1
Hsiao, T. Y.-Y., Abdurro'uf, Coe, D., et al. 2024, ApJ, 973, 8
Hunter, J. D. 2007, CSE, 9, 90
Inayoshi, K., Harikane, Y., Inoue, A. K., Li, W., & Ho, L. C. 2022, ApJL, 938, L10
Inoue, A. K., Shimizu, I., Iwata, I., & Tanaka, M. 2014, MNRAS, 442, 1805
Jaacks, J., Finkelstein, S. L., & Bromm, V. 2018, MNRAS, 475, 3883
Jakobsen, P., Ferruit, P., Alves de Oliveira, C., et al. 2022, A&A, 661, A80
Jansen, R. A., & Windhorst, R. A. 2018, PASP, 130, 124001
Jaskot, A. E., & Ravindranath, S. 2016, ApJ, 833, 136
Johnson, B. D., Leja, J., Conroy, C., & Speagle, J. S. 2021, ApJS, 254, 22
Kannan, R., Smith, A., Garaldi, E., et al. 2022, MNRAS, 514, 3857
Katz, H., Garel, T., Rosdahl, J., et al. 2022, MNRAS, 515, 4265
Keating, L. C., Bolton, J. S., Cullen, F., et al. 2024, MNRAS, 532, 1646
Kirchschlager, F., Mattsson, L., & Gent, F. A. 2022, MNRAS, 509, 3218
Kirchschlager, F., Mattsson, L., & Gent, F. A. 2024, NatCo, 15, 1841
Kirchschlager, F., Schmidt, F. D., Barlow, M. J., et al. 2019, MNRAS, 489, 4465
Kocevski, D. D., Finkelstein, S. L., Barro, G., et al. 2024, ApJ, 986, 126
Koekemoer, A. M., Ellis, R. S., McLure, R. J., et al. 2013, ApJS, 209, 3
Koekemoer, A. M., Faber, S. M., Ferguson, H. C., et al. 2011, ApJS, 197, 36
Kokorev, V., Caputi, K. I., Greene, J. E., et al. 2024, ApJ, 968, 38
Kron, R. G. 1980, ApJS, 43, 305
Kroupa, P. 2001, MNRAS, 322, 231
Labbe, I., Greene, J. E., Bezanson, R., et al. 2025, ApJ, 978, 92
Lanzetta, K. 2000, in Encyclopedia of Astronomy and Astrophysics, ed. P. Murdin (Bristol: IOP Publishing), 2141
Larson, R. L., Hutchison, T. A., Bagley, M., et al. 2023, ApJ, 958, 141
Lau, R. M., Eldridge, J. J., Hankins, M. J., et al. 2020, ApJ, 898, 74
Lau, R. M., Hankins, M. J., Han, Y., et al. 2022, NatAs, 6, 1308
Leitherer, C., Schaerer, D., Goldader, J. D., et al. 1999, ApJS, 123, 3
Leja, J., Carnall, A. C., Johnson, B. D., Conroy, C., & Speagle, J. S. 2019, ApJ, 876, 3
Leung, G. C. K., Bagley, M. B., Finkelstein, S. L., et al. 2023, ApJL, 954, L46
Levesque, E. M., Massey, P., Olsen, K. A. G., et al. 2006, ApJ, 645, 1102
Liske, J., Baldry, I. K., Driver, S. P., et al. 2015, MNRAS, 452, 2087
Looser, T. J., D'Eugenio, F., Maiolino, R., et al. 2024, Natur, 629, 53
Lotz, J. M., Koekemoer, A., Coe, D., et al. 2017, ApJ, 837, 97
Lovell, C. C., Vijayan, A. P., Thomas, P. A., et al. 2021, MNRAS, 500, 2127
Lu, T.-Y., Mason, C. A., Hutter, A., et al. 2024, MNRAS, 528, 4872
Madau, P., & Dickinson, M. 2014, ARA&A, 52, 415
Mainali, R., Kollmeier, J. A., Stark, D. P., et al. 2017, ApJL, 836, L14
Malhotra, S., & Rhoads, J. E. 2006, ApJL, 647, L95
Marassi, S., Schneider, R., Limongi, M., et al. 2019, MNRAS, 484, 2587
Marley, M., Saumon, D., Morley, C., et al. 2021, Sonora Bobcat: Cloud-free, Substellar Atmosphere Models, Spectra, Photometry, Evolution, and Chemistry, Zenodo, doi:10.5281/zenodo.5063476
Mascia, S., Pentericci, L., Calabrò, A., et al. 2023, A&A, 672, A155
Mason, C. A., Trenti, M., & Treu, T. 2023, MNRAS, 521, 497
Matthee, J., Naidu, R. P., Brammer, G., et al. 2024, ApJ, 963, 129
Mauerhofer, V., & Dayal, P. 2023, MNRAS, 526, 2196
McLeod, D. J., Donnan, C. T., McLure, R. J., et al. 2023, MNRAS, 527, 5004
McLure, R. J., Dunlop, J. S., Cullen, F., et al. 2018, MNRAS, 476, 3991
McLure, R. J., Dunlop, J. S., de Ravel, L., et al. 2011, MNRAS, 418, 2074
McQuinn, M. 2016, ARA&A, 54, 313
Menanteau, F., Hughes, J. P., Sifón, C., et al. 2012, ApJ, 748, 7
Meurer, G. R., Heckman, T. M., & Calzetti, D. 1999, ApJ, 521, 64
Micelotta, E. R., Matsuura, M., & Sarangi, A. 2018, SSRv, 214, 53
Miralda-Escudé, J. 1998, ApJ, 501, 15
Mirocha, J., & Furlanetto, S. R. 2023, MNRAS, 519, 843
Momcheva, I. G., Brammer, G. B., van Dokkum, P. G., et al. 2016, ApJS, 225, 27
Morales, A. M., Finkelstein, S. L., Leung, G. C. K., et al. 2024, ApJL, 964, L24
Muzzin, A., Suess, K. A., Marchesini, D., et al. 2025, arXiv:2507.19706
Naidu, R. P., Oesch, P. A., van Dokkum, P., et al. 2022, ApJL, 940, L14
Nakajima, K., Ouchi, M., Isobe, Y., et al. 2023, ApJS, 269, 33
Nakane, M., Ouchi, M., Nakajima, K., et al. 2024, ApJ, 967, 28
Nanayakkara, T., Brinchmann, J., Boogaard, L., et al. 2019, A&A, 624, A89
Nanayakkara, T., Glazebrook, K., Jacobs, C., et al. 2023, ApJL, 947, L26
Napolitano, L., Pentericci, L., Santini, P., et al. 2024, A&A, 688, A106
O'Brien, R., Jansen, R. A., Grogin, N. A., et al. 2024, ApJS, 272, 19
Oesch, P. A., Bouwens, R. J., Illingworth, G. D., Labbé, I., & Stefanon, M. 2018, ApJ, 855, 105
Oesch, P. A., Bouwens, R. J., Illingworth, G. D., et al. 2013, ApJ, 773, 75
Oesch, P. A., Brammer, G., van Dokkum, P. G., et al. 2016, ApJ, 819, 129
Oke, J. B. 1974, ApJS, 27, 21
Oke, J. B., & Gunn, J. E. 1983, ApJ, 266, 713
Pei, Y. C. 1992, ApJ, 395, 130
Pérez-González, P. G., Costantin, L., Langeroodi, D., et al. 2023, ApJL, 951, L1
Perrin, M. D., Sivaramakrishnan, A., Lajoie, C.-P., et al. 2014, Proc. SPIE, 9143, 91433X
Perrin, M. D., Soummer, R., Elliott, E. M., Lallo, M. D., & Sivaramakrishnan, A. 2012, Proc. SPIE, 8442, 84423D
Planck Collaboration, Ade, P. A. R., Aghanim, N., et al. 2016, A&A, 594, A13
Planck Collaboration, Aghanim, N., Akrami, Y., et al. 2020, A&A, 641, A6
Raiter, A., Schaerer, D., & Fosbury, R. A. E. 2010, A&A, 523, A64
Rasmussen Cueto, E., Hutter, A., Dayal, P., et al. 2023, A&A, 686, A138
Rawle, T. D., Giardino, G., Franz, D. E., et al. 2022, Proc. SPIE, 12180, 121803R
Rieke, M. J., Kelly, D., & Horner, S. 2005, Proc. SPIE, 5904, 1
Rieke, M. J., Kelly, D. M., Misselt, K., et al. 2023, PASP, 135, 028001
Rigby, J. R., Bayliss, M. B., Gladders, M. D., et al. 2015, ApJL, 814, L6
Roberts-Borsani, G., Treu, T., Shapley, A., et al. 2024, ApJ, 976, 193
Rodrigo, C., & Solano, E. 2020, Contributions to the XIV.0 Scientific Meeting (virtual) of the Spanish Astronomical Society (Madrid: La Sociedad Española de Astronomía), 182, https://www.sea-astronomia.es/reunion-cientifica-2020
Rogers, A. B., McLure, R. J., & Dunlop, J. S. 2013, MNRAS, 429, 2456
Rogers, A. B., McLure, R. J., Dunlop, J. S., et al. 2014, MNRAS, 440, 3714
Salim, S., & Narayanan, D. 2020, ARA&A, 58, 529
Salpeter, E. E. 1955, ApJ, 121, 161
Sanders, R. L., Shapley, A. E., Topping, M. W., Reddy, N. A., & Brammer, G. B. 2024, ApJ, 962, 24
Sarangi, A., Dwek, E., & Kazanas, D. 2019, ApJ, 885, 126
Sarmento, R., Scannapieco, E., & Cohen, S. 2018, ApJ, 854, 75
Sarmento, R., Scannapieco, E., & Côté, B. 2019, ApJ, 871, 206
Saxena, A., Bunker, A. J., Jones, G. C., et al. 2024, A&A, 684, A84
Saxena, A., Pentericci, L., Schaerer, D., et al. 2020, MNRAS, 496, 3796
Saxena, A., Robertson, B. E., Bunker, A. J., et al. 2023, A&A, 678, A68
Schaerer, D. 2002, A&A, 382, 28
Schaerer, D. 2003, A&A, 397, 527
Schmidt, K. B., Huang, K. H., Treu, T., et al. 2017, ApJ, 839, 17
Schneider, R., & Maiolino, R. 2024, A&AR, 32, 2
Senchyna, P., Plat, A., Stark, D. P., & Rudie, G. C. 2024, ApJ, 966, 92
Skelton, R. E., Whitaker, K. E., Momcheva, I. G., et al. 2014, ApJS, 214, 24
Stanway, E. R., & Eldridge, J. J. 2018, MNRAS, 479, 75
Stark, D. P., Ellis, R. S., Charlot, S., et al. 2017, MNRAS, 464, 469
Stecher, T. P., & Donn, B. 1965, ApJ, 142, 1681
Stefanon, M., Labbé, I., Bouwens, R. J., et al. 2017, ApJ, 851, 43
Steinhardt, C. L., Kokorev, V., Rusakov, V., Garcia, E., & Sneppen, A. 2023, ApJL, 951, L40
Suess, K. A., Weaver, J. R., Price, S. H., et al. 2024, ApJ, 976, 101
Tacchella, S., Finkelstein, S. L., Bagley, M., et al. 2022, ApJ, 927, 170
Tang, M., Stark, D. P., Chen, Z., et al. 2023, MNRAS, 526, 1657
Tang, M., Stark, D. P., Topping, M. W., et al. 2024, ApJ, 975, 208
Tepper-García, T. 2006, MNRAS, 369, 2025
Todini, P., & Ferrara, A. 2001, MNRAS, 325, 726
Tomczak, A. R., Quadri, R. F., Tran, K.-V. H., et al. 2014, ApJ, 783, 85
Topping, M. W., Stark, D. P., Endsley, R., et al. 2022, ApJ, 941, 153

Topping, M. W., Stark, D. P., Endsley, R., et al. 2024a, MNRAS, 529, 4087
Topping, M. W., Stark, D. P., Senchyna, P., et al. 2024b, MNRAS, 529, 3301
Totani, T., Kawai, N., Kosugi, G., et al. 2006, PASJ, 58, 485
Treu, T., Roberts-Borsani, G., Bradac, M., et al. 2022, ApJ, 935, 110
Umeda, H., Ouchi, M., Nakajima, K., et al. 2024, ApJ, 971, 124
Valiante, R., Schneider, R., Salvadori, S., & Gallerani, S. 2014, MNRAS, 444, 2442
Vázquez, G. A., & Leitherer, C. 2005, ApJ, 621, 695
Vijayan, A. P., Clay, S. J., Thomas, P. A., et al. 2019, MNRAS, 489, 4072
Vijayan, A. P., Lovell, C. C., Wilkins, S. M., et al. 2021, MNRAS, 501, 3289
Virtanen, P., Gommers, R., Oliphant, T. E., et al. 2020, NatMe, 17, 261
Wang, B., Fujimoto, S., Labbé, I., et al. 2023, ApJL, 957, L34
Whitaker, K. E., Ashas, M., Illingworth, G., et al. 2019, ApJS, 244, 16
Whitler, L., Stark, D. P., Endsley, R., et al. 2024, MNRAS, 529, 855
Wilkins, S. M., Gonzalez-Perez, V., Lacey, C. G., & Baugh, C. M. 2012, MNRAS, 424, 1522
Wilkins, S. M., Bouwens, R. J., Oesch, P. A., et al. 2016, MNRAS, 455, 659
Wilkins, S. M., Bunker, A., Coulton, W., et al. 2013, MNRAS, 430, 2885
Wilkins, S. M., Turner, J. C., Bagley, M. B., et al. 2023a, arXiv:2311.08065
Wilkins, S. M., Vijayan, A. P., Lovell, C. C., et al. 2023b, MNRAS, 519, 3118
Williams, C. C., Curtis-Lake, E., Hainline, K. N., et al. 2018, ApJS, 236, 33
Windhorst, R. A., Cohen, S. H., Jansen, R. A., et al. 2023, AJ, 165, 13
Witstok, J., Shivaei, I., Smit, R., et al. 2023, Nature, 621, 267
Witstok, J., Smit, R., Saxena, A., et al. 2024, A&A, 682, A40
Wu, X., Davé, R., Tacchella, S., & Lotz, J. 2020, MNRAS, 494, 5636
Xiao, L., Stanway, E. R., & Eldridge, J. J. 2018, MNRAS, 477, 904
Yan, H., Ma, Z., Ling, C., et al. 2023, ApJL, 942, L9
Yung, L. Y. A., Somerville, R. S., Finkelstein, S. L., Wilkins, S. M., & Gardner, J. P. 2024a, MNRAS, 527, 5929
Yung, L. Y. A., Somerville, R. S., Nguyen, T., et al. 2024b, MNRAS, 530, 4868
Zackrisson, E., Inoue, A. K., & Jensen, H. 2013, ApJ, 777, 39
Zackrisson, E., Rydberg, C.-E., Schaerer, D., Östlin, G., & Tuli, M. 2011, ApJ, 740, 13
Zavala, J. A., Castellano, M., Akins, H. B., et al. 2025, NatAs, 9, 155
Zhukovska, S., Gail, H. P., & Trieloff, M. 2008, A&A, 479, 453
Ziparo, F., Ferrara, A., Sommovigo, L., & Kohandel, M. 2023, MNRAS, 520, 2445